On Spherical Nanoindentation Stress-Strain Curves, Creep and Kinking Nonlinear Elasticity in Brittle Hexagonal Single Crystals

A Thesis

Submitted to the Faculty

of

Drexel University

by

Sandip Basu

in partial fulfillment of the

requirements for the degree

of

Doctor of Philosophy

August 2008

Dedication

This thesis is dedicated to my father (Nilmani Basu), mother (Swapna Basu), and brother (Santanu Basu), who believed in me and inspired me in every step of my life.

Acknowledgements

I would like to take this opportunity to thank all the people who supported me in different ways during my stay here at Drexel University.

First, I want to thank all my dissertation committee members – Prof. Michel Barsoum, Prof. Surya Kalidindi, Prof. Yury Gogotsi, Prof. Jonathan Spanier and Prof. Miladin Radovic – for their time and critical evaluation of my research. I am grateful for all the stimulating discussions and their constructive suggestions regarding my research.

At this moment, I do not have enough words to thank Prof. Barsoum, who has been much more than an advisor to me and I will always remember everything I learnt from him. Without his motivation and enthusiasm this research would not have been possible. He always made me think positive – not only regarding the research, but also in other aspects of life. I am indebted to him for what I achieved during the last five years. For now, I would say THANK YOU. I am really honored to work with him.

I am grateful to all the members of our research group. Specially, I would like to thank Dr. Adrish Ganguly and Dr. Surojit Gupta for their help and support since the very beginning; Dr. Anand Murugaiah for all the help with nanoindentation; Dr. Tiejun Zhen and Dr. Elizabeth Hoffman for their support and help with various lab activities; and, of course, Dr. Aiguo Zhou for numerous stimulating discussions and for being a great friend – without his effort we would not have reached this far in this research. I would also like to thank Dr. Peter Finkel, Dr. Zhengming Sun, Dr. Dmitri Filimonov, Dr. Ori Yeheskel, Shahram Amini, Alex Moseson, Ted Scabarozi, Mathieu Fraczkiewicz, Charles Spencer, Ismail Albayrak, Ryan Buchs and Joan Berger for their invaluable help and support in

this endeavor and also making our group a fun place to work in. I also want to say thanks to Chloe Baldasseroni and for her friendship and support during these years.

I am grateful to all my friends in the Department of Materials Science and Engineering and at Drexel University. I really enjoyed having all of them around. I would like to express my thanks specially to Dr. Ranjan Dash, Varun Gupta, Servesh Tiwari, Dr. Kishore Tenneti, Dr. Hari Duvvuru, Dr. Lalit Bansal, Dr. Abhijit Joshi, Dr. Maria Pia Rossi, Dr. Gwenaelle Proust, Dr. Davide Mattia, Adarsh Sagar, Sebastian Osswald, Dr. Cristelle Portet and Steven Nonnenman for all their help and for making my stay an enjoyable experience. Besides being great friends, I would also like to thank Dr. Tom Juliano and Sidhhartha Pathak for their help and support with my experiments.

I am indebted to all the faculty members in the department, for being very open and generous and, of course, for what I learnt from their courses. Specially I would like to thank Prof. Roger Doherty and Prof. Antonios Zavaliangos for numerous stimulating discussions and invaluable suggestions.

I would also like to thank all the staff in the department, specially Judith Trachtman, Dorilona Rose and Keiko Nakazawa for extending their helping hand whenever needed.

Lastly, I would like thank my parents and my brother from the bottom of my heart. I could not have come this far without their unconditional love, support and inspiration.

TABLE OF CONTENTS

LIST OF TABLES

LIST OF FIGURES

ABSTRACT

On Spherical Nanoindentation Stress-Strain Curves, Creep and Kinking Nonlinear Elasticity in Brittle Hexagonal Single Crystals
Sandip Basu
Advisor: Prof. Michel W. Barsoum
Co-advisor: Prof. Surya R. Kalidindi

Despite the fact that they can accurately delineate the onset of the elasto-plastic transition of solids, spherical nanoindentation, NI, experiments are less common than sharp indenters. Herein a novel, robust technique to convert NI load-displacement to stress-strain curves was developed and applied to fused silica, aluminum, iron and the hexagonal single crystals: ZnO, $LiNbO_3$, GaN, sapphire and mica. In all cases, the NI stress-strain curves clearly showed the onset of yield and subsequent strain hardening. We also show, by Weibull analysis, that the pop-in stresses are stochastic in nature and depend on the presence of dislocation-nucleating defects.

The ability to calculate the NI or mean stress in real time allowed us to run, for the first time, constant NI stress experiments, which, in turn, was exploited to quantify the room temperature creep of A-oriented ZnO single crystals. Analyses of the results clearly showed that the creep is a power law creep, with an exponent of ≈ 3 and a threshold stress that was a function of time.

Repeated cyclic NI experiments, in the same location, were used to successfully demonstrate the fully-reversible hysteretic nature of kinking nonlinear elastic, KNE, solids, indirectly confirming the presence of incipient kink bands, IKBs, in these materials. Our recently developed micro-scale model, based on the reversible dislocation

motion in the form of IKBs, shows excellent agreement with the nonlinear hysteretic behavior of C-oriented $LiNbO_3$ single crystals. Combining the NI stress-strain results, we show that the energy dissipation per unit volume per cycle in KNE solids increases with increasing c/a ratios, as well as increasing domain sizes.

In summary this work shows that spherical NI stress/strain curves are a powerful tool for quantifying and understanding the elastic-plastic transition in materials, especially brittle solids, where bulk uniaxial compression/tension experiments are not possible.

CHAPTER 1: INTRODUCTION

1.1 Nanoindentation

1.1.1 Introduction to Nanoindentation

Since the 1990s a lot of attention has been paid to the development of micro and nano-scale devices both from bulk single crystals and thin films. Along that came the necessity of characterizing the mechanical properties at such a small scale. Since the conventional microhardness indentation requires imaging of the impressions, large errors can be introduced in measuring the length of the diagonals at such small length scale. During the last two decades, it has been well established that depth sensing nanoindentation technique is a powerful tool to determine the modulus and hardness of a material by probing a very shallow depth into the sample.[1-5] Different methodologies have been proposed to analyze the load-displacement data from the nanoindenter, and different tip geometries are being used to determine different mechanical properties of solids.[2,3,6-9]

There are a variety of tip geometries available. The most popular ones for sub-micron depth sensing indentation technique are spherical (sphero-conical) and Berkovich (three-sided pyramid) indenters.[5] Most of the indentation studies, with few exceptions, to date have concentrated on determining only the hardness and moduli values from analysis of

nanoindentation results using either the Oliver and Pharr[2] or the Field and Swain method.[6] Somewhat surprisingly, very little work has been done on the determination of indentation stress-strain curves, which can be much more informative in terms of what occurs at the elastic-plastic transition upon contact loading.[10-13]

Since the majority of the work has been carried out using Berkovich indenters, the emphasis has been more on extracting moduli and hardness values.[2,4,5] Berkovich or cube corner indenters are quite sharp and result in plastic deformation almost instantly, consequently, much of the information about the purely elastic region and, as important, the elastic-to-plastic transition is lost, a fact that has long been appreciated.[14] As discussed in this work, that information can be readily obtained by using spherical indenters.

1.1.2 Spherical Nanoindentation

Although it has been more than a century since Brinell[15] proposed the spherical indentation technique, most of the work with spherical indenters was limited to bulk hardness testing. The potential of obtaining a stress-strain curve, by using spherical indenter, was also appreciated for a long time but the technique did not caught on partly because of the ease with which a stress-strain curve can be obtained from uniaxial tension or compression tests. Unfortunately, uniaxial tension or compression tests are not possible for studying the properties of thin surface layers and small volumes of individual material phases those are important for better stability of micro/nano-devices and, moreover, better understanding of the micromechanisms of deformation behavior in materials – especially brittle ceramic materials. The need can be addressed by combining

indenters of spherical geometry with the depth-sensing nanoindentation technique. Spherical nanoindentation makes use of a sphero-conical indenter tip with a certain tip radius. This technique can be used to investigate hardness (or, mean contact pressure) and elastic modulus as a function of penetration depth, produce representative stress-strain curves, and investigate strain hardening.[3] As shown in this work, spherical nanoindentation can also be used for understanding the nonlinear elastic deformation in solids.[11,12,16-18]

1.1.3 Previous Work on Spherical Nanoindentation Stress-Strain Analysis

Given that the conversion of load-displacement curves to indentation stress-strain curves is almost as old as the technique[14] of using indentations to probe the mechanical properties of solids, it is somewhat surprising that this conversion is not much more common than it is. This comment notwithstanding, there have been a number of papers in which spherical nanoindenters have been used.[3,6,10,19,20] Roughly a decade ago, Field and Swain[6] suggested a method to extract indentation stress-strain curves from load-displacement curves. But for reasons that are not clear, and with some exceptions, their methodology has not caught on and as importantly, Swain et al.[21,22] have not used this technique in their more recent work. Instead, in some recent publications,[21,22] plots of hardness vs. indentation penetration were presented, but none as indentation stress-strain curves. Prior to this work (see Ch. 2), we used the Field and Swain method to convert load-displacement results obtained on Ti_3SiC_2,[23] and single-crystals of mica[11] and graphite,[12] loaded parallel to the c-axis to indentation stress-strain curves.

Herbert et al.[20] described a methodology that is almost identical to the one developed here and applied it to Al and concluded that the method was a qualified success in that more work was needed to better delineate the yield points of Al. Again for reasons that are not clear, and as far as we are aware, neither Pharr and co-workers, nor others, have attempted to develop the technique further. In the next chapter (Ch. 2) we describe, in detail, the methodology that has been developed during the current research to convert the load-displacement data to indentation stress-strain.[24]

1.2 Kinking Deformation in Solids

A kink band is known to be the fundamental building block of kink folds. It has been explained as a tabular shear zone that cuts across layered media such as bedding, foliation, crystal lattices or cleavage planes.[25] The formation of kink bands can be observed in many geological structures, as well as highly deformed crystals.[26,27] Frank and Stroh have proposed the concept of nucleation of two oppositely signed dislocation walls attached at both ends in a material with limited slip systems[27] – which we called an incipient kink band (IKB – Fig. 1.1a). They annihilate when the load is removed. They proposed that at much higher stresses the ends of an IKB get detached and form mobile dislocation walls (MDWs – Fig. 1.1b), hence an irreversible and permanent deformation, and damage in the form of delaminations. It is the coalescence of mobile walls that eventually produces the kink boundaries that result in the permanent kink bands (KBs – Fig. 1.1c) that have been documented extensively in the literature.[26-29] Fig. 1.1 shows a schematic of this process.

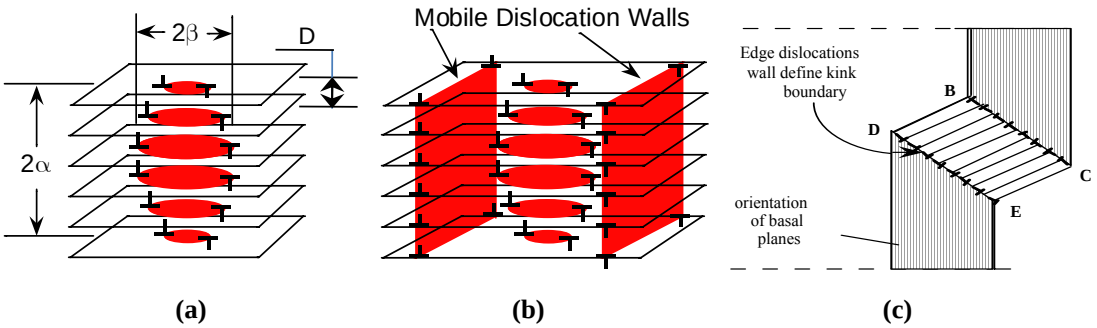

Fig. 1.1 Schematic of the kinking deformation process. a) Incipient kink band (IKB). b) Mobile dislocation walls (MDW). Note a new IKB can form inside two MDWs. c) Permanent kink band (KB).

1.2.1 Kinking Nonlinear Elastic Solids

Kinking nonlinear elastic (KNE) solids are characterized by a marked anisotropy in their plastic properties at the single crystal level. One measure of that anisotropy is a high c/a ratio. It has been postulated that a sufficient condition for a solid to be KNE is a high c/a ratio.[30] This condition renders dislocations other than basal and/or basal twinning prohibitively expensive. The material can thus only deform by basal slip, which leads to kinking.

Fig. 1.2 plots C_{44}/C_{33} vs. c/a for a number of solids, some of which are known to kink and others that are not. Based on this map it is clear that KNE solids lie to the right of the vertical line and hence constitute a huge class of solids.

As noted above, high c/a ratios render non-basal slip prohibitively expensive. Thus only kink band formation - made possible by basal slip - can be activated during deformation. However, at c/a ratios of ~ 1.5, it is possible to activate non-basal slip in addition to basal slip. The IKBs - comprised of basal plane dislocation dipoles - are then activated in the dislocation cell structures developed giving rise to the fully reversible loops observed. The signature of KNE deformation is the large hysteresis loops in the

stress-strain curves.[11,23,31] As the stresses become larger, the hysteresis loops become larger until the samples fail.

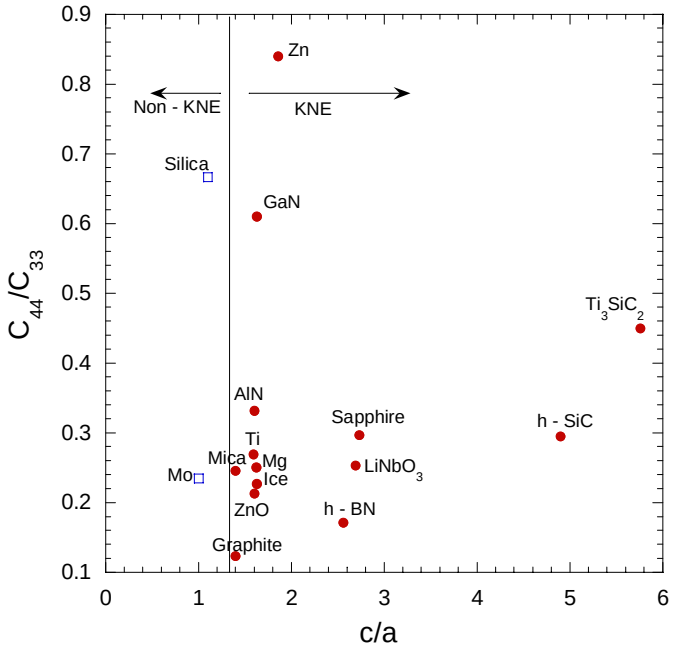

Fig. 1.2 Plot of c44/c33 vs. c/a ratio for different materials. The materials on the right of the vertical line (at c/a ~ 1.4) belong to the group called kinking nonlinear elastic solids.

1.2.2 Kinking Deformation in MAX Phases

The current research was mainly triggered by the unique deformation behavior of the $M_{n+1}AX_n$ - or MAX – phases synthesized in our laboratory, where M is an early transition metal, A is an A-group element, X is carbon and/or nitrogen, and n=1-3. The MAX phases, numbering over 50, are ternary carbides and nitrides that have received considerable attention in the past decade.[28,31-37] The crystal structure of MAX phases is comprised of hexagonal nets of "A" atoms separated by three nearly close-packed "M" layers that accommodate "X" atoms in the octahedral sites between them.[38] Some of these compounds – most notably Ti_3SiC_2 and Ti_2AlC - are promising, lightweight candidates for high temperature structural and other applications. Their electrical and

thermal conductivities are higher than those of Ti metal.[32,34] Despite having a density (~ 4.5 gm/cm^3) comparable to Ti, their stiffness are roughly three times as high,[39] and yet are most readily machinable.[34] With a Vickers hardness of ≈ 3 GPa, they are relatively soft, unusually thermal shock resistant[34,40] and highly damage tolerant.[34,41] Unlike most brittle solids, edge cracks do not emanate from the corners of hardness indentations.[39,41] Rather, intensive kinking, buckling and bending of individual grains take place in the vicinity of the indentations, resulting in pseudo-plastic behavior at room temperature.[41]

More recently it has been shown that polycrystalline Ti_3SiC_2 samples can be cyclically loaded in compression at room temperature to stresses up to 1 GPa, fully recover on the removal of the load, while dissipating about 25 % (0.7 MJm^{-3}) of the mechanical energy.[31] These loss factors are higher than most woods, and comparable to polypropylene and nylon. The stress-strain curves outline fully reversible, rate-independent, closed hysteresis loops that are strongly influenced by grain size, with the energy dissipated per unit volume per cycle, W_d, being significantly larger in the coarse-grained material. In more recent papers it was established that Ti_2AlC,[42] graphite,[12] hexagonal-BN,[11] mica,[11] among many others, have similar deformation behavior. This phenomenon was attributed to the reversible formation and annihilation of incipient kink bands (IKBs), which is why we refer to them as kinking nonlinear elastic (KNE) solids.[30]

1.2.3 Kinking Deformation in Geological Materials

Most of the minerals near the earth's crust are layered and so kink bands can readily be observed in the minerals as reported in the geological literature.[11,13] These minerals also show non-linear elastic deformation behavior, which can be observed as reversible

hysteretic stress-strain curves and hence they have been labeled non-linear mesoscopic elastic (NME) solids. These solids are modeled phenomenologically by invoking the presence of hysteretic mesoscopic units (HMUs), as discussed in Ch. 8, whose physical underpinnings were unknown until recently.

Barsoum et. al. studied the deformation in mica[11] and graphite[12] with both uniaxial compression and nanoindentation and have shown clear evidence of kink bands after the material is deformed. The reversible hysteretic deformation behavior has been explained with the IKB model, which finally gave a physical understanding to the HMUs. Thus IKBs play a much crucial role in the deformation of the earth's crust than hitherto been appreciated.

1.2.4 Microscale Model: Reversible Motion of Dislocations, forming IKBs under spherical nanoindentation

Our recently developed model[30,43] is based primarily on a theoretical paper by Frank and Stroh,[27] (F&S), who considered the problem of the growth of a thin elliptical kink with dimensions 2α and 2β, such that $2\alpha >> 2\beta$ (Fig. 1.1a). Initially, the elliptical kink is comprised of dislocation loops with components of opposite sign, such that the ends are attached and *attracted* to each other (Fig. 1.1a). However, because initially they increase the energy of the system, the kinks are subcritical or unstable. Using an energy approach, reminiscent of Griffith's, F&S showed that the remote shear stress, τ, needed to render a subcritical kink band unstable – and hence grow – depended on α :

$$\tau > \tau_t \approx \frac{\sigma_t}{k_1} \approx \sqrt{\frac{4G^2 b\gamma_c}{2\alpha\pi^2}\ln\left(\frac{b}{\gamma_c w}\right)}, \qquad (1.1)$$

which can be simplified, by assuming w ≈ b, to

$$\tau > \tau_t \approx \frac{\sigma_t}{k_1} \approx \sqrt{\frac{G^2 b \gamma_c}{2\alpha}}\,, \tag{1.2}$$

where b is the Burgers vector; G is the shear modulus (for single crystals, G is replaced by c_{44}); w is related to the dislocation core width; σ_t is the threshold stress and k_1 is a factor (assumed to be 2) relating the remote applied stress to the shear stress. It should be noted here that, during indentation in some materials, k_1 can be higher than 2 – but that will only make a small difference in magnitude of the parameters, described below, and the overall physics will remain the same. This comment notwithstanding, more work is in progress to better understand the scaling factors. γ_c is the critical angle of kinking given by:

$$\gamma_c = \frac{b}{D} \approx \frac{3\sqrt{3}(1-\nu)\tau_c}{2G}, \tag{1.3}$$

where ν is Poisson's ratio, D is the distance between dislocations in the wall (Fig. 1.1a).

Recent *ab initio* and molecular dynamics calculations[44] have shown that dislocations in perfect metal crystals nucleate when the critical shear stress:

$$\tau_c \approx \sigma_c/2 = G/n\,, \tag{1.4}$$

where τ_c and σ_c are the applied shear and normal contact stresses under the indenter, respectively. For polycrystalline metals n is ≈ 30.[45,46] For the single crystals, studied during this work, the appropriate modulus is not G, but c_{44}. Also, as described in later chapters, the fact that in some cases IKBs nucleate at a very high stress implies that n is

much lower than 30. In general, it is not easy to experimentally determine n. The fact that τ_c is close to the theoretical strength of a crystal and can be readily measured here is one of several advantages of using spherical indenters and converting the results to stress-strain curves.

F&S modeled a two dimensional single crystal and assumed, correctly, that once the inequality in Eq. 1.2 was satisfied, the subcritical kink band would rapidly, and autocatalytically, grow to the edge of the sample and dissociate into two parallel mobile dislocation walls (MDW) (Fig. 1.1b). It is the repetition of this process that ultimately leads to the formation of KBs (Fig. 1.1c) that are irreversible.[28,37,47] As shown in the chapters 3 to 8, this behavior is very similar to what happens in a single crystal under the nanoindenter. During the first cycle, most of the energy gets dissipated towards forming MDWs, KBs and/or twin boundaries in the material – which, in turn, act as domains for the formation of IKBs in the material. Thus the reversible hysteretic phenomenon can only be observed during 2nd cycle onwards.[11-13,16-18,48]

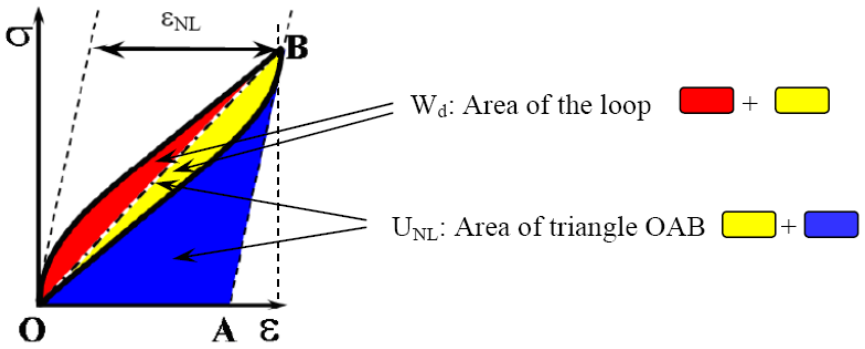

Fig. 1.3 Schematic of the fully reversible cyclic deformation.

An IKB is one in which the ends remain attached (Fig. 1.1a) at the domain boundaries and is therefore *fully reversible* upon the removal of the load.[31] In an IKB, each

dislocation loop can be assumed to be comprised of two edge and two screw dislocation segments with lengths, $2\beta_x$ and $2\beta_y$, respectively. In our model it is assumed that when $\sigma > \sigma_t$, the IKBs grow by increasing 2β, assuming,[27,43]

$$2\beta_x = \frac{2\alpha(1-\nu)\sigma}{k_1 G\gamma_c} \tag{1.5a}$$

for the edge components, and

$$2\beta_y = \frac{2\alpha\sigma}{k_1 G\gamma_c} \tag{1.5b}$$

for the screw components.

Herein we assume that when $\sigma \leq \sigma_t$, the IKB has a finite length of 2α, with widths,[43]

$$2\beta_{x,c} = \frac{2\alpha(1-\nu)\sigma_t}{k_1 G\gamma_c} \quad \text{and} \quad 2\beta_{y,c} = \frac{2\alpha\sigma_t}{k_1 G\gamma_c} \tag{1.6}$$

The nonlinear strain, ε_{NL} due to the growth of these elliptical IKBs is thus given by:[30,43]

$$\varepsilon_{NL} = \frac{\Delta V N_k \gamma_c}{k_2} = \frac{4}{3}\pi\alpha(\beta_x\beta_y - \beta_{x,c}\beta_{y,c})\frac{N_k\gamma_c}{k_2} = \frac{(4/3)\pi(1-\nu)N_k\alpha^3}{k_2 k_1^2 G^2\gamma_c}(\sigma^2 - \sigma_t^2), \tag{1.7}$$

where, ΔV is the change in volume of one IKB, N_k is the number of IKBs per unit volume and, k_2 is a factor (assumed to be 2) for converting local shear strain to the macroscopic linear strain. This is also acknowledged here that more work is needed to understand the value of k_2 for different materials, and their orientations (as indicated in the PM space model studied in Ref 49).[49]

Consequently, the nonlinear energy stored, U_{NL} (Fig. 1.3), is given by,[30,43]

$$U_{NL} = \frac{1}{2}\varepsilon_{NL}\sigma \approx \frac{1}{2}\sqrt{\frac{k_1^2 k_2 G^2 \gamma_c}{(4/3)\pi(1-\nu)N_k\alpha^3}}\ \ \varepsilon_{NL}^{1.5} \tag{1.8}$$

If Ω is the energy dissipated by a dislocation line sweeping a unit area, then the area within each stress-strain loop or energy dissipated per cycle per unit volume, W_d, can be expressed as,[30,43]

$$W_d = 2N_k \frac{2\alpha}{D}\pi(\beta_x\beta_y - \beta_{x,c}\beta_{y,c})\Omega = \frac{4\pi(1-\nu)N_k\alpha^3\Omega}{k_1^2 G^2 b\gamma_c}\left(\sigma^2 - \sigma_t^2\right) \tag{1.9}$$

Combining Eqs. 1.7 and 1.9 yields,[43]

$$W_d = 3k_2\frac{\Omega}{b}\varepsilon_{NL} \tag{1.10}$$

As demonstrated herein and previous work,[11,12,16,17,31,43,49] the formation of fully reversible, reproducible hysteretic stress-strain loops upon cycling is one of the signatures of IKBs. In deriving Eq. 1.9, W_d is assumed to be solely due to the movement of IKB related dislocations; the motion of dislocations in pileups is neglected. Ω/b is a material property that is proportional to, if not identical to, the critical resolved shear stress, CRSS, of basal plane dislocations making up the IKBs.[43] In the case of hexagonal metals we have shown that indeed, Ω/b is $\approx$ CRSS.[43] It should be noted here that Ω/b is related to the ease of moving a dislocation on a particular slip plane and this may potentially vary with the amount of hydrostatic pressure present during the deformation. With that caveat, it is acknowledged that in case of spherical nanoindentation, where a much higher hydrostatic component is present compared to bulk uniaxial experiments, Ω/b can be higher than reported values of CRSS.

1.3 Kinking Nonlinear Elastic Deformation under Spherical Nanoindenter

1.3.1 MAX Phases

In the recent past Murugaiah et. al.[13,23] reported on the load versus depth-of-indentation response of Ti_3SiC_2 surfaces loaded with a 13.5 μm spherical tipped diamond indenter up to loads of 500 mN. Using orientation imaging microscopy, two groups of crystals were identified; one in which the basal planes were parallel to, and the other normal to, the surface. When the load-penetration depth curves were converted to indentation stress-strain curves the following was apparent: when the surfaces were loaded normal to the c-axis, the response at the lowest loads was linear elastic—well described by a modulus of 320 GPa—followed by a clear yield point at approximately 4.5 GPa. And while the first cycle was slightly open, the next 4 on the same location were significantly harder, almost indistinguishable, and fully reversible. At the highest loads (500 mN) pop-ins due to delaminations between basal planes were observed. When pop-ins were not observed the indentations, for the most part, left no trace. When the load was applied parallel to the c-axis, the initial response was again linear elastic (modulus of 320 GPa) followed by a yield point of approximately 4 GPa. Here again significant hardening was observed between the first and subsequent cycles. Each cycle resulted in some strain, but no concomitant increase in yield points. This orientation was even more damage tolerant than the orthogonal direction. This response was attributed to the formation of incipient kink bands that lead to the formation of regular kink bands.[13,31] Remarkably, these dislocation-based mechanisms allow repeated loading of Ti_3SiC_2 without damage, while dissipating significant amounts of energy per unit volume, W_d, during each cycle.

The values of W_d measured were in excellent agreement with corresponding measurements in simple compression tests, confirming that the same mechanisms continue to operate even at the high (~ 9 GPa) stress levels typical of the indentation experiments.[23]

1.3.2 Graphite

Barsoum et. al. reported on the response of graphite single crystals – loaded parallel to their c-axis – to a 13.5 μm radius spherical diamond nanoindenter.[12] Up to loads of 5 mN, corresponding to stresses of ~ 0.5 GPa, fully reversible hysteresis loops are observed. At stresses more than 0.5 GPa, the first loops are slightly open; subsequent loops, in the same location, were fully reversible and harder than the first. Simple compression experiments on polycrystalline cylinders yielded qualitatively similar results. Their results, together with much of the literature on the mechanical properties of graphite,[50] can be explained by invoking the formation of incipient kink bands, IKB's, that give way to mobile dislocation walls that, in turn, coalesce into kink boundaries with increasing stress. The IKB's are fully reversible; the dislocation walls result in plastic deformation, and the kink boundaries explain the hardening. Since the dislocations are confined to the basal planes, they cannot entangle and can thus move reversibly over relatively large distances resulting in the dissipation of substantial amounts (up to 100 MJ/m^3) of energy during each cycle. At stresses more than 1.5 GPa, massive pop-ins—of the order of 60 μm—are observed.[12] Examination of the craters formed provided direct evidence for kink bands and the formation of a multitude of subgrains under the indenter. Based on this work, it is clear that graphite is a member of a larger class of solids –

kinking nonlinear elastic solids[30] – that includes the $M_{n+1}AX_n$ phases, layered silicates, nonlinear mesoscopic elastic solids, among others.

1.4 Goal and Motivation

As described in recent literature one of the reasons behind non-linear elastic deformation is the formation of dislocation-based IKBs.[11,31] Crystals with hexagonal structure show microscopic evidence of the presence of kink bands as can be seen in MAX phases,[23,31] mica,[11] and graphite.[12] Due to the ubiquity of such crystal structures it is of immense interest to understand the *micromechanisms* of the formation and propagation of these dislocation bands. Also, from Fig. 1.2, it is evident that some proposed KNE solids (such as ZnO, $LiNbO_3$, sapphire, GaN) also belong to the so-called *brittle ceramics* category. Hence, the motivation for this project is mainly two-fold. First, it is important to generate the representative indentation stress-strain curves for different materials, using the spherical nanoindentation technique, and correlate the behavior with underlying dislocation based deformation behavior. The stress-strain curves will be informative for understanding the micro-mechanics of deformation and, more importantly, for designing novel experiments where the macro-scale deformation theories (e.g. elastic/plastic anisotropy, creep etc.) can be validated at smaller length scales. Second and as important pertaining to the current project, is to demonstrate the kinking nonlinear elastic behavior in hexagonal brittle solids at micro/nano-scale and correlate the experimental results with our microscale dislocation-based theoretical model, discussed before. It is also important from a design point of view to understand the structural

changes occurring during nucleation and growth of IKBs and their transformation to KBs and how these changes affect structural properties of KNE solids.

Consequently, in a broader sense, the purpose of this research is to investigate the following:

A. Micromechanisms of the dislocation based deformation behavior during the nucleation and growth of IKBs and KBs in brittle KNE solids; and

B. Design of novel micro/nano-mechanical characterization techniques for measuring room temperature time-dependent deformation in brittle solids and correlate the behavior with macro-scale models.

This study will not only lead to a better understanding of the deformation mechanisms observed in KNE solids, but also enhance our capability to design more efficient and robust devices both at macro and micro scale.

1.5 Structure of the Thesis

The current research, and hence the thesis, is designed in the following way to achieve the above mentioned goals and to gain more insights into micro/nano-mechanical deformation of materials, specially hexagonal crystalline so-called brittle materials.

The next chapter (Ch. 2) will discuss the details of determining indentation stress-strain curves from the load-displacement data, including a proposed technique to correct for the effective zero-point of contact during the experiments.

Once the indentation stress is determined from the load-displacement data, it can potentially be controlled to achieve more insight into the deformation of the material. As per one of our goals to understand the kinking non-linear elasticity at micro-scale in materials, we considered single crystals of five different materials, from Fig. 1.2.

The first one is ZnO (Ch. 3), where the c/a ratio is ~ 1.6 and also has a low shear modulus, c44, of ~ 45 GPa. The response of two different orientations, C (0001) and A $(11\bar{2}0)$, to spherical nanoindentation are discussed.

Chapter 4 discusses a novel technique to control the indentation stress for extended periods of time, to determine room temperature creep deformation in ZnO single crystals, specially the A orientation. This chapter is a powerful example of the potential for calculating indentation stress-strain curves and comparing micro-scale deformation of materials to existing macro-scale theories.

The second material is $LiNbO_3$ (Ch. 5), where the c/a ratio is high (~ 2.69) but has a low c44 of ~ 59.5 GPa. Again, both C and A orientations are characterized. In the C orientation, the largest nonlinear hysteresis, during cyclic spherical nanoindentation, has been observed; and, for the first time the micro-scale model for kinking non-linear elasticity (see above) is applied to the nanoindentation data.

Chapter 6 discusses the nanoindentation results on C and A orientations of free-standing epitaxial GaN films. GaN has a c/a ratio of ~ 1.63 but it has a very high shear modulus, c44, of ~ 241 GPa.

The fourth material discussed, in Ch. 7, is sapphire (Al_2O_3), where both the c/a ratio (~2.73) and c44 (~148 GPa) are high.

Chapter 8 discusses the spherical nanoindentation deformation behavior in different grades (based on their initial defect concentration) of mica (c/a ≈ 1.4, c44 ≈ 15 GPa) single crystals. This chapter, being a continuation of our earlier work,[11] focuses more on the effect of initial defect population and delaminations on the deformation behavior in mica.

Lastly, Ch. 9 summarizes the findings in different materials and correlates the deformation behavior with the material parameters. This chapter also discusses the future directions pertaining to the current research.

CHAPTER 2: CONVERTING SPHERICAL NANOINDENTATION RESULTS INTO INDENTATION STRESS-STRAIN CURVES

2.1 Introduction

As discussed in Ch. 1 and demonstrated herein, information regarding the elastic to plastic transition at micro/nano-scale can be readily obtained using spherical indenters.[3,6,14] To do so, however, use is made of the continuous stiffness measurement, CSM, technique,[2] with which, it is possible to apply a load to the indenter tip, while simultaneously superimposing an oscillating force, with force amplitudes that are roughly an order of magnitude smaller than the nominal load.[51] This technique is thus capable of accurately measuring the contact stiffness at every load and eliminates the need to carry out multiple loading-unloading measurements, as described in the Field and Swain method,[3,52] to calculate the variations in hardness and moduli values with load and displacement into the surface.

Despite the use by some of spherical nanoindenters[3,6,20,21,52,53] – and the ease by which the load can, in principle, be converted to stress - as far as we are aware, there has been little effort in trying to systematically study and convert nanoindentation load-displacement results to their corresponding stress-strain curves.

The objective of this work is to apply a variation of the Herbert et al.[20] technique to a number of quite different solids, viz. amorphous silica,[24] polycrystalline aluminum, Al,[24] iron, Fe,[24,54] and single crystals of sapphire[16] and ZnO.[17] In all cases, the results were compared to the moduli reported in the literature and those measured using the Oliver and Pharr[2] method and a Berkovich indenter. The hardness values obtained here were, in turn, compared to the results obtained using Vickers and Berkovich indenters. We show herein that this approach is quite powerful and versatile.

2.2 Spherical Indentation Model

Typically, a nanoindentation test results in load (P) and displacement into the surface (h_t) data. Additionally, the CSM attachment provides the harmonic contact stiffness (S) values over the entire range of loading. The vast majority of spherical nanoindentation data analysis is based on the Hertz equation in the elastic region: [1,3,6,14]

$$P = \frac{4}{3} E^* R^{1/2} h_e^{3/2}, \tag{2.1}$$

where R is the radius of the indenter, h_e is the elastic distance into the surface (Fig. 2.1) and E* is the system composite modulus given by:

$$\frac{1}{E^*} = \frac{1-\upsilon^2}{E} + \frac{1-\upsilon'^2}{E'}, \tag{2.2}$$

where E' and υ', respectively, refer to the modulus and Poisson's ratio of the diamond indenter (1140 GPa and 0.07). The other terms refer to those of the sample.

For a rigid spherical indenter, Sneddon[55] showed that the *elastic* displacements of a plane surface above and below the contact circle are equal, and given by,

$$h_e = h_t = \frac{a^2}{R}, \tag{2.3}$$

where a is the contact radius during indentation (Fig. 2.1). Combining Eqs. 2.1 and 2.3 yields,

$$\frac{P}{\pi a^2} = \frac{4}{3\pi} E^* (\frac{a}{R}) \tag{2.4}$$

The left hand side of the equation represents the indentation stress or mean contact pressure, also referred to as the Meyer hardness.[14] The expression in parentheses on the right-hand side represents the indentation strain.[14] Henceforth, these will be referred to as indentation stress and indentation strain, respectively. Note these are not same as the stresses and strains measured in uniaxial compression tests.

In the remainder of this section we outline a method by which a can be calculated from a knowledge of P, S and the total displacement of the indenter into the surface, h_t, first in the elastic regime, and then in the elasto-plastic regime.

2.2.1 Elastic Regime

Both the Oliver and Pharr[2] and Field and Swain[3] methods use the slopes of the initial portions of the unloading curves, dP/dh, to calculate h_e. Differentiating Eq. 2.1 with respect to h yields:

$$\frac{dP}{dh} = 2E^* R^{1/2} h_e^{1/2}, \tag{2.5}$$

which when substituted in Eq. 2.1, results in:

$$P = \frac{2}{3}\frac{dP}{dh}h_e \tag{2.6}$$

Therefore,

$$h_e = \frac{3}{2}P\frac{dh}{dP} \tag{2.7}$$

Since dP/dh is nothing but the stiffness, S*, of the system comprised of the specimen and the load frame, the stiffness of the material itself can be calculated from

$$\frac{1}{S} = \frac{1}{S*} - \frac{1}{S_f}, \tag{2.8}$$

where S_f is the load-frame stiffness, which in our case is ~ 5.5 MN/m. This value is the one obtained from the instrument manufacturer. Replacing $\frac{dP}{dh}$ in Eq. 2.8 with S, one obtains:

$$h_e = \frac{3}{2}\frac{P}{S} \tag{2.9}$$

Once h_e is known, *a* is calculated from Eq. 2.3.

2.2.2 Elasto-Plastic Regime

Again following Oliver and Pharr[2] and Field and Swain[3] we assume the "contact depth", h_c, defined as the distance from the circle of contact to the maximum penetration depth (Fig. 2.1) to be given by:

$$h_c \approx h_t - \frac{h_e}{2} \tag{2.10}$$

Combining Eqs. 2.9 and 2.10 yields:

$$h_c = h_t - \frac{3}{4}\frac{P}{S} \tag{2.11}$$

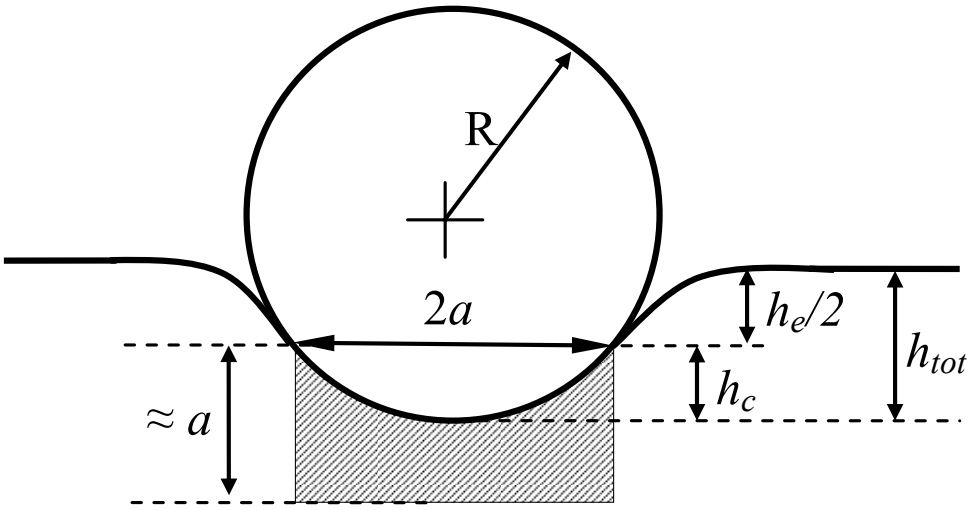

Fig. 2.1. Schematic representation of spherical indentation.

For reasons discussed below, we modified this equation to read:

$$h_c = h_t - \frac{3}{4}\frac{P}{S} \pm \delta\,, \tag{2.12}$$

where δ is an adjustable parameter of the order of a few nm, discussed below.

Once h_c is known, *a* can be calculated from:

$$a = \sqrt{2Rh_c - h_c^{\,2}} \;\approx \sqrt{2Rh_c} \tag{2.13}$$

Note the right-hand expression is only valid if h_c « a, and the indenter tip is perfectly spherical. In the purely elastic regime, $h_c = h_t/2 = h_e/2$ and Eq. 2.3 and Eq. 2.10 become identical. Also note that, for the most part, in the plastic regime, since $h_t >> h_e/2$ and thus $h_c \approx h_t$ (Eq. 2.10).

For an *isotropic* elastic solid, indented with a spherical indenter,[2]

$$S = 2E^{*}a \tag{2.14}$$

It is important to note here that, in principle for an isotropic solid, an S vs. a curve should be linear and it should go through the origin. Equation 2.14 is key to our work as it enables us to correctly, and objectively, determine the value of δ, mentioned above, by measuring the goodness of fit of the experimental data to a straight line passing through the origin (see below).

To date the most commonly used method for measuring nanoindentation hardness values is the Oliver and Pharr method, in which h_c is calculated from Eq. 2.11, and the contact area, A, is determined from a calibrated area function of the form:[2]

$$A(h_c) = C_0 h_c^2 + C_1 h_c + C_2 h_c^{1/2} + C_3 h_c^{1/4} + C_4 h_c^{1/8} + ... \tag{2.15}$$

In this work we calculate *a* from Eq. 2.13. The validity of the results are then judged by two simple criteria: First, that the initial portion of the indentation stress-strain curves be linear, with a slope corresponding to the elastic modulus – which is verified with the slope obtained from Eq. 2.14, the one measured by the standard method, viz. a Berkovich indenter and the Oliver and Pharr method, and also from known elastic constants.

Second, that the stress level at higher strains (~ 20 %) corresponds to the stress measured on the *same* material using a Vickers microhardness indenter.

2.3 Theoretical Elastic Modulus from Elastic Constants

The elastic modulus along a particular direction in a crystal can be obtained from the components in the compliance, S, matrix. For example, for a hexagonal crystal system, the compliance matrix can be written as,

$$\begin{bmatrix} S_{11} & S_{12} & S_{13} & 0 & 0 & 0 \\ S_{12} & S_{11} & S_{13} & 0 & 0 & 0 \\ S_{13} & S_{13} & S_{33} & 0 & 0 & 0 \\ 0 & 0 & 0 & S_{44} & 0 & 0 \\ 0 & 0 & 0 & 0 & S_{44} & 0 \\ 0 & 0 & 0 & 0 & 0 & S_{66} \end{bmatrix}$$

And, the elastic modulus for the [0001] direction will be $1/S_{33}$. As mentioned above, the value of elastic moduli, obtained from the slope of Eq. 2.14 for different materials and different orientations, are compared to the theoretical values from the compliance matrix. In tensor notations, the compliance matrix can be represented by S_{ij}.

In many instances, the stiffness, C, values are reported instead of compliance; and the stiffness matrix can be represented by C_{ij}. The stiffness matrix will also have a similar structure as above,

$$\begin{bmatrix} C_{11} & C_{12} & C_{13} & 0 & 0 & 0 \\ C_{12} & C_{11} & C_{13} & 0 & 0 & 0 \\ C_{13} & C_{13} & C_{33} & 0 & 0 & 0 \\ 0 & 0 & 0 & C_{44} & 0 & 0 \\ 0 & 0 & 0 & 0 & C_{44} & 0 \\ 0 & 0 & 0 & 0 & 0 & C_{66} \end{bmatrix}$$

where, the five independent parameters are C_{11}, C_{12}, C_{13}, C_{33} and C_{44}; and, C_{66} can be calculated from,

$$C_{66} = \frac{(C_{11} - C_{12})}{2} \tag{2.16}$$

Once the complete stiffness matrix is known, it can be easily inversed to obtain the compliance matrix.

2.4 Experimental Details

The nanoindenter (XP System, MTS, Oak Ridge, TN) used in this work was equipped with a CSM attachment. The harmonic displacement for the CSM was 2 nm with a frequency of 45 Hz. The tests were carried out to various loads for different materials depending on their hardness. Once the surface is detected, the indenter is loaded at a constant value of $(dP/dt)/P = 0.1\ s^{-1}$ (the loading rate divided by the load),[2] which has the advantage of logarithmically scaling the data density so that there are just as many data points at low strains than as high. Constant $(dP/dt)/P$ tests have the advantage of producing approximately a constant indentation strain rate, $(dh/dt)/h$, provided the hardness is not a function of the depth.[56]

Two diamond spherical tips - with radii of 13.5 μm and 1 μm - were used. As noted above we used a number of materials: fused silica (GM Associates Inc., Oakland, CA); sapphire single crystal (C-orientation) (Kyocera Industrial Ceramics, Vancouver, WA); C-orientation ZnO single crystal (Wafer World, Inc., West Palm Beach, FL) and two metals: Al (Puratronic 99.999%, Alfa Aesar, MA) and Fe (99.99 % Alfa Aesar, MA).

In all cases, the Vickers microhardness values of the same surfaces used for the nanoindentations were measured using a microhardness indenter (M-400 Hardness Tester, LECO Corp., St. Joseph, MI) and a 10 N load. We also used the Oliver and Pharr[2] method and a Berkovich indenter tip to measure the hardness, H_{Br}, and moduli, E_{Br}, of all samples. As noted above, the latter method will henceforth be referred to as the standard method.

Lastly, to compare the indentation stress-strain curves with those measured in uniaxial compression, a Fe cylinder (9.7mm diameter x 35mm long) was loaded at a nominal stress rate of approximately 13.5 MPa/s. The strain was measured using an extensometer attached to the sample.

2.5 Results

2.5.1 δ–Correction and Effective Zero-point

As discussed above, the real physical significance of the δ-correction is important for better understanding of the initial elastic deformation of materials. It is especially true for materials with lower yield points, viz. metals. After looking at materials with different elastic and plastic properties we came to the conclusion that the δ-correction is related to the determination of the effective zero-point of contact.[54]

For a properly zeroed experiment, according to Eq. 2.14, the S vs. a plot should be a straight line, with a slope of 2E*, and should go through the origin. This is due to an important assumption in Hertzian theory that the sample surface is perfectly flat at the first point of contact between the sample and indenter tip. Unfortunately, this assumption does not hold good for any experimental data as the sample surface always contains a

finite roughness to it. So, it is important to find a correction factor, δ in this case, which can render the experimental data in such a way that it fits with the Hertzian model and provides us with the complete deformation picture for that particular sample. In the following paragraphs, we describe the method of determining the effective zero-point of contact and how it applies to spherical nanoindentation results on fused silica.

2.5.2 Method of Determining the Effective Zero-point for Spherical Nanoindentation

We defined the effective zero-point correction, δ, as the difference in displacement between the correct effective zero point, X_z, and the first point of contact as determined by the instrument, X_0, where S is 200 N/m.[2] To start, we assume different δ_j values (± 10 nm) corresponding to a point X_j, where P definitely becomes positive. For finding the correct effective zero-point, we subtract the values of P_j and $h_{t,j}$ from the P and h_t columns, respectively. Data points with negative h_t values are then discarded and the S vs. a curves are plotted for different δ. The effective zero-point correction will then be the one for which the S vs. a curve best passes through the origin.[54]

To determine the best curve fit, linear regression is used on the S vs. a data. The best fit is then determined from the minimum value of standard error or the maximum value of correlation coefficient, R^2, over the whole range of δ. A detailed explanation of the procedure can be found in Ref. 54.[54]

2.5.3 Effective Zero-point Correction in Fused Silica

Figure 2.6a shows the load-displacement response on fused silica with a 13.5 μm indenter. The as received data is shown in red and the data after δ correction of 7.5 nm

and 15 nm are shown in blue and green, respectively. It is evident from Fig. 2.6a that the difference between the three curves is very small and almost does not have any effect after plastic deformation. But, as mentioned earlier, the effective zero-point correction can make a difference in the very initial elastic part (Fig. 2.6b).

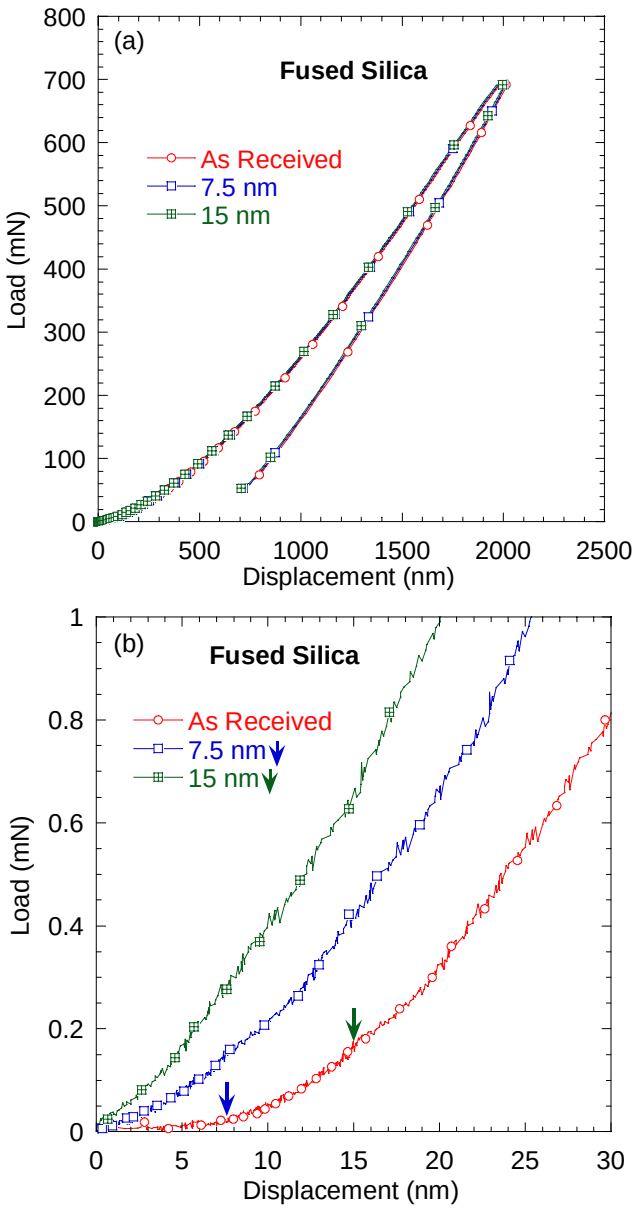

Fig. 2.2. a) Load-displacement curve resulted from a 13.5 μm indent on fused silica. Also plotted are the load-displacement responses after effective zero-point correction of 7.5 and 15 nm. b) Same curves as (a) – only showing the initial loading part. Note the difference in initial load-displacement response after effective zero-point correction.

As determined from the regression analysis described above, the effective zero-point for this dataset is at 7.5 nm shown by the blue arrow in Fig. 2.6b, which also plots the curve with a correction of 15 nm (green arrow) for comparison.

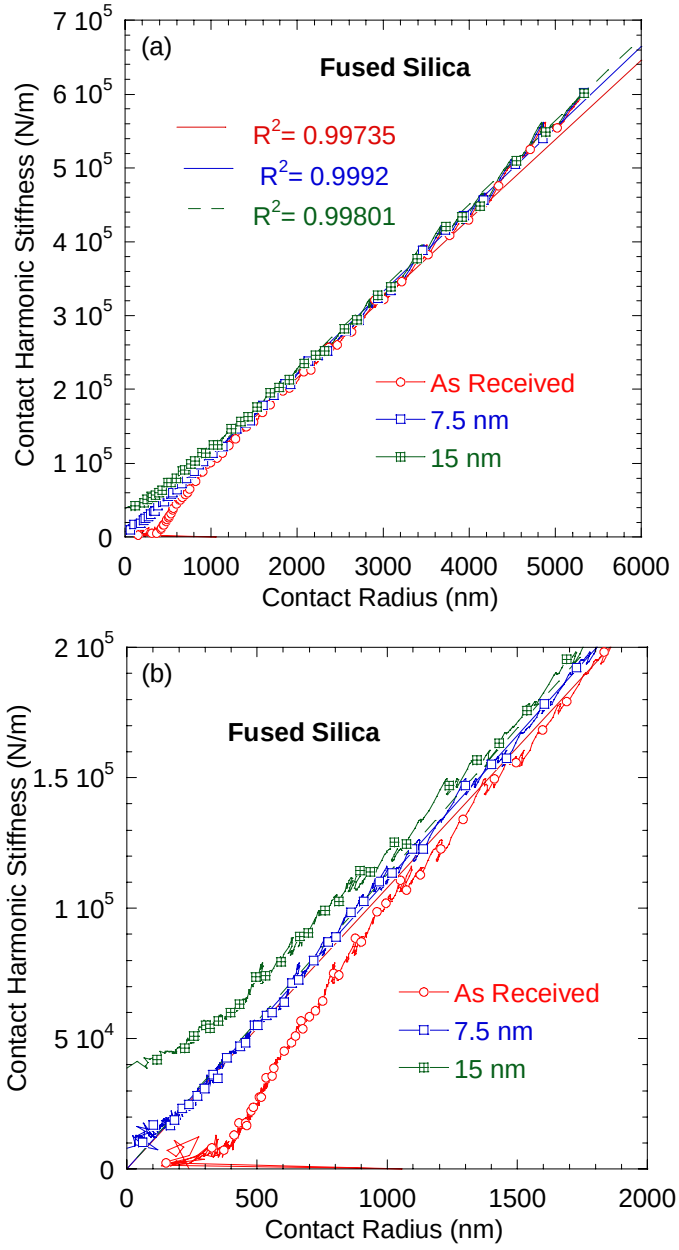

Fig. 2.3. a) S vs. a curve from 13.5 μm indent on fused silica. Also plotted are similar curves after effective zero-point correction of 7.5 and 15 nm. b) Same curves as (a) – only showing the initial elastic loading part. Note the excellent match, between the S vs. a curve and the straight line passing through the origin, after effective zero-point correction of 7.5 nm.

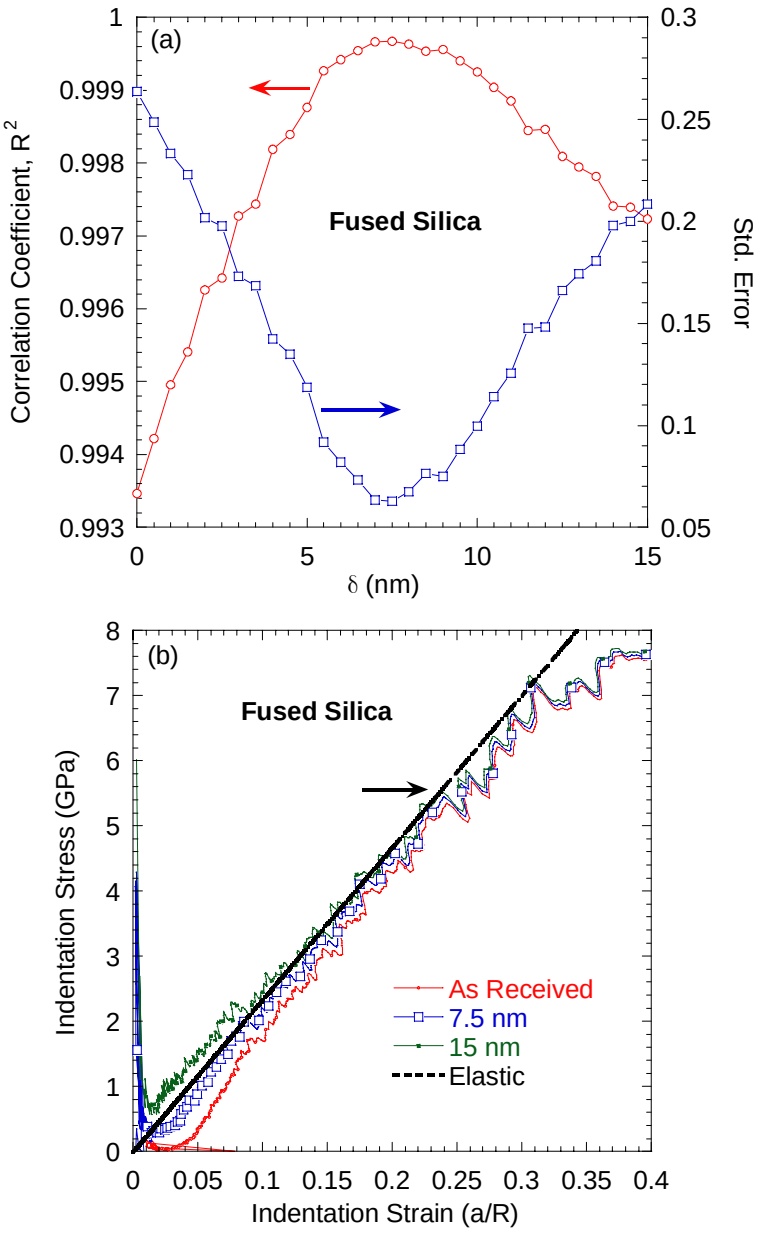

Fig. 2.4. a) The variation in correlation coefficient and standard error for different effective zero-point (δ) correction, obtained from regression analysis of Fig. 2.7. b) Corresponding indentation stress-strain curves before and after the correction. Note the agreement between the initial stress-strain curve, after 7.5 nm correction, with the dashed line representing the elastic behavior. The horizontal arrow shows the approximate yield point for the silica sample.

The difference is more evident in Fig. 2.7a, where the contact stiffness, S, is plotted against the contact radius, a – especially, in the initial elastic part (Fig. 2.7b). The 'as received' data is clearly underestimating while 15 nm is overestimating the effective

zero-point. The blue curve in Figs. 2.7a and b, representing the correct effective zero-point, matches very well with a straight line passing through the origin, giving us confidence in using this method.

The correlation coefficient (or, goodness of fit) and the standard error calculated for each delta correction are shown in Fig. 2.8a. The resulting indentation stress-strain curves (Fig. 2.8b) also show the slight difference made by the effective zero-point correction. As evident from Fig. 2.8b, although the correction is important for the initial elastic part, it almost has no effect on the yield point (horizontal arrow) or the plastic deformation regime of fused silica. However, for a material with lower yield point (e.g. metals) the correction can be crucial. Detailed description of the effective zero-point correction on metals can be found elsewhere.[54]

In the following sections, we follow the effective zero-point correction procedure to obtain the indentation stress-strain curves.

2.5.4 Stiffness vs. Contact Radii Plots and Indentation Moduli

Before plotting the indentation stress-strain curves for the materials, studied herein, it is crucial to determine the effective elastic moduli of the various materials examined.

According to Eq. 2.14, and after the effective zero-point correction, plots of S vs. a resulted in straight lines with slopes proportional to E_{eff} as observed (Fig. 2.5a). (The results for Al are not shown in Fig. 2.5a, since they are almost identical to those for fused silica.) The linearity over the entire loading regime implies that S is *not* affected by pop-ins or plastic deformation, at least for the materials studied in this work. The reproducibility is also noteworthy - each group of results was obtained from multiple

locations - as is the excellent agreement between the slopes obtained using the 1 µm and 13.5 µm indenters on fused silica and ZnO (see Ch. 3). In other words, E_{eff} is not a function of indenter radius, as one would expect.

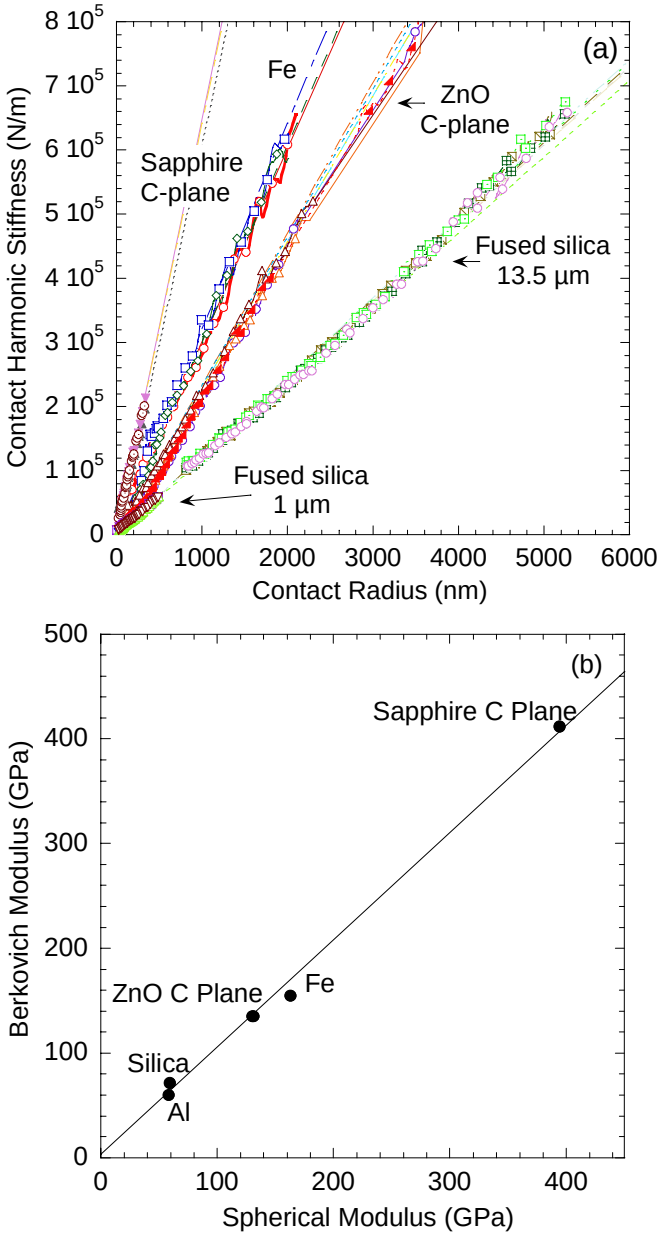

Fig. 2.5. a) Plot of contact harmonic stiffness versus contact radius, as determined from spherical nanoindentation; and b) Comparison of moduli values determined from Berkovich and spherical nanoindentation.

The moduli values calculated from both spherical and Berkovich nanoindentation were also compared in Fig. 2.5b. The linear agreement between the values, for the wide range of solids used during this work, shows the potential for using the spherical nanoindenter in parallel to the more popular Berkovich nanoindenter.

The elastic moduli values calculated from Eqs. 2.2 and 2.14, after the δ–correction, are listed in Table 2.1 as E_{Sp} (column 4) together with the literature data, E, (column 3) and the values determined using the standard method, viz. E_{Br} (column 5). Comparison of the former two sets of results make it amply clear that $E_{Sp} < E$. Similarly, and with the exception of Fe, $E_{Sp} < E_{Br}$.

Table 2.1: Summary of Poisson's ratios, ν, and Young's moduli, E, or $1/s_{33}$ taken from the literature, the moduli values measured in this work using the spherical indenters, E_{Sp}, a Berkovich indenter, E_{Br}, and the hardness values using the latter, H_{Br}. Also listed in last column are the Vickers microhardness values measured herein using a load of 10 N.

Material	ν	E or $1/s_{33}$ (GPa)	E_{Sp} (Fig. 2.2a) (GPa)	E_{Br} (GPa)	H_{Br} (GPa)	Vickers μ-Hard. (GPa)
Silica 13.5 μm	0.18	72	59±1	71.7±0.7	9.3±0.2	5.6±0.6‡‡
SiO_2 1 μm			59±2			
Al 13.5 μm	0.3	70	58±4	60±4	0.48±0.02	0.29±0.02
Fe 13.5 μm	0.3	210 203*	163±9	155±1	1.2±0.1	1.3±0.1
C-ZnO 13.5 μm	0.2	$1/s_{33}$ = 149	130±4	135±3	4.8±0.2	3.3±0.1
C-ZnO 1 μm			131±4			
C-Al_2O_3 1 μm	0.2	$1/s_{33}$= 458	394±4	412±8	25±1	22.5‡

‡ According to manufacturer.
‡‡ This value depends on load; lower loads yield higher values.
* This work.

In the remainder of this chapter we discuss the indentation stress-strain response in fused silica, Fe and Al. The results on single crystal ZnO and sapphire are discussed separately in Chs. 3 and 7, respectively.

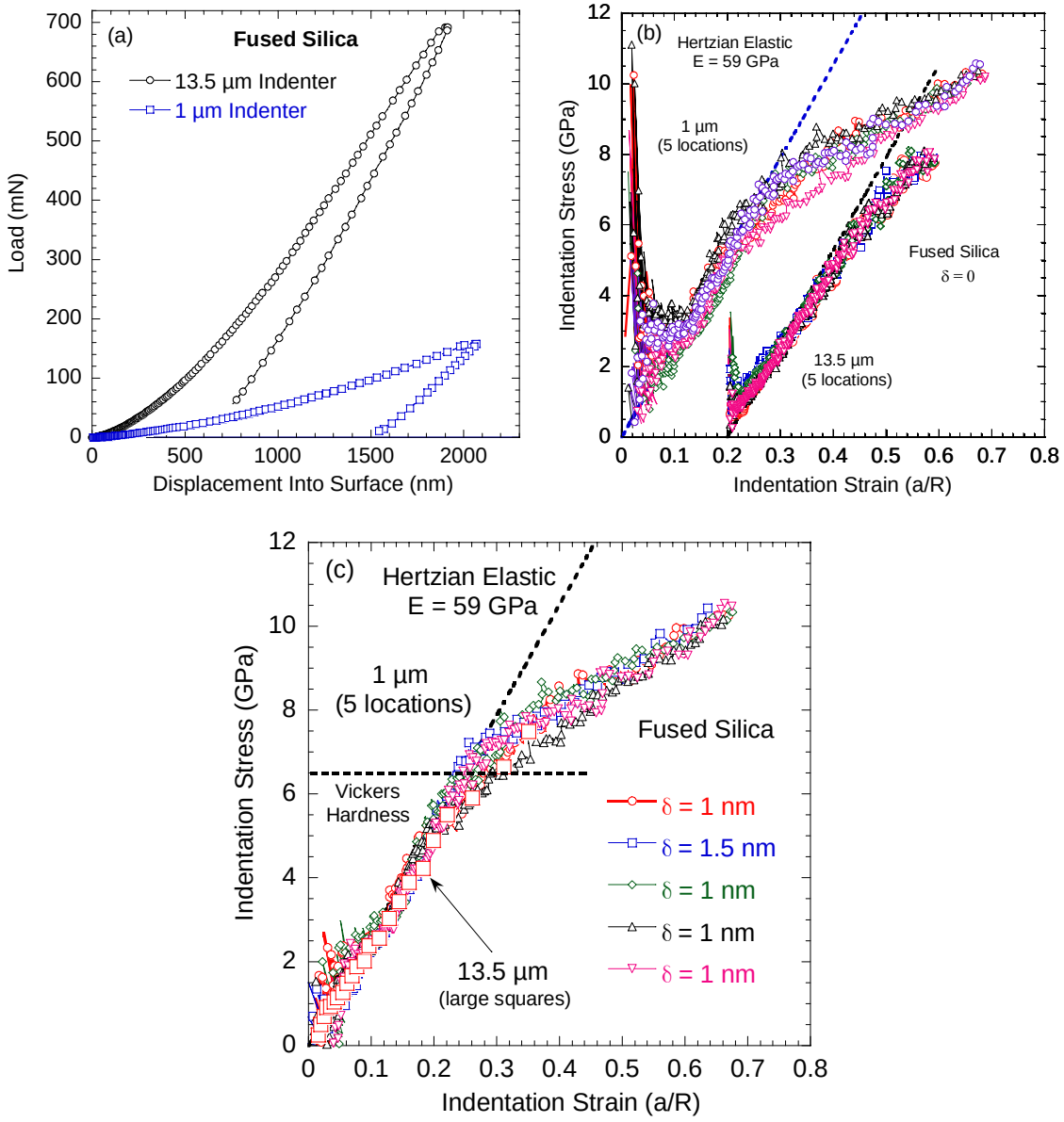

Fig. 2.6. Indentation results for fused silica. a) Load-displacement results for the 1 µm and 13.5 µm indenters used. b) corresponding stress-strain curves with no correction (i.e., $\delta = 0$); the 13.5 µm results are shifted by 0.2 to the right for clarity. c) The same 1 µm results after δ-correction, the values of which are listed. In this figure we eliminated the data points to the left of the dashed line, which represents the elastic response. Also shown is a typical result obtained using 13.5 µm indenter. The agreement between the two sets of results is excellent. Dashed horizontal line represents the Vickers microhardness value measured on the same silica sample.

2.5.5 Fused Silica

To best illustrate our methodology, consider the indentation load-displacement results for fused silica, shown in Fig. 2.6a, for the 1 μm and 13.5 μm indenters. Figure 2.6b plots the indentation stress-strain curves, for 5 different locations, for both the 1 μm and 13.5 μm indenters; the results for the latter were shifted by 0.2, to the right for clarity. The reproducibility of the 13.5 μm results is excellent, those of the 1 μm ones less so, but acceptable, nevertheless. Least squares fits of the S vs. a curve, shown in Fig. 2.5a, yield slopes that correspond to an E_{Sp} = 59±2 GPa (Table 2.1), rather than the established value of 72 GPa measured by the standard method.

Figure 2.6c re-plots the results shown in Fig. 2.6b, after the zero-point correction of the indentation data. The range of δ was quite small, ± 1.5 nm. The curves derived from the 1 μm and 13.5 μm indentations (Fig. 2.6c, open red squares) appear to superimpose onto each other lending great validity to our method. In other words, in the case of fused silica, the results obtained, after the yield point, do not depend on the indenter diameter. (For the sake of clarity only one indentation stress-strain curve, from the 13.5 μm data set, is plotted in Fig. 2.6c. The spread in the results for 5 locations was no more than the widths of 5 symbols across.)

Based on Fig. 2.6c, a clear "yield" point is observed for both indenters at ≈ 6.5±1 GPa. Interestingly, this yield point occurs at a stress that is slightly higher than the 5.6±0.6 GPa obtained from our Vickers microhardness measurements for the same sample at 10 N (higher microhardness values are obtained at lower loads). Whether this is simply coincidental remains to be determined. The nature of the micro-yielding is not

clear at this time, but is most probably related to the densification of the amorphous silica under the indenter.

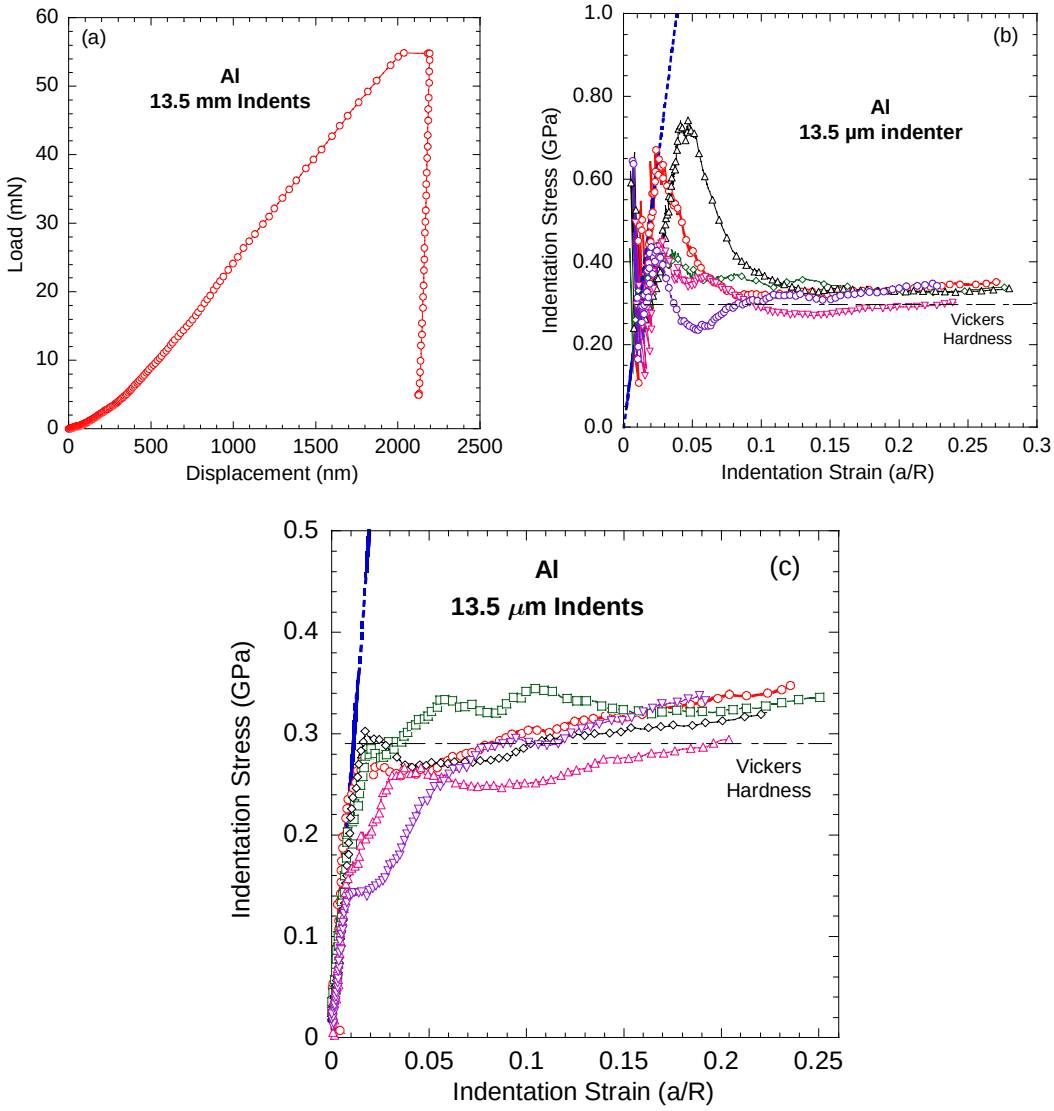

Fig. 2.7. a) Typical indentation load-displacement curve obtained by the 13.5 μm indenter on pure Al. b) Corresponding indentation stress-strain curves at different locations without any correction. c) Same as (b), but after δ–correction (see text). d) Indentation stress-strain curves after the curves in (c) are mechanically shifted to pass through the origin. Dashed horizontal line represents the Vickers microhardness on the same surface and dashed inclined line represents the elastic modulus of 58 GPa.

Note that our method is valid for the 1 μm indenter tip only up to h_t depths of the order of ≈ 300 nm. Above that the tip is no longer spherical and Eq. 2.12 is not valid,

which is why there are no results beyond a strain of 0.7 in Fig. 2.6c. This is not a problem for the 13.5 μm indenter until penetration depths of ~ 4500 nm, but the maximum load applicable was 700 mN (Fig. 2.6a).

2.5.6 Aluminum

A typical load-displacement curve for 13.5 μm indentations of Al is shown in Fig. 2.7a. The corresponding indentation stress-strain results are shown in Fig. 2.7b. While the steady state stresses converge onto the dashed horizontal line representing the Vickers hardness of the same surface (Table 2.1), the initial portions varied from location to location. The zero-point corrections for the results correspond to a δ of about 10 nm, with one exception where δ = 25 nm. The corresponding elastic modulus, calculated from the S vs. a curves, was 58 ± 4 GPa. The indentation stress-strain curves are shown in Fig. 2.7c. In addition to obtaining the elastic modulus, the effective zero-point correction, has the added effect of rotating the initial points in Fig. 2.7b counterclockwise in such a way that they now all fall on the same straight line as the other data points (Fig. 2.7c). The initial hump is also greatly reduced. The reproducibility of the stress-strain curves is noteworthy; especially when it is appreciated that the Al tested was polycrystalline.

The elastic-to-plastic transition for a majority of the curves is sharp and the stresses obtained hovered around the Vickers micro-hardness value measured on the same sample, viz. 0.29±0.02 GPa (Table 2.1).

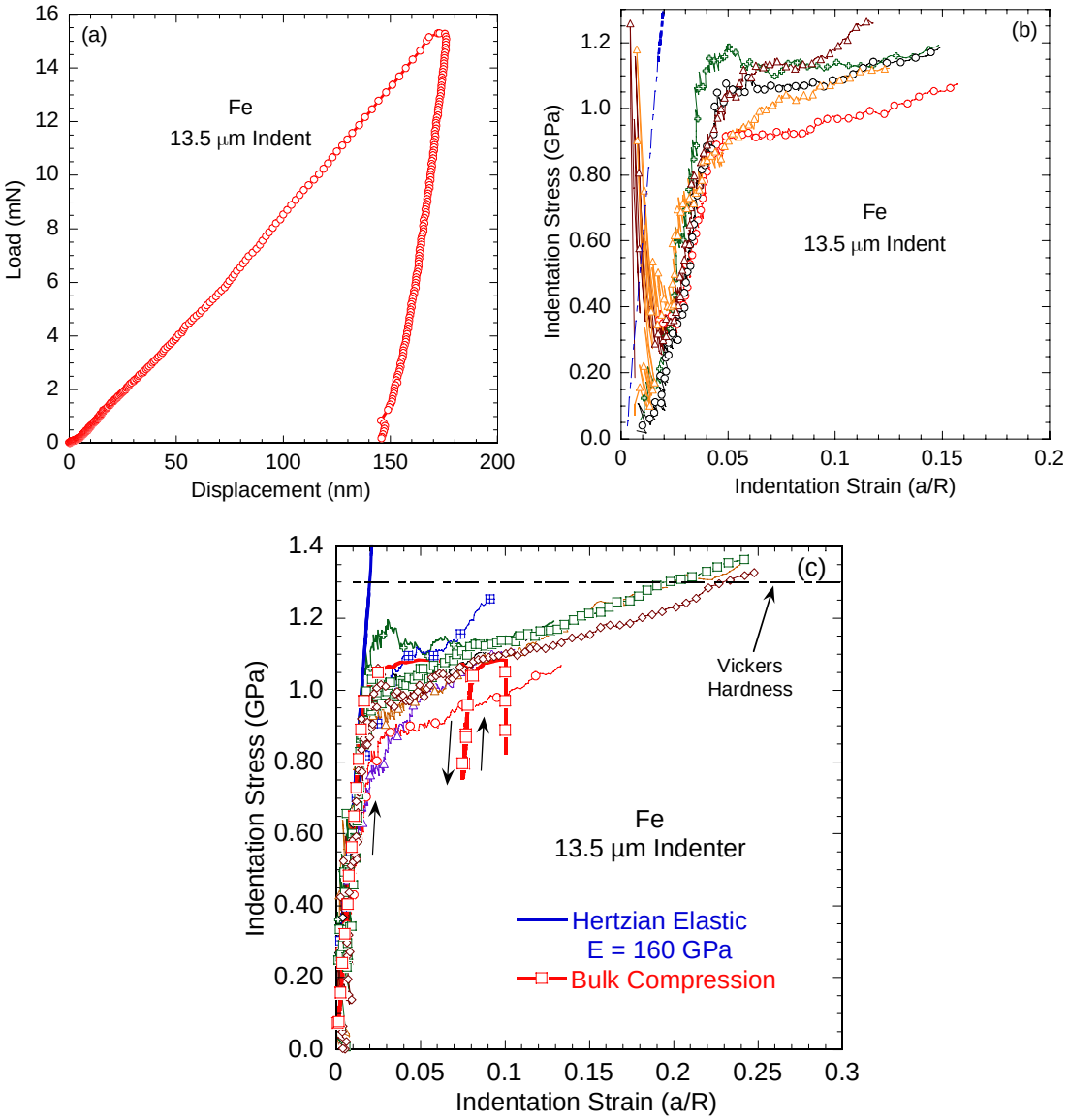

Fig. 2.8. Indentation curves for Fe loaded with a 13.5 μm spherical indenter. a) Typical load-displacement response. b) Indentation stress-strain response at different locations before the δ–correction. c) Same results after δ–correction and mechanical shifting. Also plotted are bulk compression results (open squares) on the same Fe, after multiplying the stress by 3 and strain by 10. The agreement between the two sets of results is excellent. Dashed horizontal line represents the Vickers microhardness measured on the same sample.

2.5.7 Iron

The indentation load-displacement curves and the corresponding indentation stress-strain curves for pure Fe were plotted in Figs. 2.8a and b, respectively. The indentation stress-strain curves – after the effective zero-point correction – are shown in Fig. 2.8c.

At 1.1±0.1 GPa, the steady state hardness values are in reasonably good agreement with the 1.3±0.1 GPa Vickers microhardness values measured on the same sample (horizontal dashed line in Fig. 2.8c). To compare the uniaxial compression results with those shown in Fig. 2.8c we multiplied the former stress by three and the strain by a factor of 10. The agreement between yield values of the two sets of results is surprisingly good.

2.6 Discussion

2.6.1 Critical Analysis of Method

Based on the totality of the results, there is little doubt that our method is a relatively simple way to convert indentation load-displacement results into the much more informative and useful indentation stress-strain curves. The method is versatile and is applicable to Al, as well as sapphire (see Ch. 7), that between them span quite a large moduli and hardness values range. The method is relatively straightforward and, with the effective zero-point correction, devoid of any adjustable parameter and/or any calibration procedure. The approach described herein was not arrived at easily; for over two years we tried and discarded numerous techniques, before choosing the one described herein. Note that for the most part, the same conclusions are reached without the zero-point correction, specially for ceramic materials. For metals, however, the elastic regime is small and a better physical understanding of the effective zero-point correction was needed (Ref. 54).[54]

The usefulness and acceptance of the method proposed here depends on a number of factors, the most important of which is whether the resulting indentation stress-strain

curves yield new information that is reliable, reproducible and meaningful. To answer these questions we compare the results obtained in this work to previous work, with special emphasis on the hardness and moduli values obtained by the standard method.

2.6.2 Fused Silica

It is clear from the results shown in Fig. 2.6c that the indentation stress-strain curves derived from the 1 μm and the 13.5 μm indenters are superimposable, not only at stresses below the ≈ 7 GPa "yield" point, but as important above that value. In other words, for silica we do not observe the indentation size effect that is well documented in the literature and observed in single crystal ZnO (see Ch. 3).[17]

2.6.3 Aluminum

For reasons that are not clear, the moduli values for Al obtained from S vs. a curves, are ≈ 20 % lower than those for pure Al, reported in the literature, and ≈ 4 % lower than E_{Br} (Table 2.1). They are also lower than the value of 70 GPa reported by Herbert et al.[20] essentially using the same technique applied here. In this context, it is important to note here as a caveat that the standard method, used for determining the E_{Br}, calibrates the results to provide a modulus of ~ 72 GPa on fused silica. As mentioned before, the fact that we actually observe a lower modulus on fused silica is consistent with the results on Al. This comment notwithstanding, more work is needed to determine the scaling factor for relating the elastic moduli from spherical nanoindentation to macroscopic Young's moduli.

The hardness values measured herein are also roughly 1/3 of the values reported by Field and Swain[3] for pure Al. The reason for the discrepancy is unclear, but Field and

Swain did not work with the CSM attachment. Also for reasons that are not clear, the indentation stress-strain curves derived by Herbert et al.[20] from spherical nano-indentation experiments on 6066-T1 Al - essentially using the same technique described here - obtained quite different results. In the same paper, the hardness values did not asymptote or reach a steady state, but continually increased with strain. Two possibilities for the discrepancy could be that Herbert et al. used an Al-alloy rather than pure Al and/or the fact that they used much larger spherical indenters. These discrepancies notwithstanding, there is little doubt that our quasi-steady state hardness values, are in good agreement with the Vickers microhardness values measured on the same Al (Fig. 2.7d and Table 2.1), which is comforting.

2.6.4 Iron

For reasons that are not clear, the values of E_{Br} and E_{Sp} we measure for Fe (Table 2.1) are ≈ 30 % lower than the value of 211 GPa reported in the literature, or the 203 GPa we obtained from our uniaxial compression results.

It has long been appreciated that the Meyer hardness,

$$\frac{P}{\pi a^2} \approx 3\sigma_y \,, \tag{2.17}$$

where σ_y is the yield point.[14] It was thus gratifying to obtain the excellent agreement between uniaxial compression results and the indentation results (Fig. 2.8c). Along the same lines, the indentation strain is related to the uniaxial strain, ε, by:[14]

$$\frac{a}{R} \approx 5\varepsilon \tag{2.18}$$

In Fig. 2.8c, a factor of 10 was used instead of 5. The fit is good, in part because the moduli we determine from indentation in the case of Fe are significantly lower than the moduli measured under uniaxial loadings (Table 2.1). The exact relationship between a/R and ε has not been studied in detail to date but is important that it be better understood. This is a fruitful area of research that we are embarking on.

The agreement between the Vickers microhardness values measured here and those shown in Fig. 2.8c has to be considered excellent, given the polycrystalline nature of the Fe and the scatter observed. The scatter is believed to be real and due to the polycrystalline nature of the sample. More careful work, especially on Fe single crystals, is indicated, however, to better understand the subtleties of the elastic-to-plastic transition and the effect of grain boundaries on the local deformation. Note that in this case our Berkovich hardness values are in excellent agreement with our Vickers microhardness results.

2.7 Summary and Concluding Remarks

When load-penetration nanoindentation results, obtained with spherical indenters, are properly converted to indentation stress-strain curves, the latter can provide invaluable information about one of the most important transitions in materials: the elastic-to-plastic transition; information that, as has long been appreciated, is lost when sharp indenters are used.[14] Indentation stress-strain curves can also shed light on work hardening, micro-yielding, or simply whether what is occurring under an indenter is dislocation-based or not. The following chapters discuss, in details, about the micromechanisms of deformation behavior in ZnO (Ch. 3), $LiNbO_3$ (Ch. 5), GaN (Ch. 6), sapphire (Ch. 7) and

mica (Ch. 8) based on the corresponding spherical nanoindentation stress-strain curves. Another potential application of calculating indentation stress-strain curves was to do controlled-stress experiments, which is exemplified in the novel constant-stress creep experiment on $(11\bar{2}0)$ oriented ZnO single crystal (Ch. 4).

In this work we combine the CSM measurements, with Hertzian theory and the Oliver and Pharr method to convert spherical nanoindentation load-displacement curves to indentation stress-strain curves. The results are judged by how closely they match the Vickers microhardness measurements on the same solids, the latter an easy, straightforward, but crucial criteria that, as far as we are aware, has never been previously used in conjunction with nanoindentation results. The correlation that has been observed between the Vickers microhardness and the indentation stress-strain curves is discussed in Ch. 9.

CHAPTER 3: DEFORMATION MICRO-MECHANISMS UNDER SPHERICAL NANOINDENTATION IN ZnO SINGLE CRYSTALS

3.1 Introduction

Single crystal ZnO - a II-VI wide band-gap semiconductor - has received a good amount of attention in the recent past due to its potential application in short wavelength optoelectronic devices due to some advantages over the more popular GaN.[21] For example, ZnO has a simpler crystal growth technology, which translates to a lower cost material. ZnO can also be easily etched in acids and alkalis, providing an opportunity of fabrication of small-scale devices. Recently, ZnO has shown potential for applications in transparent thin-film transistors as well.[57] In all cases, knowledge about its mechanical deformation behavior is of great importance for the manufacture of such devices.

Most of the earlier studies carried out on polycrystalline ZnO with sharp indenters[58,59] provided little information about the deformation behavior of this material. They mostly showed much variability in the hardness (~ 1.5 to 12 GPa) and moduli (~ 40 to 120 GPa) values.[57] More recently, using a combination of spherical nanoindentation and cross-sectional transmission electron microscopy (TEM), Bradby et al.[53] showed that at loads greater than pop-in loads, deformation under the indenter was due to extensive slip on basal and pyramidal planes. In more recent work,[60,61] they reported that the hardness values of A- and C-planes of ZnO were 2±0.2 GPa and 4.8±0.2 GPa, respectively, and

attributed these differences to the different orientations of the basal planes and the ease by which slip can occur along them.

Recently, we have shown that spherical nanoindentation can be an important and powerful tool to characterize the mechanical deformation of single crystals.[11,12,16,23,24] This is especially true since we developed a technique to convert the load-displacement curves to indentation stress-strain curves (Ch. 2).[24] In this work, we apply this technique to understand the response of two different ZnO surfaces to a highly localized stress. Herein repeated spherical nanoindentation, into the same location - of both C (basal) and A (prismatic) ZnO orientations - with two different tip radii were carried out.

3.2 Experimental Details

High quality, bulk wurtzite, ZnO, single crystals were purchased (Wafer World, West Palm Beach, FL) with two orientations: (0001) C-plane and $(11\bar{2}0)$ A-plane. The nanoindentation experiments were performed at room temperature, with a nanoindenter (XP system, MTS Corp, TN) equipped with a continuous stiffness measurement (CSM) attachment. Two diamond hemispherical indenters with radii, R, of 13.5 μm and 1 μm were used. A constant loading rate/load ratio of 0.1 was used. Typically, the tip was indented into the same location at least 5 times at a given load. Post-indentation surface features were examined using a scanning electron microscope, SEM (XL30, FEI Corporation, Hillsboro, OR). We also measured the Vickers micro-hardness (M-400 Hardness Tester, LECO Corp., St. Joseph, MI) using a load, P, of 10 N. The hardness and moduli of the two surfaces were also measured using a Berkovich tip in the nanoindenter.

3.3 Results

3.3.1 C-Plane

Typical nanoindentation load-displacement results for the C orientation obtained with the 13.5 μm indenter are shown in Fig. 3.1a; those with the 1 μm indenter are shown in Fig. 3.1b. The loads at which a sudden displacement burst occurs (or, pop-in loads) are quite stochastic for the 13.5 μm indents. In case of 1 μm indents the variation is much smaller. The contact radius, a, was calculated according to the methodology described in Ch. 2, and the S vs. a curves are shown in Fig. 3.2.

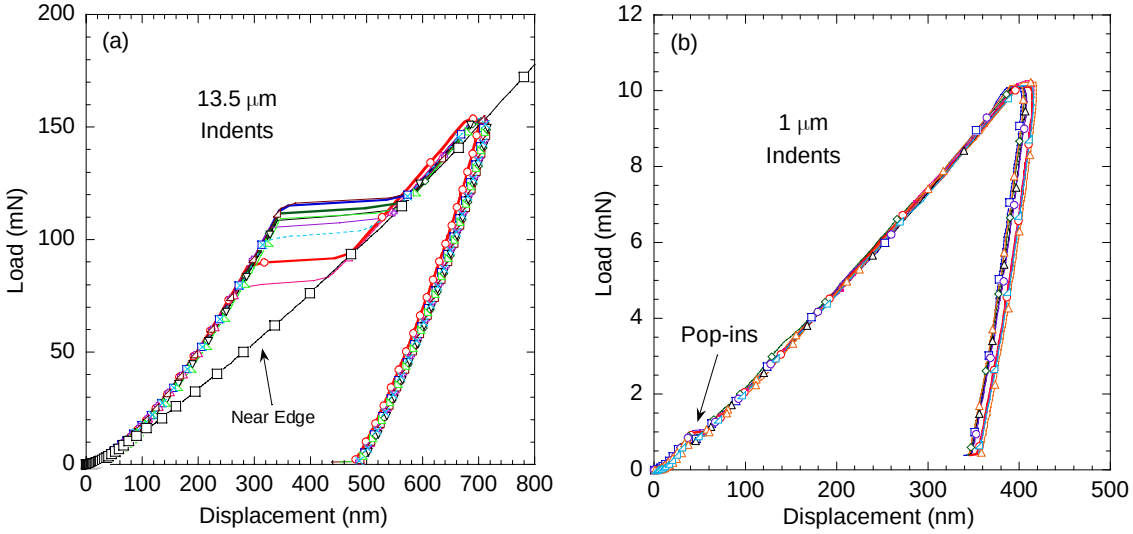

Fig. 3.1. Typical load-displacement results obtained on the C-plane ZnO single crystal. a) 13.5 μm indents; Note stochastic nature of pop-ins. The curve connecting the square symbols trace the load-displacement when the indentation is made near the edge of the sample. b) 1 μm indents. In both cases, only one major popin event is observed during each loading.

It is important to note here that the linearity observed in Fig. 3.2 is gratifying because the data were obtained from two drastically different tip sizes and even with the presence of huge pop-ins during the deformation. In other words, this validates our method for computing the stress-strain results that follow.

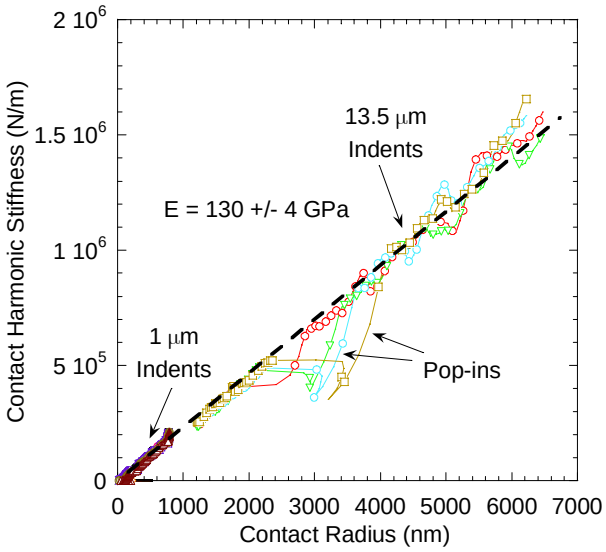

Fig. 3.2. The contact stiffness vs. contact radii plot for the C-plane sample; Note the excellent agreement between the 1 and 13.5 μm indents, and that the linearity is preserved even after huge pop-ins.

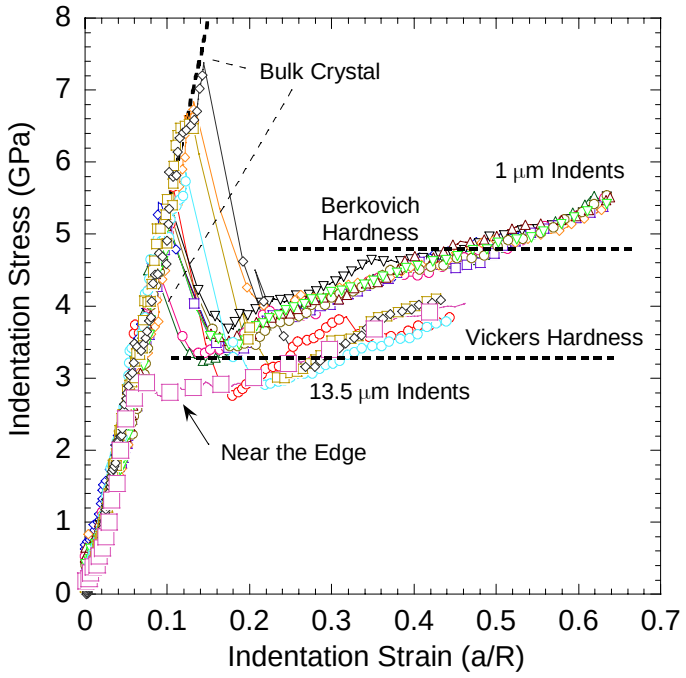

Fig. 3.3. Nanoindentation stress-strain curves obtained when 1 μm and 13.5 μm spherical indenters are introduced into a ZnO C-surface. Dashed horizontal lines represent the hardness values of the same surface measured by a Vickers indenter using a load of 10 N and a Berkovich nanoindenter. The slope of the dashed inclined line corresponds to a modulus of 135 GPa. Note the near disappearance of a popin when the indentation is made near the sample's edge (square symbols).

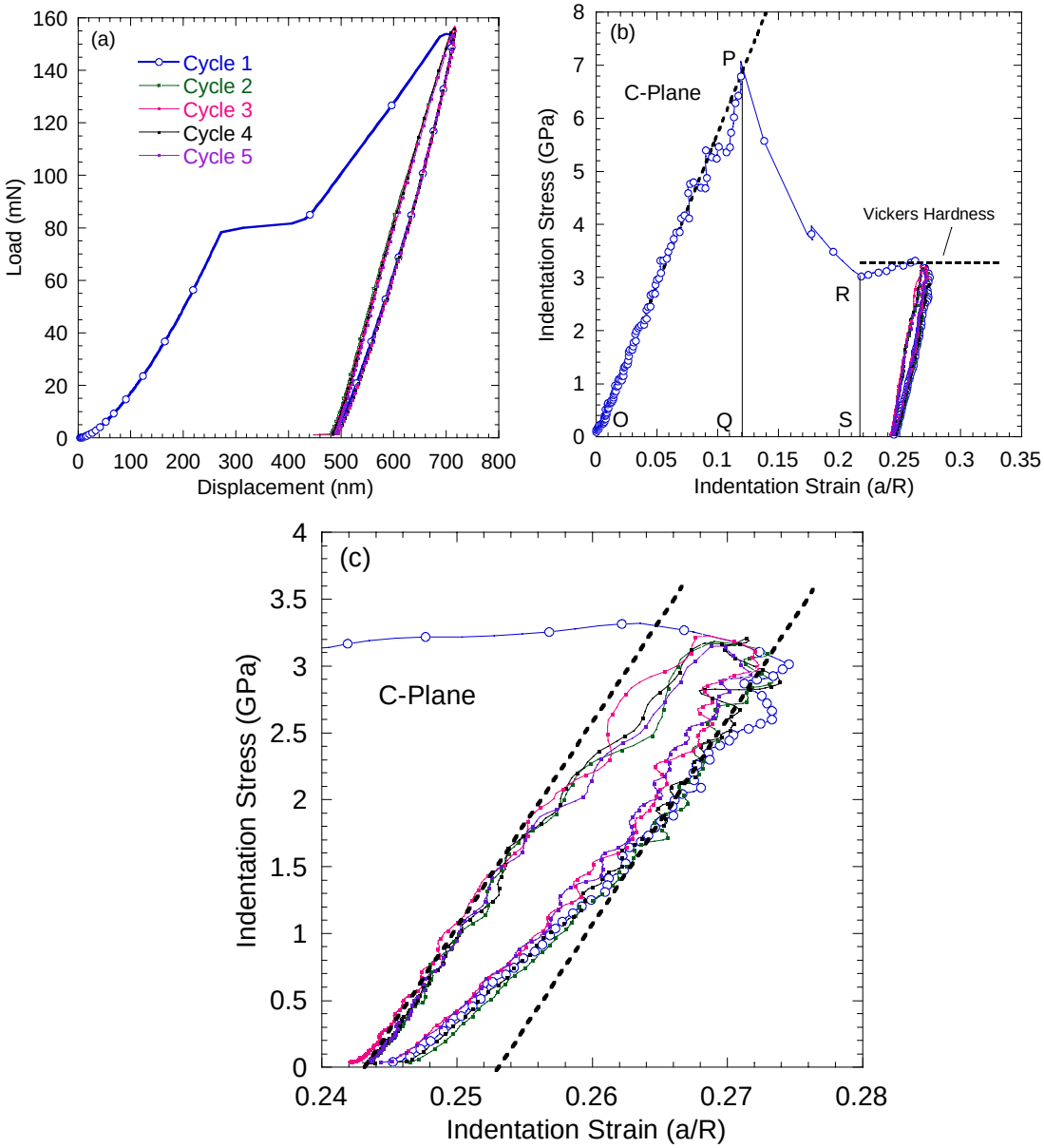

Fig. 3.4. Spherical nanoindentation, a) load-displacement; b) stress-strain curves obtained when a 13.5 μm radius hemisphere is indented five times into the same location, to the same maximum stress, on a ZnO C-surface. Dashed horizontal line represents the Vickers hardness. The slope of the dashed inclined line corresponds to a modulus of 135 GPa; and, c) Magnified view of cycles 2 to 5 in (b). Note fully reversible and reproducible nature of loops. The distance between the two dashed inclined lines represents the nonlinear strain during cyclic deformation.

The C-orientation elastic modulus - determined from Fig. 3.2 and from Berkovich nanoindentation - were 130±4 GPa and 135±3 GPa, respectively. These values are in reasonable agreement with those of Coleman et al.,[60] who reported values of 143±6 for

the C-plane sample. Interestingly, both sets of values are also coincidentally close to the values of $1/s_{33}$ (149 GPa), calculated using the elastic constants for ZnO.[57]

The corresponding stress-strain curves for both 13.5 and 1 μm indents are shown in Fig. 3.3. The dashed horizontal line in Fig. 3.3 represents the Vickers micro-hardness value of 3.3±0.1 GPa, measured herein.

The repeat cycles in the C-orientation are fully reversible and reproducible (Figs. 3.4a and b). It is important to note that fully reversible loops are not observed when plastically isotropic solids, such as fused silica, Al or Fe, are tested (Ch. 2).[24]

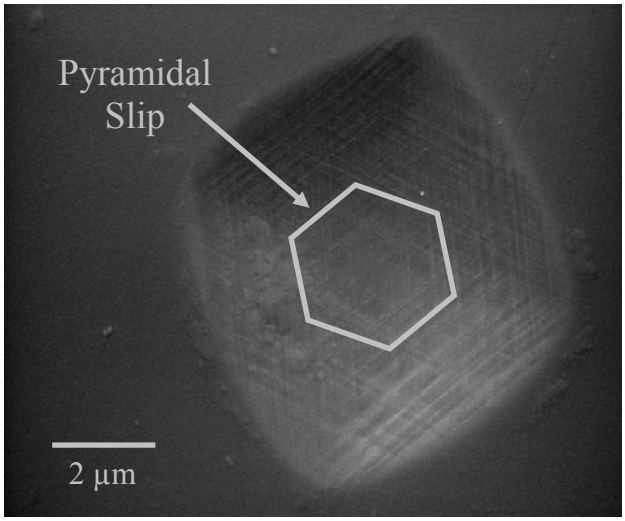

Fig. 3.5. Secondary Electron Microscopy (SEM) image of indented C-plane ZnO surface. The 6-fold symmetry of slip lines is consistent with pyramidal slip underneath the indented region.

The surface features after the C-plane sample was indented with the 13.5 μm indenter are shown in Fig. 3.5. Interestingly, the hexagonal symmetry of slip lines was evident and, as discussed below, was caused by pyramidal slip.

3.3.2 A-Plane

The nanoindentation load-displacement results for the A plane crystal, obtained with the 13.5 µm indenter, are shown in Fig. 3.6a; those with the 1 µm indenter are shown in Fig. 3.6b. In this orientation, the scatter in pop-in loads was higher compared to the C-plane. The S vs. a curves measured with both the indenter tips are shown in Fig. 3.7.

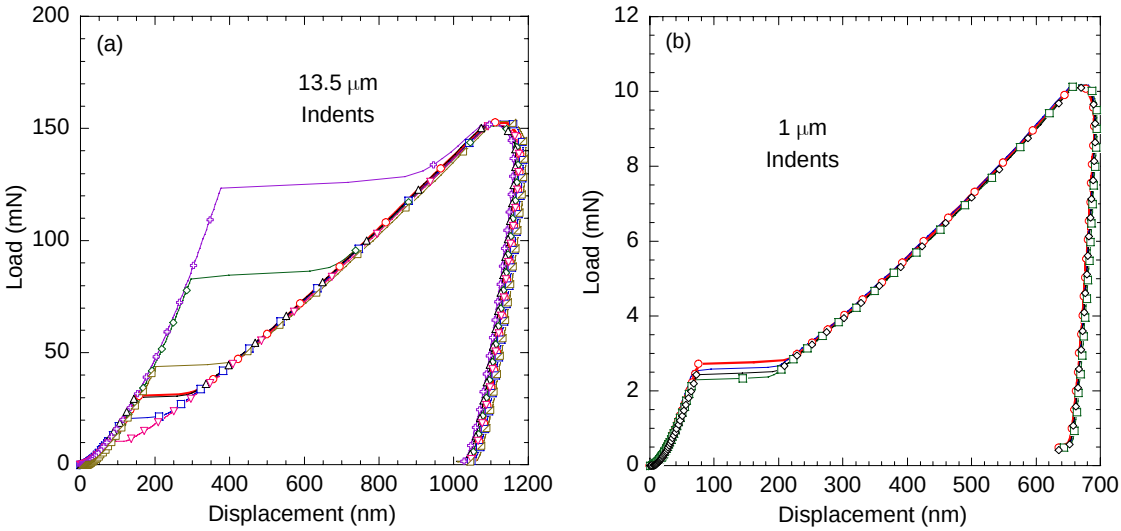

Fig. 3.6. Typical load-displacement results obtained on a A-plane ZnO single crystals. a) 13.5 µm indents; b) 1 µm indents. Note stochastic nature of pop-ins and forward-displacement creep during unloading. Like the C-plane, only one major popin event is observed during each loading.

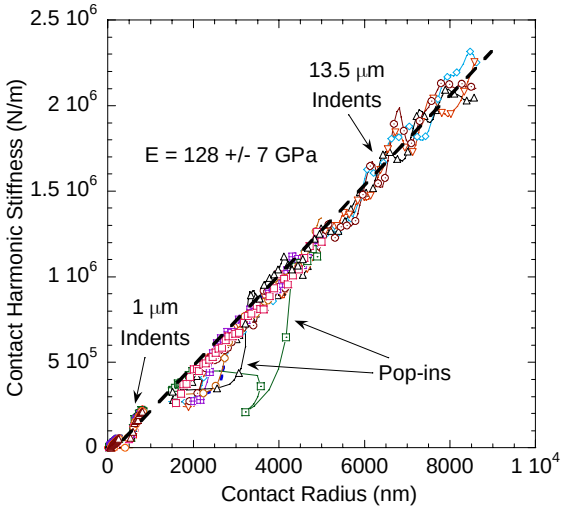

Fig. 3.7. The contact stiffness vs. contact radii plot for the A-plane sample; Note the excellent agreement between the 1 and 13.5 µm indents, and that the linearity is preserved even after huge pop-ins.

The elastic modulus in the A-orientation - determined from Fig. 3.7 and from Berkovich nanoindentation - were 128±7 GPa and 144±4 GPa, respectively. These values are again close to the values from Coleman et al.,[60] who reported a modulus of 163±6 GPa for the A-plane sample. Interestingly, the modulus from the spherical nanoindentation is also coincidentally the closest to the value of $1/s_{11}$ (128 GPa), calculated using the elastic constants for ZnO.[57]

The corresponding stress-strain curves for both 13.5 and 1 μm indents are calculated using the methodology described in Ch. 2 and are shown in Fig. 3.8.

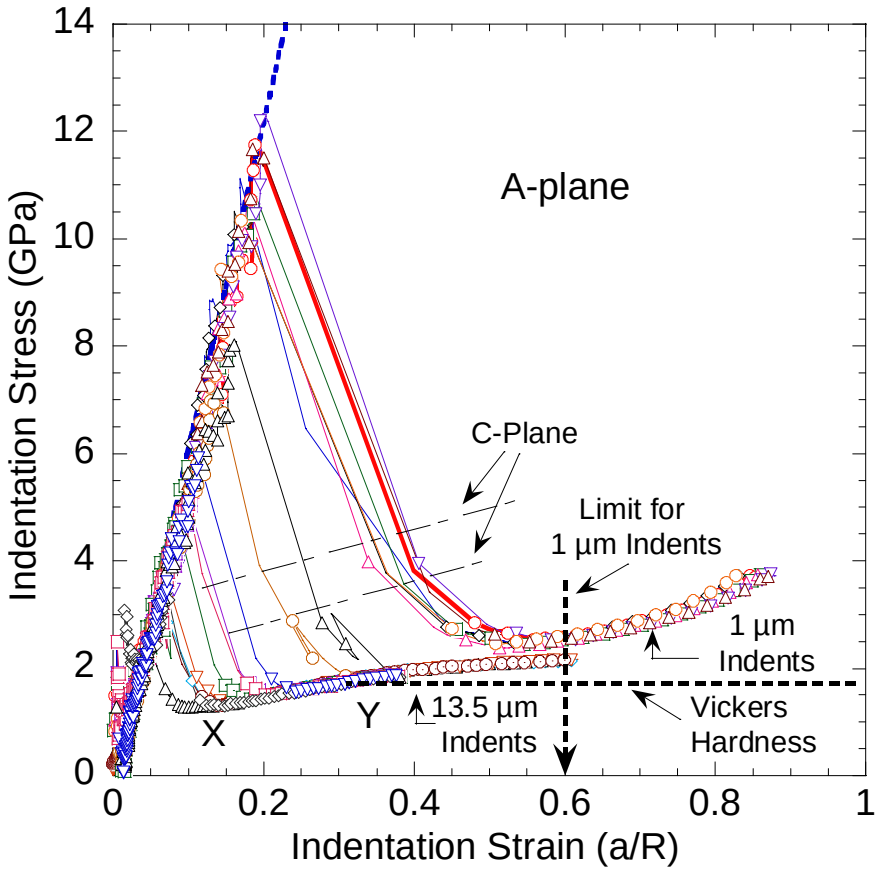

Fig. 3.8. Nanoindentation stress-strain curves obtained when 1 μm and 13.5 μm spherical indenters are introduced into A-surface. Inclined near-horizontal dashed lines are those for the C-plane shown in Fig. 3.3. Dashed horizontal line represents the hardness values of the same surfaces measured by a Vickers indenter using a load of 10 N. The slope of the dashed inclined line corresponds to a modulus of 144 GPa.

The dashed horizontal line in Fig. 3.8 represents the Vickers micro-hardness value – 1.7±0.1 GPa - measured herein. At 2.0±0.2 GPa, the hardness values for the A-surface measured by Coleman et al.[60,61] are also in good agreement with our results. The hardness of the same surface measured by a Berkovich nanoindenter is found to be 2.7±0.1 GPa.

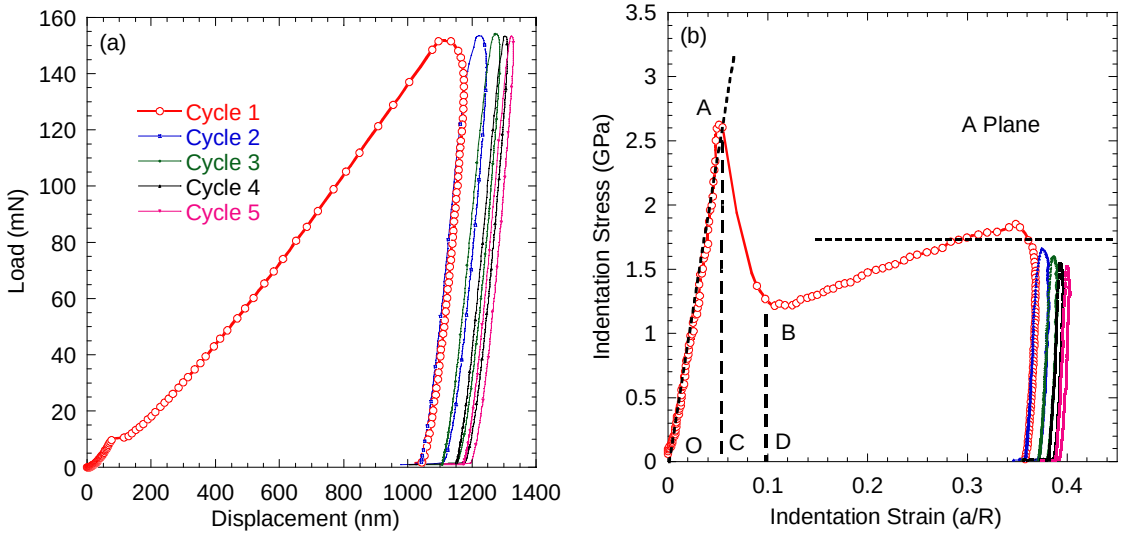

Fig. 3.9. Spherical nanoindentation, a) load-displacement; and, b) stress-strain curves obtained when a 13.5 μm radius hemisphere is indented five times into the same location, to the same maximum stress, on the A-plane surface. Dashed horizontal lines represent the hardness values of the same surfaces measured by a Vickers indenter using a load of 10 N. Note that, unlike the C-orientation, there is no hysteresis in this orientation.

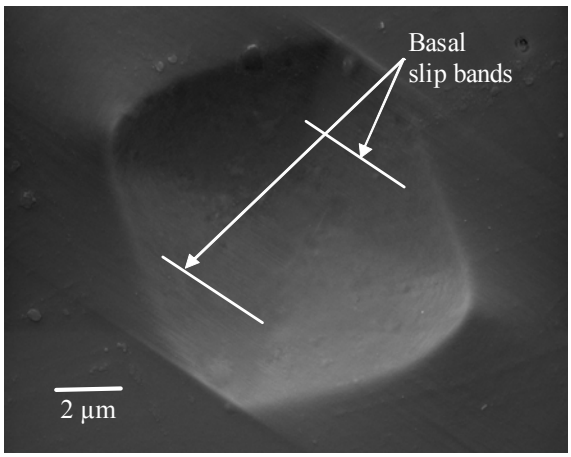

Fig. 3.10. Secondary Electron Microscopy (SEM) images of indented A-plane ZnO surface. The 2-fold symmetry is consistent with basal slip (see Figs. 3.13b and 3.15b below).

The repeat cycles in the A-orientation are shown in Figs. 3.9a and b. In this orientation no reversible hysteresis has been observed and the loops disappear with cycling. The post-indentation surface features are shown in Fig. 3.10.

When the pop-in loads for both the indenter tips are normalized by πR^2, R being the indenter radius, and plotted against the extent of the pop-ins, normalized by R, straight lines result (Fig. 3.11) in which the slopes for the C-direction were ~ 4 times steeper than the A-direction.

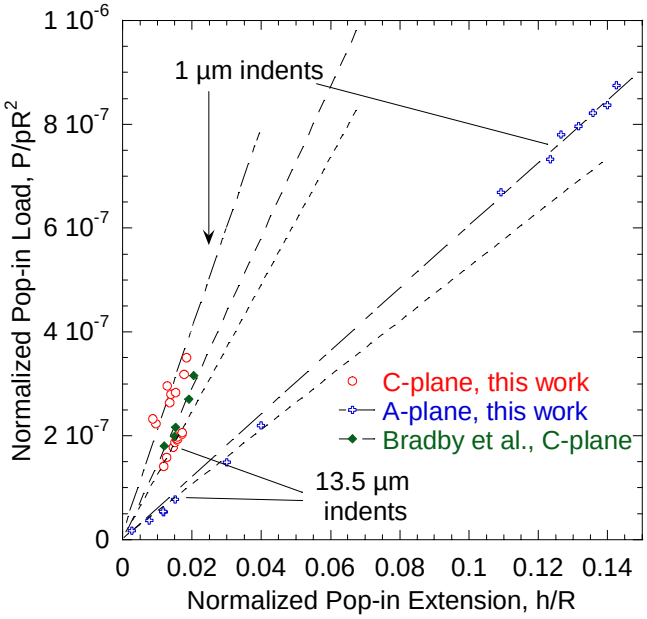

Fig. 3.11. The normalized popin load is plotted against normalized popin extension for both 13.5 µm and 1 µm tips and both C and A-orientations. The results from Bradby et al. on C-plane (Ref. 22)[22] are also shown for comparison.

Bradby et al.[22] have shown that the slopes of such lines scale with hardness. This is clearly confirmed here. For both surfaces, studied herein, the slopes were a function of indenter radius (Fig. 3.11). The effect on the C-plane, however, was more noticeable.

Our results for the C-plane straddle those of Bradby et al.,[22] who used an indenter tip radius of 4.3 μm.

3.4 Discussion

A perusal of the results, presented above, indicates that: i) The C-surface is about twice as hard as the A-surface (Figs. 3.3 and 3.8). ii) The repeat cycles in the C-orientation are fully reversible and reproducible (Fig. 3.4). Similar fully reversible loops were not observed when plastically isotropic solids, such as fused silica, Al or Fe, are tested.[24] The same is true when the stress can be relieved without the formation of IKBs, - as in the case of A-surface, where the loops disappear with cycling (Fig. 3.9). iii) At 12.2±0.6 GPa for the 1 μm indenter and 5.3±1.6 GPa for the 13.5 μm indenter, the pop-in stresses in the A-surface are quite stochastic (Fig. 3.8). The same trend is observed in the C-direction, but the variations are smaller (Fig. 3.3). iv) Not only is the C-surface harder, but, as important, its strain hardening coefficient is also higher (compare slope of dashed lines in the center of Fig. 3.8 that correspond to the C-plane to those of the A-plane). v) In the C-direction the hardness is a function of indenter radius (Fig. 3.3). The effect in the A-direction is either absent or much milder (Fig. 3.8).

To understand the results shown above, we make the following four conjectures. First, the difference in hardness values between the two planes is due to the orientation of basal planes with respect to the indentation axis. Two, the intrinsic flow stresses of the pyramidal dislocations are higher than those for the basal dislocations, and the combination of these two slip systems accounts for the higher strain hardening coefficient of the C-plane. Three, dislocation nucleation is heterogeneous, stochastic, defect

dependant and occurs at the pop-in stress. Four, the strain energy released when the pop-ins occur determine their extent. In the remainder of this chapter evidence for these conjectures is presented.

For the C-plane, the dislocation flow stress, τ_o is 1.25±0.3 GPa (Fig. 3.3); for the A-plane, τ_o is 0.5±0.1 GPa (Fig. 3.8). (Here it is assumed that $\tau_o \approx \sigma_o/2$, where σ_o is the y-axis intersection of the stress-strain curves after the pop-ins). Given that in both cases, at least initially (see below), the same basal plane dislocations are nucleated and move, the difference has to be related to the resolved shear stress on the basal planes which is presumably higher for the A-planes. In other words, we are in agreement with Bradby et. al.[53] and Coleman et. al.[61]

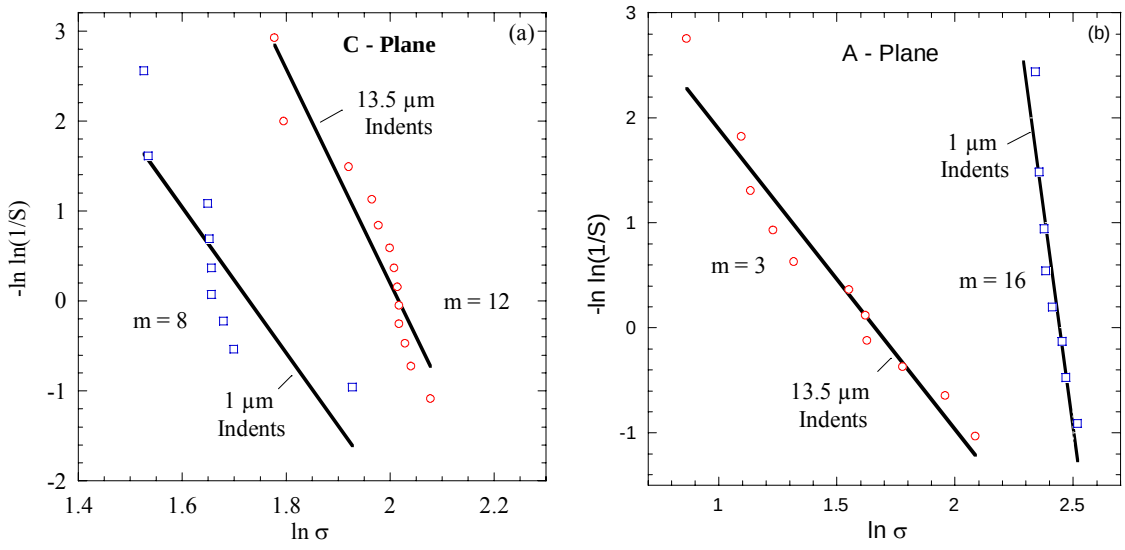

Fig. 3.12. Weibull plots for the popin stresses for the 1µm and 13.5 µm indenters on, a) C-plane; and, b) A-plane. The Weibull moduli, m, are shown on the figures.

Based on Figs. 3.3 and 3.8, there is little evidence for plastic deformation prior to the pop-ins. The wide variations in pop-in stresses thus suggest that dislocation *nucleation* is

the rate-limiting factor in the deformation. Consistent with this interpretation is the fact that the pop-in stresses for the A-surface are a function of indenter radii (Fig. 3.8). Given that the volume probed by the 1 μm indenter is roughly 2500 times smaller than the one probed by the 13.5 μm indenter, it is reasonable to assume that the probability of finding a dislocation-nucleating heterogeneity would be greater under the 13.5 μm indenter. If that were the case the Weibull moduli, m, for both indenters should be comparable. The fact that they are not; at 16 and 3, m for the 1 μm and 13.5 μm indenters (Fig. 3.12b), respectively, in the A-direction (Fig. 3.12b) are quite different we conclude that the difference is probably due to different defect populations, near the surface and deeper in the bulk. The results also suggest, somewhat surprisingly and for reasons that are unclear at this time, that the defect population and size at, or near, the surface may be smaller than deeper in the material. These comments notwithstanding, it is hereby acknowledged more work in needed to better understand the nature of the dislocation nucleating defects.

In contradistinction the difference in the m values - 8 and 12 - for the two indenters in the C-plane (Fig. 3.12a) is smaller, suggesting that in this orientation the defect populations are more comparable with respect to the tip radii.

To confirm the fact that the popin stress is a function of inherent defect population we carried out indentations near (≈ 10 μm) the edge of the crystal, where the defect concentration/population is presumably higher due to machining. The indentation results from the sample's edge (represented by large square symbols in Fig. 3.1a and Fig. 3.3) are indirect evidence that the pop-in stresses are indeed governed by the initial defect population. Moreover, since the 1 μm indenter is probing a much smaller volume, but

results in *lower* average pop-in stresses (Fig. 3.3) and a lower Weibull modulus (Fig. 3.12a), it is fair to conclude that in this case the defects are more densely populated in a thin surface layer, as compared to deeper inside the bulk. The reason for this state of affairs is not clear, but could be related to the polishing of the surfaces. Note, however, that the highest pop-in stresses are of the order of $c_{44}/4$, and thus quite close to the theoretical limit.

The fact that for a given indenter size, the load-displacement curves, *after* the pop-ins, for both surfaces, follow a single trajectory is noteworthy (Figs. 3.1a and 3.6a), because it implies that the evolution of the microstructure under the indenter is quite insensitive to strain rate. For example, in Fig. 3.8, the indentations with pop-ins at X and Y, at a strain beyond Y, fall on the same curve. It is reasonable to assume that the microstructure formed at Y developed at a much higher strain rate than the one that followed the trajectory X to Y. Note that this is consistent with a system in which dislocation nucleation is rate limiting.

As important the energy dissipated during the popin is roughly equal to the strain energy stored in the material just before the pop-in, i.e. resulting from the elastic deformation. This is best seen in Figs. 3.4b and 3.9b. In Fig. 3.9b, it is clear the areas OAC and ABDC are roughly equal. Similarly, area OPQ is roughly equal to area PRSQ in Fig. 3.4b. Said otherwise, during the pop-ins the strain energy is used into nucleating and moving a large number of dislocations. The equality also suggests that relatively little energy is dissipated as heat and/or sound waves. The details of how the strain energy in

converted to cascades of dislocations and why the microstructure under the indenter appears to be insensitive to strain rate are not understood at this moment.

Recently we postulated that most solids with c/a ratios > 1.5 belong to the same class of solids we labeled kinking nonlinear elastic, KNE (Ch. 1).[11,30] Experimentally, the signature of KNE solids is the formation of fully reversible, hysteretic stress-strain loops on repeat loadings to the same stress.[31] As discussed in Ch. 1, this full reversibility is due to the formation of incipient kink bands, IKBs, that are comprised of two nearly parallel, dislocation walls of opposite polarity attracted to each other such that when the load is removed they annihilate. Given that the response of the C-planes to repeated indentations (Fig. 3.4) is indeed fully reversible, we conclude that IKBs are responsible. This response is very similar to the deformation behavior observed in other KNE solids such as layered ternary carbides,[23,31] mica[11] (Ch. 8), graphite,[12] sapphire[16] (Ch. 7), and, more recently, C-plane GaN[48] (Ch. 6) and C-plane $LiNbO_3$ (Ch. 5).[18]

As noted above, high c/a ratios render non-basal slip prohibitively expensive. The results of this work clearly show that at c/a ratios near 1.5 – for ZnO it is 1.6 - it is possible to activate non-basal slip, but only under highly constrained conditions. At ~ 17.3±2.6 MJ/m^3, the energy dissipated per cycle for the C-plane (Fig. 3.4c) is considerable and can only be attributed to to-and-fro motion of dislocations.[31] The other two possibilities – fracture and phase transformation – can readily be ruled out as fracture cannot lead to hardening as observed in Fig. 3.3 and no cracks have been observed on the surface (Fig. 3.5) or in cross-sectional TEM.[53] No evidence of a phase transformation in ZnO, at the stresses reported here, has ever been reported.

To examine the assumptions of our IKB model[30] - embodied in Eqs. 1.1 to 1.10 - we need to estimate γ_c. As noted above, the *threshold* stress for the formation of the initial KBs/dislocations for the C-plane is ≈ 1.25 GPa. Equating this value to τ_c in Eq. 1.3, c_{44} for ZnO to be 45.1 GPa, and consequently, $\tau_c \approx c_{44}/36$, which is not unreasonable, and is what Frank and Stroh[27] estimated that value to be. It is important to note that this value is in the presence of IKB nucleating heterogeneities and/or defects; in the absence of these defects, τ_c can be close to the theoretical limit, viz. $\approx c_{44}/2\pi$.

Thus taking $\tau_c \approx c_{44}/36$ and assuming, $G = c_{44} = 45.1$ GPa, $\nu = 0.2$, and $b = 0.324$ nm,[57] from Eq. 1.3 we calculate $\gamma_c \approx 0.06$. Hence, the distance between two dislocations in a wall, D is ≈ 5.4 nm. In other words, a dislocation is present along the c-axis every ≈ 54 Å. The c-lattice parameter[57] is 5.20 Å and the total length of an IKB, 2α, as calculated from Eq. 1.2, is ≈ 50 nm. In other words, each IKB is comprised of roughly 10 dislocation loops.

The IKB strain, ε_{IKB} - approximated to be the distance between two lines drawn parallel to the initial loading and unloading portions of the reversible hysteretic cycles as shown in Fig. 3.4c - was of the order of 0.009±0.001 and W_d was of the order of 17±3 MJ/m^3. Using those values in Eq. 1.10, results in a Ω/b of ≈ 308 MPa. This value is reasonable and comparable to the estimated flow stress of basal plane dislocations obtained from Fig. 3.8, viz. 500±100 MPa (see above). Note the purpose of these calculations is not to prove our IKB model, but rather to show that they are consistent with our other observations. They also suggest that the fully reversible nonlinear deformation is due to the to-and-fro motion of basal plane dislocations.

The fully reversible loops and the considerable energy dissipated during each cycle suggest that ZnO single-crystals behave like other KNE solids. From this work, however, it is also obvious that the KNE deformation of hexagonal crystals with c/a ratios near 1.5 depends on orientation. With increasing c/a ratios, the formation of IKBs becomes more ubiquitous and independent of orientation, as in the case of sapphire.[16] More single crystal work is needed to better understand the effect of orientation on the formation of IKBs when the c/a ratios are close to 1.5.

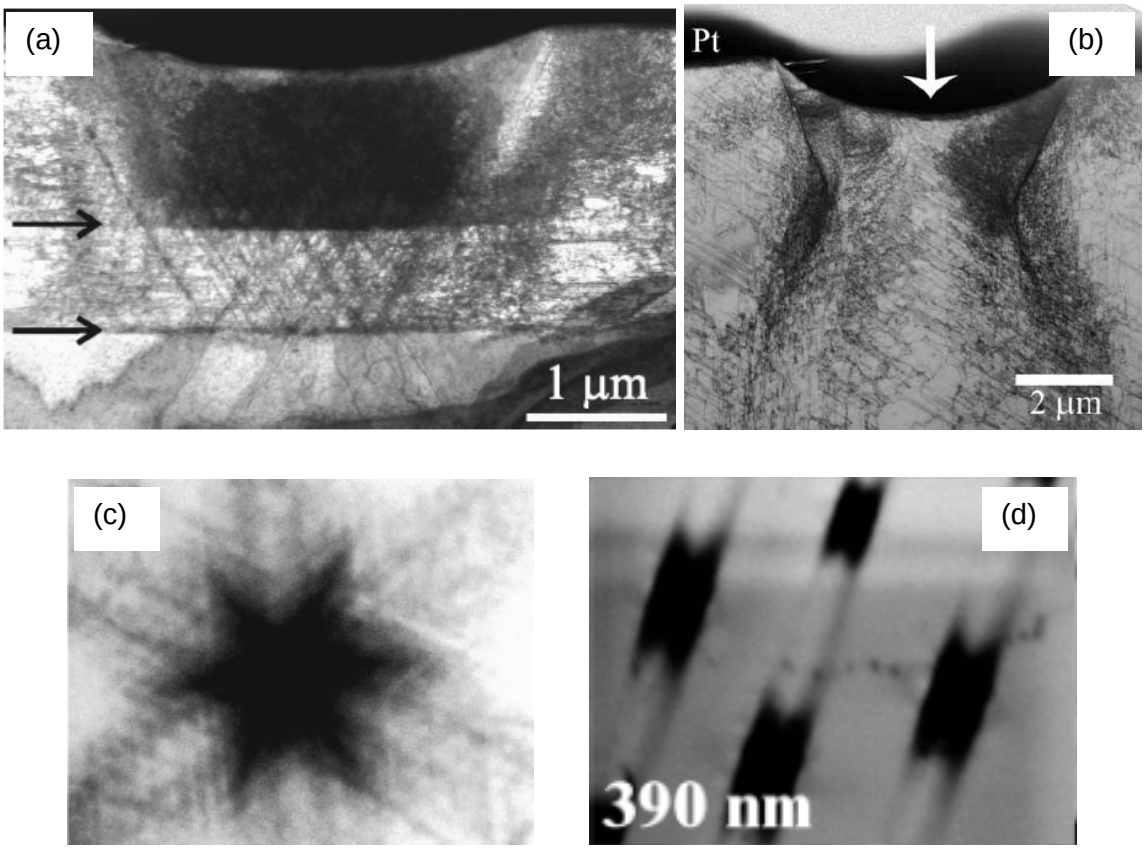

Fig. 3.13 a) Bright-field XTEM image of a spherical indent (tip radius ≈ 4.2 μm) in C-plane at a maximum load of 50 mN. Arrows denote slip bands along the basal planes. (taken from Ref. 53)[53] b) Bright-field XTEM image of a 50 mN spherical indent (tip radius ≈ 4.2 μm) in A-plane. The arrow shows the direction of indentation. (taken from Ref. 61)[61] c) Room temperature monochromatic CL image of a 200 mN spherical indent in C-plane. The field width for the image is ~ 65 μm and the CL wavelength is 376 nm. (taken from Ref. 53)[53] d) Room temperature monochromatic CL image of 200 mN spherical indents in A-plane. The field width for the image is ~ 170 μm and the CL wavelength is 390 nm. (taken from Ref. 61)[61]

Using the totality of our results and previous work[21,53,60-62] it is possible to reconstruct a highly simplified scenario of what happens at the atomic scale. When C-plane indentations were imaged in a SEM, a clear 6-fold pattern was observed (Fig. 3.5). When this information is combined with the XTEM (Fig. 3.13a) and cathodoluminescence (CL – Fig. 3.13c) observations of Bradby et al.[53] we conclude that in this direction pyramidal slip is also activated along with basal slip. Evidence for the activation of the former is clearly seen in the hardening rates for the C-plane *after* the pop-ins; they are clearly higher for the C-plane than the A-plane - compare the slopes of parallel dashed lines in Fig. 3.8 with the slope of the line XY - where presumably little pyramidal slip is observed.[61]

Consistent with the XTEM (Fig. 3.13b) and CL (Fig. 3.13d) observations of Coleman et. al.[61], when the A-plane indentations were imaged only one set of parallel slip lines, presumably due to basal slip, was observed (Fig. 3.10).

The different nature of dislocation structures in C and A orientations of ZnO were also verified by executing novel constant-stress indentation creep tests on both the surfaces. While – due to the inherent reversible nature of IKBs – the C orientation shows high resistance to creep, the A orientation exhibits creep because of dislocation pile-ups on basal planes. The details of this novel creep experiment are described in Ch. 4.

Combining these insights, with the fact that ZnO - in the C-direction at least - is a KNE solid allows us to propose the following scenarios for what is occurring at the atomic level. At pop-in, in the case of the C-plane, like in Ti_3SiC_2,[63,64] kink boundaries of opposite polarity are nucleated on either side of the indentation. The kink boundaries

under the indenter are of the same sign and merge together to form a high angle kink boundary right below the indenter. The ones at the edges are mobile, and what we termed mobile dislocation walls,[64] and are swept away along the $[11\bar{2}0]$ directions (Fig. 3.14b). This explains both the pile-up around the indentation mark and the formation of the Star of David with dimensions that are roughly twice as large as a (Fig. 3.14a). Note that these kink boundaries could not occur without concomitant delaminations and/or the formation of dislocation pileups or arrays – shown as near horizontal lines in Fig. 3.14a - along the basal planes, viz. parallel to the surface. Later in the process pyramidal slip bands at 60° to the surface are activated. With increasing stress, more basal slip bands are formed deeper into the material nucleating more pyramidal slip, etc., as observed.[53]

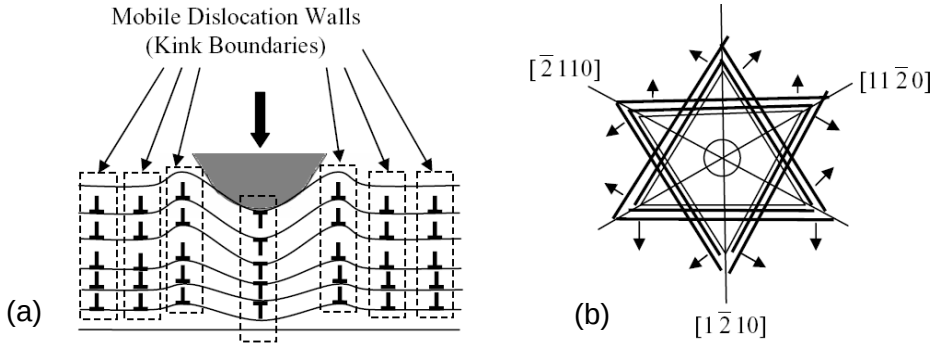

Fig. 3.14. a) Schematic showing formation of dislocation based kink bands and/or mobile dislocation walls during spherical indentation of the C-orientation. The horizontal lines represent basal plane dislocation arrays/pileups. b) Schematic of dislocation movement on basal plane to form the Star of David, as observed by Bradby et. al. (Ref. 53)[53].

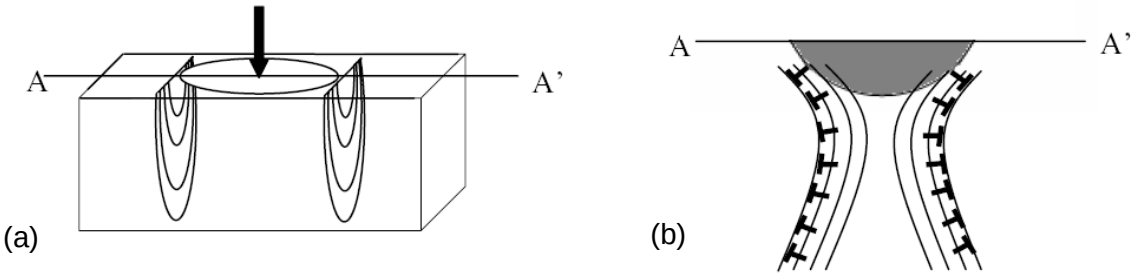

Fig. 3.15. a) Schematic of creation of basal plane dislocation loops when the A-surface is indented. b) Schematic of the cross-sectional view (along the line AA' in a), as confirmed from the XTEM study of Coleman et. al. (Ref. 61)[61].

In the case of the A-planes the situation is different; at pop-in basal dislocations of opposite signs are nucleated from the surface (Fig. 3.15a), on either side of the indentation mark (Figs. 3.15a and b). The presence of dislocations of one sign in turn results in a bending of the shear bands to form the hour-glass shape (Fig. 3.15b) clearly seen in the XTEM studies of Coleman et. al. (Fig. 3.13b).[61] This scenario explains the presence of the parallel slip lines observed in the SEM (Fig. 3.10), as well as high amount of creep during constant-stress indentation experiments (Ch. 4).

3.5 Conclusions

By converting load-depth of penetration curves to stress-strain curves, together with post indentation SEM observations and previous TEM work,[53,61] we conclude that:

a) In agreement with previous work,[61] we conclude that the factor of ≈ 2 difference in the hardness values of the C- and A-surfaces of ZnO is most probably due to the orientation of the basal planes with respect to the indentation axis.

b) The higher hardening rates of the C-plane are due to the nucleation of pyramidal dislocations, in addition to basal dislocations.

c) During the pop-ins, the strain energy is converted to the nucleation and movement of a large number of dislocations. The strain energy, released when the pop-ins occur, determines their extent.

As far as we are aware this is the first example of how indentation stress-strain curves can be used to shed important light on the atomistics of the deformation processes in ZnO single crystals, that would be otherwise very difficult, if not impossible, to obtain.

CHAPTER 4: ROOM TEMPERATURE CONSTANT-STRESS CREEP IN ZnO

4.1 Introduction

With recent advancements in micro/nano-scale devices, such as micro/nano electromechanical systems (MEMS/NEMS), dimensions are shrinking and stresses, thermal and other, can become significant. It follows that understanding the time dependent deformation, around room temperature, becomes crucial in predicting the failure modes and/or lifetimes of such devices. Currently, there are no satisfactory techniques by which such information can be rapidly and easily gathered and quantified, especially at the micro, or nano-scales. The problem is most acute for brittle solids; the latter is important since most MEMS/NEMS devices are typically made with brittle solids such as Si.

Studying room temperature plastic deformation in brittle solids and thin films has been an important topic of research. One of the most common, and popular techniques, has been depth-sensing nanoindentation (NI).[2,3,5] And while there were some attempts to use spherical indenters, over the last two decades, the vast majority of NI studies have been carried out using sharp Berkovich indenters.[2,4] Recently we developed a technique to convert *spherical* NI load/displacement results to NI stress-strain curves[24] and successfully applied it to solids with vastly different elastic moduli and elasto-plastic properties, such as single crystals of sapphire,[16] ZnO,[17] GaN,[48] $LiNbO_3$,[18] and

polycrystals of Al, Fe and others.[24] It is this breakthrough that, in turn, led us to the one described herein.

It has long been appreciated that because of the high stresses during indentation experiments, many materials will exhibit time dependent deformation, or creep, even at room temperature.[51,65,66] All of the studies to date, however, have been saddled with two problems. The first is not knowing the magnitude of the stresses under the indenter, especially when Berkovich tips are used. The second, related problem, is that microhardness and/or NI-based creep experiments are typically carried out at constant loads. Under those circumstances, the deformation of the material under the indenter results in a continual decrease of the stress with time, which in turn renders data analysis – at a more than qualitative level –difficult, if not, impossible. With the exception of a study carried out by Mayo and Nix[67] on Pb, Sn and their alloys, in which they maintained a constant loading rate, over a time period of 20 s, as far as we are aware, there are *no* reports of *constant-stress* NI *creep* tests in crystalline solids.

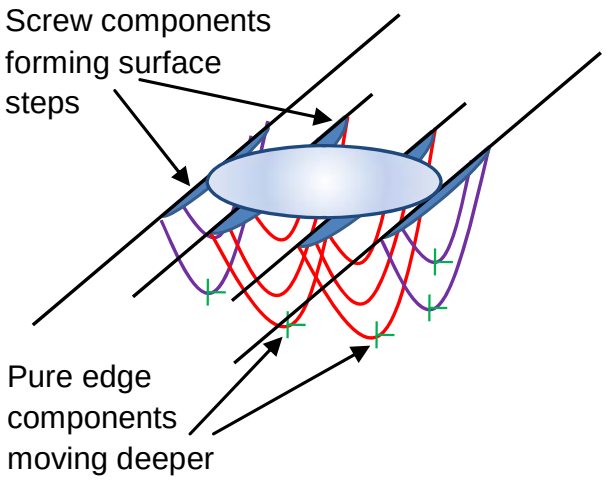

Fig. 4.1. Schematic of basal dislocation loops under the indented ZnO $(11\bar{2}0)$ surface.

In general, steady state creep is represented by the following power-law relationship.[68]

$$\dot{\varepsilon} = K\sigma^n , \tag{4.1}$$

where $\dot{\varepsilon}$ is the steady-state strain rate, K is a temperature dependent constant, σ is the applied stress, and *n* is the stress-exponent. Whether this relationship also applies under a NI has to date *not* been established. Since our recently developed method[24] allows us to calculate the stress under a spherical NI in *real time* we were able - using proportional-integral-derivative (PID) control - to keep it constant over relatively long (~ 4000 s) time periods. As shown here, this method also allowed us to test the validity of Eq. 4.1 at the submicron-scale.

The II-VI semiconductor, ZnO, has been selected for this study because of its technological importance in nonlinear electrical devices.[69] In the recent past, ZnO single crystals have gained popularity in applications such as short-wavelength optoelectronic devices and transparent transistors, because of their simpler crystal growth technology and better etching characteristics, as compared to GaN.[21,57] It is thus important to understand the mechanical behavior of ZnO single crystals, not only for better understanding of the underlying mechanisms, but also for better manufacturing and mechanical stability of devices based on this oxide.

Despite its increasing importance, until recently, little was available about the contact induced mechanical deformation in single crystal ZnO. Recently, using a combination of spherical NI, and cross-sectional transmission electron microscopy

(XTEM), Coleman et al.[60-62] showed that the deformation under the indenter was due to extensive slip on basal planes when indented in the $[11\bar{2}0]$, or, A direction, with loads higher than pop-in loads. They also reported a lower hardness as compared to the [0001], or, C direction, where the deformation was reported to be due to slip on both basal and pyramidal planes.[21,53] More recently, we concluded that when indented in the A-direction, the deformation was accommodated by the formation of dislocation pile-ups (DPs – Fig. 4.1) on basal planes underneath the indenter.[17] This observation, together with the fact that *no* cracks - that could clearly complicate the analysis - are observed around the indenter at any load, led to this work.[17]

4.2 Experimental Details

High quality ZnO single crystal was purchased (Wafer World, West Palm Beach, FL) with $(11\bar{2}0)$ orientation (A-plane). The NI experiments were performed at room temperature, with a nanoindenter (XP system, MTS Corp, TN) equipped with a continuous stiffness measurement (CSM) attachment. A diamond hemispherical indenter with nominal tip radius of 5 μm, calibrated on fused silica, was used. The details of the indentation load-displacement data to indentation stress-strain conversion procedure can be found in Ch. 2.[24]

As mentioned earlier, the NI creep experiments were carried out during the second loading cycle. Thus, each location on the sample surface was first preloaded up to 40 mN, unloaded to 4 mN, and then reloaded to a different load (33 mN, 35 mN, or 38 mN, etc.) at which point the PID control took over to maintain the indentation stress at a constant value. The PID parameters, used to control the stress, are as follows:

proportional gain, $k_P = 2$, integral gain, $k_I = 1$, derivative gain, $k_D = 1$, maximum speed = 10 mN/s and minimum speed = 0 mN/s. Two sets of experiments were carried out with holding segments of 400 s and 4000 s.

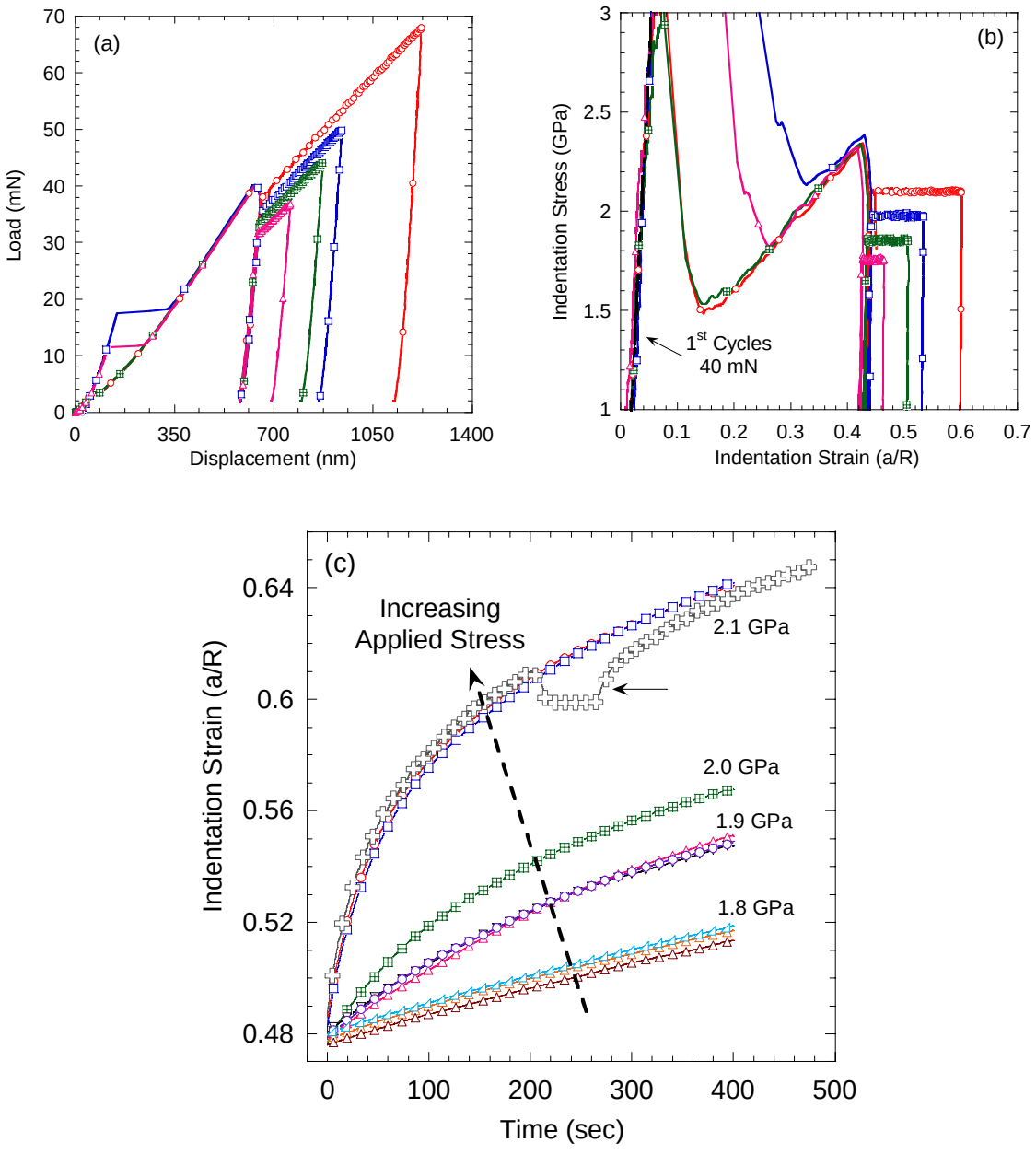

Fig. 4.2. a) Typical load-displacement response when a ZnO $(11\bar{2}0)$ surface is indented with the 5 μm spherical tip. To keep the stress constant during the second cycle, the load had to be continually increased. b) Corresponding NI stress-strain curves. Note the constant nature of applied stress during the creep tests. c) Time dependence of NI strain at stresses shown. Horizontal arrow points to a run that was interrupted for 50 s, 200 s into the creep run. No evidence for backpressure was noted.

Experimentally one of the difficulties in carrying out long term NI tests is thermal drift. In order to minimize its effect, all tests were begun only when the maximum allowable drift was < 0.05 nm/s. In other words, the results were considered for creep calculation, only when the increase in displacement during the holding period was higher than 20 nm over 400 s, or 200 nm over 4000 s.

4.3 Results and Discussion

The load-displacement curves into a $(11\bar{2}0)$ ZnO surface are shown in Fig. 4.2a. As noted above, due to the stochastic nature of the elastic-to-plastic transition, or pop-in stresses (Fig. 4.2a),[17,22] the first cycle was not used. Instead, the creep measurements were carried out during the *second* cycle into the same location (Fig. 4.2a). The corresponding NI stress-strain curves, in 4 different locations and stresses, are shown in Fig. 4.2b. In each location, at a strain > ≈ 0.43, the stress was held constant. The resulting NI strain, ε, - defined here, as previously,[24] as *a/R* where *a* is the contact radius, and *R* is the indenter radius – versus time, t, plots clearly show that ε increases with t (Fig. 4.2c). Note that in order to keep the stress constant, the loads had to increase with displacement more or less linearly (Fig. 4.2a).

When log-log curves of σ versus $\dot{\varepsilon}$ (Fig. 4.3a) – where $\dot{\varepsilon}$ was determined from the slopes of the strain-time curves (Fig. 4.2c) - were plotted, they did not follow Eq. 4.1, i.e. the slopes, or n_{app}, defined as:

$$n_{app} = \frac{\partial \ln \dot{\varepsilon}}{\partial \ln \sigma} \tag{4.2}$$

were not constant, but decreased with time, t.

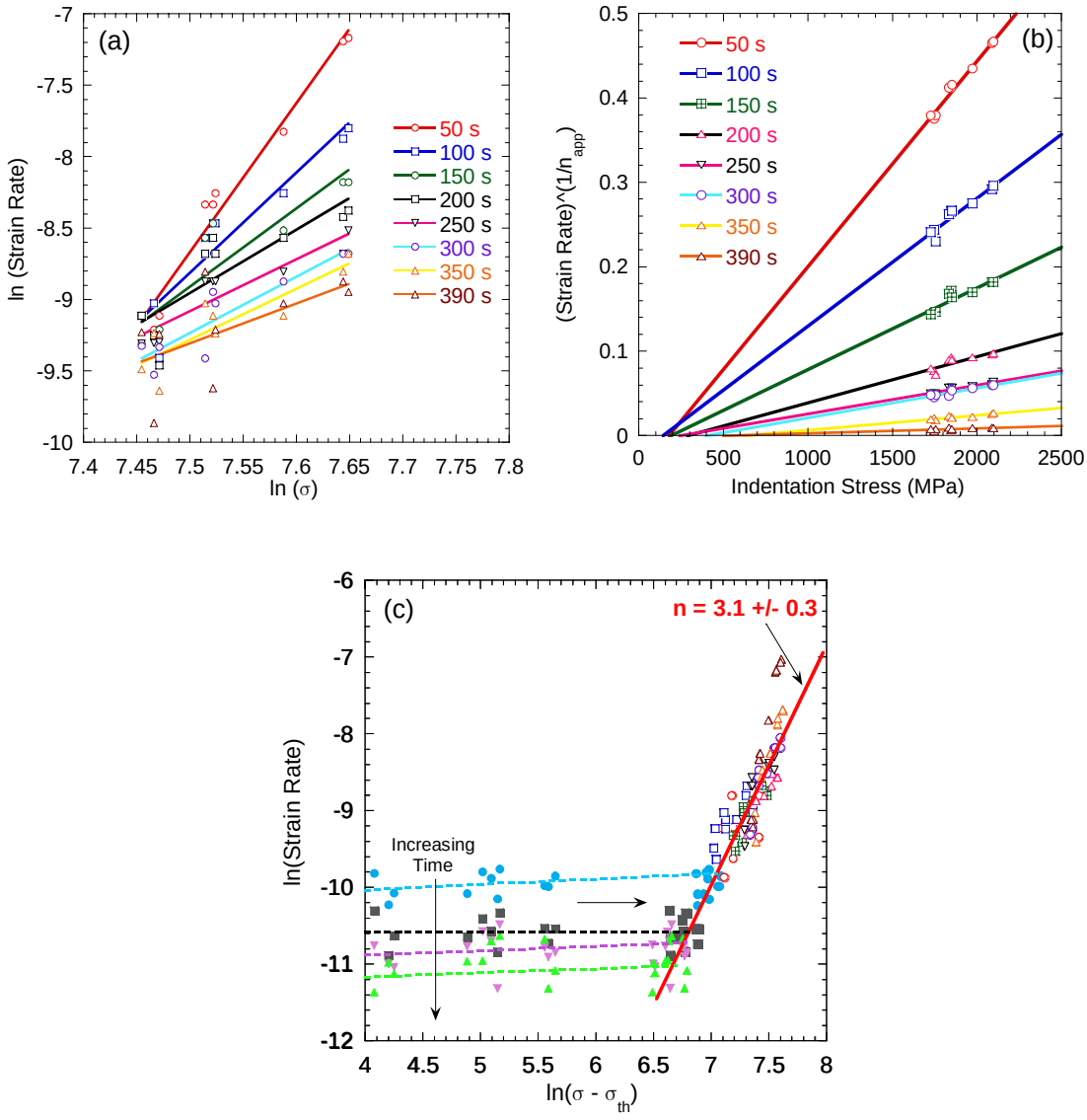

Fig. 4.3. a) The log-log plot of strain rate vs. applied stress from the data obtained at different times during the 400 s holding segment. Note the decrease in slope with increasing time. b) Corresponding variation of strain rate with indentation stress at different times during the 400 s holding period. The intercept on the x-axis represents the threshold stress at a particular time. c) Log-log plot of strain rate, $\dot{\varepsilon}$, vs. effective stress, $\sigma - \sigma_{th}$, where σ_{th} is a threshold stress. Hollow symbols represent the data up to 400 s, where σ_{th} is estimated from (b). Solid symbols represent the creep data up to 4000 s. To determine σ_{th}, it was varied until the solid data points they fell on the n = 3.1±0.3 line. i.e. σ_{th} was an adjustable parameter.

This behavior suggests a threshold-type creep deformation for which:[70,71]

$$\dot{\varepsilon} = K(\sigma - \sigma_{th})^n, \tag{4.3}$$

where σ_{th} is a threshold stress, which is also time dependent. To obtain σ_{th} at each t, we plotted $\dot{\varepsilon}^{\frac{1}{n_{app}}}$ vs. σ (Fig. 4.3b).

According to Eq. 4.3, σ_{th} at each t is simply the x-axis intercept. Once the threshold stresses were determined, $\ln\dot{\varepsilon}$ was plotted vs. $\ln(\sigma - \sigma_{th})$ (hollow symbols in Fig. 4.3c), which resulted in a straight line, with a slope of 3.1±0.3. It is thus reasonable to conclude, and despite some scatter, that Eq. 4.3, governs the creep of ZnO when loaded in the $[11\bar{2}0]$ direction under a spherical NI, with n ≈ 3, which is not incompatible with a dislocation glide mechanism along a limited number of slip systems, i.e. < 5.[72]

To understand the creep response at longer times, another set of experiments was carried out with a holding period of 4000 s. Here again $\dot{\varepsilon}$ was measured at different times (1000 s, 2000 s, 3000 s, etc.). However, because of increasing values of σ_{th}, the strain rates dropped significantly and, could no longer be determined accurately from plots such as those shown in the Fig. 4.3b. Instead we first assumed a σ_{th} of 1.7 GPa – which was the lowest applied stress - and plotted the results on Fig. 4.3c as solid symbols on lower right hand-side of the plot. If one then makes the reasonable assumption that the dominant creep mechanism does not change by extending the creep time from 400 to 4000 s, then the creep behavior should follow the same line with a slope ~ 3, that describes the short-term creep tests (i.e. hollow symbols in Fig. 4.3c). This can be done by varying σ_{th} until the solid symbols fell on the inclined solid line with the slope of ~ 3.

Said otherwise, for the 4000 s results, σ_{th} was treated as an adjustable parameter. Note that a different σ_{th} is determined at every t.

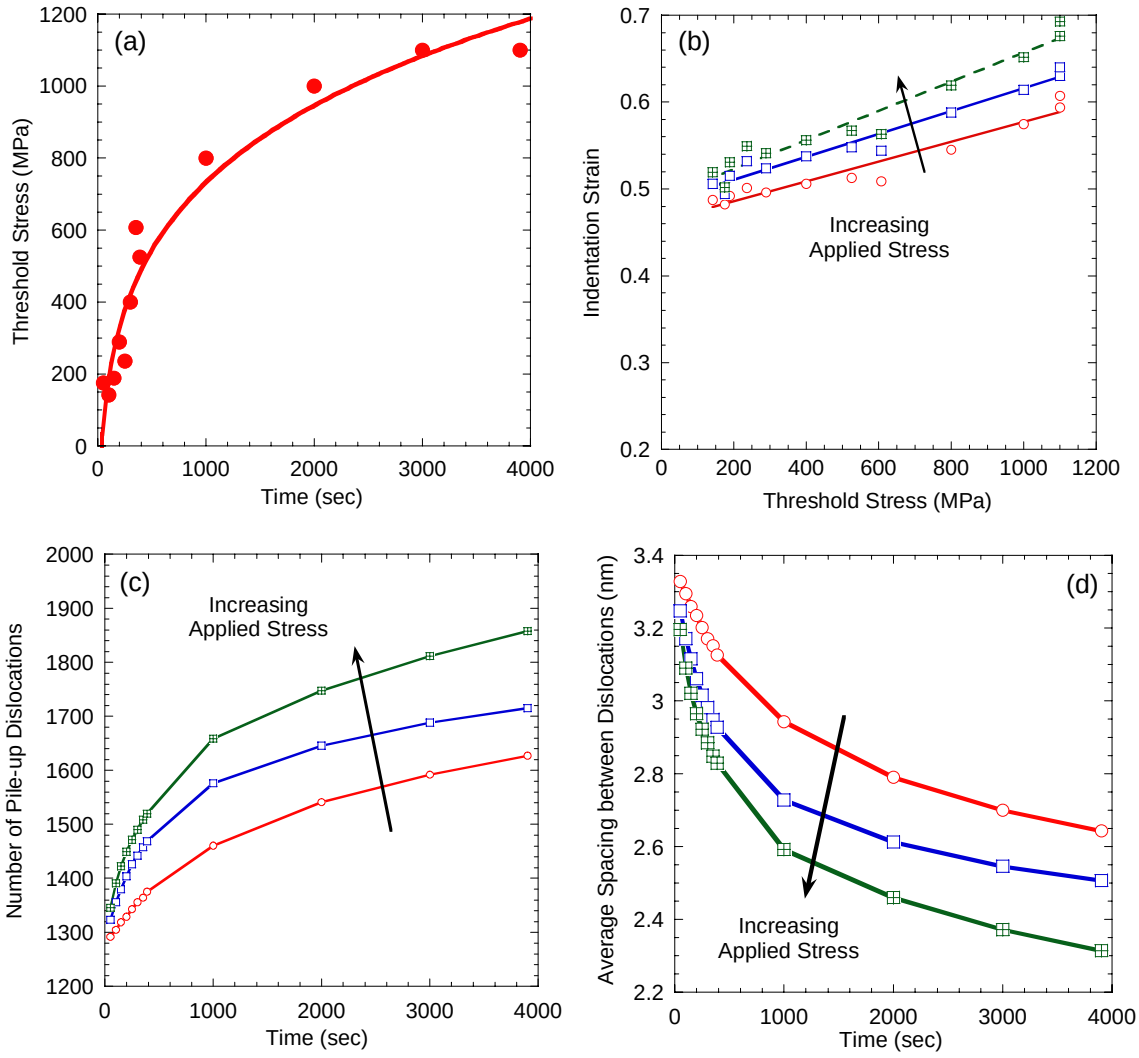

Fig. 4.4. a) Time dependence of σ_{th}; b) Functional dependence of NI strain with σ_{th} and applied stress, σ; c) Time and σ dependence of number of pile-up dislocations; and d) time and σ dependence of average distance between pile-up dislocations.

When the resulting variations in σ_{th} with t were plotted, the best fit (solid line in Fig. 4.4a) was one where σ_{th} scaled with log t. The fact that the same fit can be used to describe the changes in $\dot{\varepsilon}$ with t (Fig. 4.2c) is gratifying and indirectly validates our

methodology. The same time dependencies, in turn, lead to the linear relationship between ε and σ_{th} shown in Fig. 4.4b.

Based on these results we propose the following micromechanism to explain the observed creep response. During the first cycle, and as a direct result of the pop-ins, basal plane dislocation pileups (Fig. 4.1) are created.[17] To render further analysis possible, we make the assumption that the number of pile-up dislocations, increase with time, resulting in the creep observed. The XTEM work[20] also showed that the lengths of the pileups, L, is of the order of 2*a,* which is estimated to be ≈ 4.3±0.1 μm after the pop-ins.

If this picture is accurate, and assuming that the threshold shear stress, $\tau_{th} \approx \frac{\sigma_{th}}{2}$, then the number of DPs per unit volume, N_s, can be estimated from the slopes in Fig. 4.4b, assuming,[46]

$$N_S = \frac{2G}{\pi(1-\nu)L^3}\frac{d\varepsilon}{d\sigma_t}\ , \tag{4.4}$$

where *G* is the shear modulus - assumed to be equal to c_{44} or 45.1 GPa;[57] ν, is Poisson's ratio (0.2). Using these values N_s is of the order of $6\pm1\text{x}10^{16}$ m^{-3}.

Once N_S is known, the number of dislocations in a pileup, n_d, can be estimated assuming,[46]

$$n_d = \frac{\varepsilon}{N_S L^2 b}, \tag{4.5}$$

where b is the Burgers vector (0.324 nm). Equation 4.5 implicitly assumes that the increase in strain is accommodated by the formation of new dislocations. Consequently, the average spacing between dislocations becomes,

$$x_d = \frac{L}{n_d} \tag{4.6}$$

The dependencies of n_d on t and stress are shown in Fig. 4.4c; the corresponding dependencies of x_d on t and stress are shown in Fig. 4.4d. Under those conditions, dislocation density, ρ, which can be estimated from,

$$\rho = 3LnN_S \tag{4.7}$$

is ≈ 10^{11} cm^{-2}, which is quite reasonable considering the highly localized deformation and the high stresses under the NI.

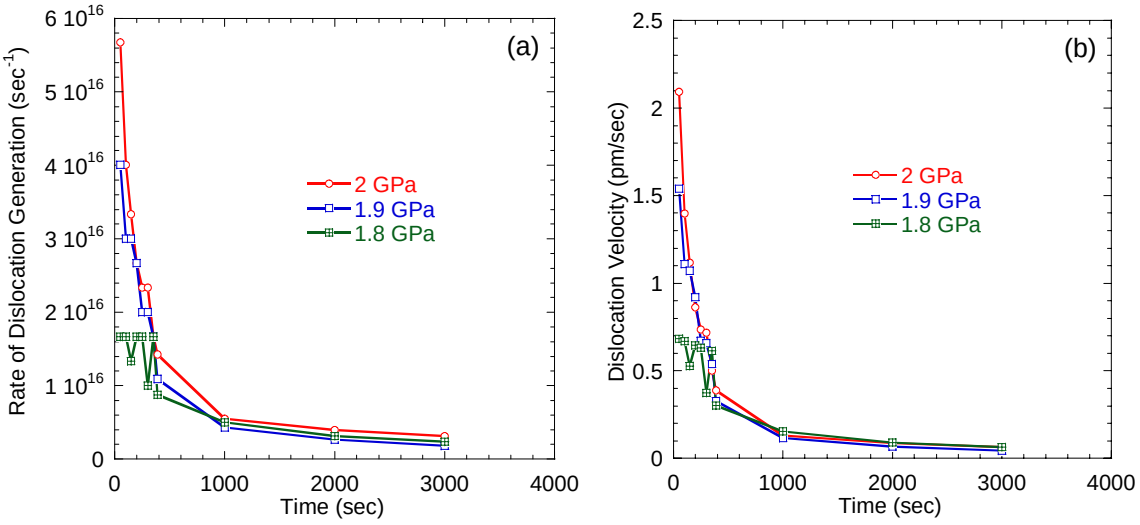

Fig. 4.5 Time dependent variation in - a) rate of dislocation generation; and b) Dislocation velocity.

Estimated dislocation dynamics - i.e. the rates of dislocation generation and movement as a function of time (i.e. σ_{th}) - at different applied stresses (Figs. 4.5a and b, respectively) were obtained by differentiating the curves shown in Figs. 4.4c and d, respectively. Similar time dependence at different applied stresses (Fig. 4.5), most presumably, indicates that both the rate of dislocation generation and dislocation velocity are governed primarily by σ_{th}.

These calculations notwithstanding, it is hereby recommended that the values of n_d, x_d, dislocation nucleation rate and dislocation velocity calculated be taken with a modicum of skepticism because of the complicated, non-uniform, stress-state under the indenter, the definition of strain used, as well as the simplifying assumptions for which Eqs. 4.4 to 4.7 are valid. However, while the actual numbers may vary, we believe our approach captures the fundamental physics of what is occurring under the indenter.

In order to probe whether the dislocation pileups had any back stresses, a number of interrupted runs - one of which is shown by a horizontal arrow in Fig. 4.2c - in which the load on the indenter was removed for 50 s, and reloaded, to the same stress. No evidence of negative creep was observed suggesting that these pileups had no measureable back-pressure.

In conclusion, a constant-stress spherical NI method was used to study room-temperature indentation creep in $(11\bar{2}0)$ ZnO single crystal. Consistent with our previous conclusions concerning dislocation distributions under a spherical NI, we find that the room-temperature creep in ZnO can be attributed to DPs.

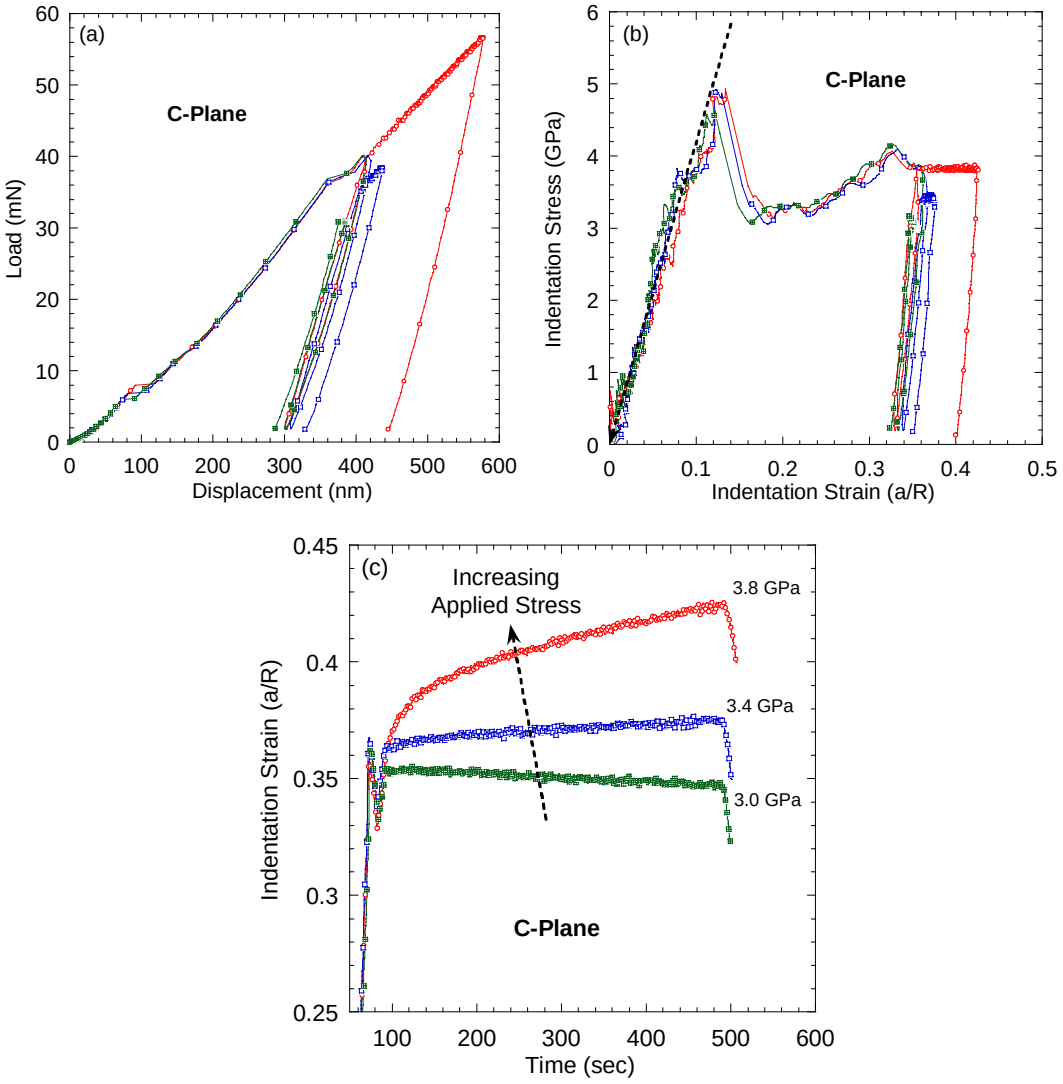

Fig. 4.6 a) Typical load-displacement response when a ZnO (0001) surface is indented with the 5 µm spherical tip. To keep the stress constant during the second cycle, the load had to be continually increased. b) Corresponding NI stress-strain curves. c) Time dependence of NI strain at stresses shown. Note the strain rates are significantly lower compared to the A-plane (Fig. 4.2c).

When similar experiments were carried out on the (0001) orientation (Fig. 4.6), the load-displacement and indentation stress-strain curves showed similar behavior. But the strain rates observed – even at little higher stresses – were roughly an order of magnitude smaller than those for $(11\bar{2}0)$ orientation, which is consistent with our conjecture that in the (0001) orientation, the formation of domain walls and/or kink boundaries, along with

pyramidal slip, act as hurdles for the dislocations.[17] This comment notwithstanding, more work is needed to understand time-dependent deformation in materials at micro/nano-scale.

The ramifications of this work go beyond understanding the creep response of ZnO single crystals for several reasons. First, understanding the micro/nano-scale time dependent deformation at high stresses and low temperatures, which in turn can be compared to more conventional macro-scale creep experiments, is crucial in bridging the gap between different lengths scales during creep. Currently the link between the micro and macro-scales has *not* been established, and therefore there is no paradigm, or framework, for even thinking about the problem; the equations to use are simply *unknown*. Needless to add, without that knowledge the design of devices, where long-term mechanical stability is an important consideration, cannot be carried out.

Second, the *real-time* calculation and control of stress during NI experiments opens the door to understanding other stress/time dependent phenomena, such as fatigue and subcritical crack growth. Here again the crucial link between the nano/micrometer and macro-scales - that currently does not exist - can be established, understood and modeled. It is important to note that, in most cases, large pop-ins lead to the emanation of cracks from the indents,[16,18,48] rendering this technique almost ideally suited to the study of subcritical crack growth. In that case, however, it is important to decouple creep from subcritical crack growth.

Third, the fact that we can now, rapidly and non-destructively, estimate the number of dislocations, their separations and dynamics is noteworthy. This kind of information

should help theoreticians and modelers in fine-tuning their dislocation-based models, as well as explore the effect of confining, or hydrostatic conditions, on dislocation dynamics. The work carried out herein was done with a 5 μm radius spherical indenter. In principle, there are no reasons why the tip radius cannot be reduced further to the point where one is truly probing the nano-scale, at which time, theoretical models and simulations can fully mimic what is occurring under the indenter. Said otherwise, when the volume probed is comprised of a few million atoms, they can all be simulated simultaneously.

In short this paper presents a powerful and new way of exploiting NI stress/strain curves to understand the time-dependent, deformation of materials, in general, and brittle solids in particular at the nano/micrometer scale. The same principle – real time feedback of the stress - can also be used to quantitatively study fatigue and subcritical crack growth at the same scales.

CHAPTER 5: KINKING NON-LINEAR ELASTIC BEHAVIOR IN $LiNbO_3$ SINGLE CRYSTALS

5.1 Introduction

Lithium niobate – $LiNbO_3$ – has attracted a good amount of attention because of its important nonlinear optical properties for applications in electro-optic, acousto-optic, and optical storage devices.[73] Precise knowledge of the mechanical deformation behavior is a prerequisite for successful manufacturing and operation of these devices. Despite the importance, very little is available on the elastic-plastic transition and dislocation movement during contact deformation in $LiNbO_3$.

Earlier studies on $LiNbO_3$ single crystals have been limited to mostly uniaxial compression[74] and Vickers microhardness.[75] When single crystals are loaded in uniaxial compression at temperatures > 1150 °C, $(10\bar{1}2)[\bar{1}011]$ twins form.[74] Within these twins, basal slip is observed. More recently, Park et al.[76,77] confirmed the existence of this twin system (Fig. 5.1). Subhadra et al.[75] reported a Vickers microhardness of ~ 6.3 GPa, at 2 N load, for a single crystal loaded along [0001] and showed that, with increasing load, the hardness dropped.

The phenomenon of fully reversible dislocation motion is not very widespread. Recently, there have been some reports of reversible plastic deformation in Au and Si, nanospheres.[78,79] For example, Gerberich et al.[79] presented evidence and proposed a

model for small reversible plastic deformation in Si nanospheres. The model – based on the backstress of dislocation pileups - successfully explained such strains during their contact loading experiments. More recent wok by the same group,[80] however, suggests that phase transitions may be the origin of these observations. Our work on indentation creep of ZnO also suggests the absence of such back stresses due to dislocation pileups (Ch. 4). Herein, we suggest that reversible dislocation motion – but not in the configuration of pileups – is responsible for the reversible strain measured in $LiNbO_3$ single crystals.

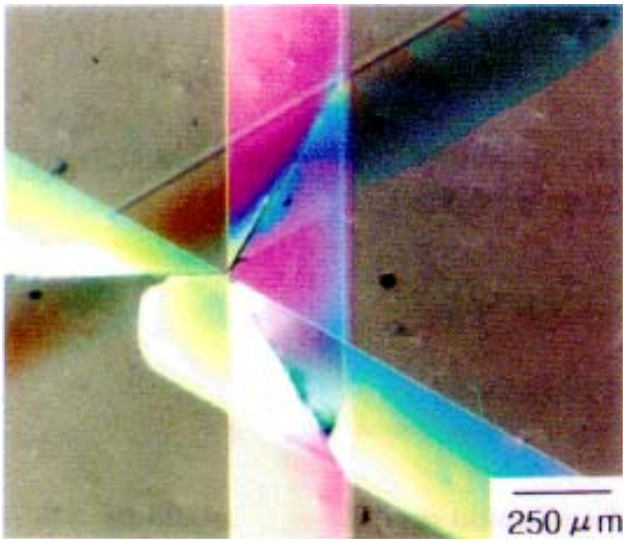

Fig. 5.1 A photograph of transmission polarizing microscope showing three sets of intersecting twin lamellae in $LiNbO_3$ single crystal (taken from Ref. 77).[77]

Recently it was postulated that most solids with c/a ratios > 1.5 belong to the same class of solids which were labeled kinking nonlinear elastic, KNE.[11,30,42] The signature of KNE solids is the formation of fully reversible, hysteretic stress-strain loops on repeat loadings.[11,31] This full reversibility is attributed to the formation of incipient kink bands, IKBs, that are comprised of multiple parallel dislocation loops (Fig. 1.1a) that either

annihilate or shrink when the load is removed.[31] In other words, solids that are highly plastically anisotropic, deform at least initially by the formation of dislocation-based IKBs. At higher stresses, as for example under a nanoindenter, the IKBs are sundered and devolve, first into mobile dislocation walls, MDW, and then ultimately into kink boundaries, KBs. The latter are irreversible.[11,16,17,23,48,63,64] Based on work by Frank and Stroh,[27] we developed a microscale model for this unique deformation behavior,[30] which is discussed in details in Ch. 1.

Recently, we have also shown that spherical nanoindentation can be a powerful tool to understand the deformation of single crystals under point contacts. This is especially true when the load-displacement data are converted to indentation stress, $\frac{P}{\pi a^2}$, and indentation strain, $\frac{a}{R}$.[3,11,16,17,20,24,81] where P, E*, a and R are the load, reduced modulus, contact and tip radii, respectively. The indentation stress-strain conversion procedure is discussed in Ch. 2. In this work, repeated nanoindentation - into the same location, with 3 different R's - was used to understand the response of $LiNbO_3$ single crystals indented along the [0001] and $[11\bar{2}0]$ axes.

5.2 Experimental Details

High quality, bulk, $LiNbO_3$, single crystals with (0001) and $(11\bar{2}0)$ orientations – denoted by C-plane and A-plane, respectively – orientation were purchased (MTI Corporation, Richmond, CA). The nanoindentation experiments were performed at room temperature in a nanoindenter (XP system, MTS Systems Corp, TN) with a continuous stiffness measurement (CSM) attachment. Three diamond sphero-conical indenters with

tip radii of 1, 5 and 13.5 μm were used. The loading rate/load ratio was held constant at 0.1. Post-indentation surface features were examined using a scanning electron microscope, SEM (XL30, FEI, Hillsboro, OR). We also measured the Vickers microhardness using a load of 2 N.

5.3 Results and Discussion

The repeated spherical nanoindentation behavior for all three different tip sizes were dependent on the orientation of the crystal (i.e. C and A). As discussed below the discrepancy is, most probably, due to different arrangement of twinned domains, and the arrangement of slip planes therein. Hence, we discuss the response of the C and A orientations separately.

5.3.1 C-Plane

The load-displacement results for the 13.5 μm indenter (Fig. 5.2a) clearly show that while the first cycle is open, the repeat cycles are closed, fully reversible and reproducible.[18] Note that true reproducibility is only achieved somewhere between cycles 5 and 10; cycles 10 to 30 are, within the resolution of our indenter, identical. Figures 5.2b and c show similar cyclic deformation behavior for 5 and 1 μm indenters, respectively. As discussed previously,[11,12,16,17,23,48] such a response can only be explained by invoking the formation and annihilation of dislocation loops.

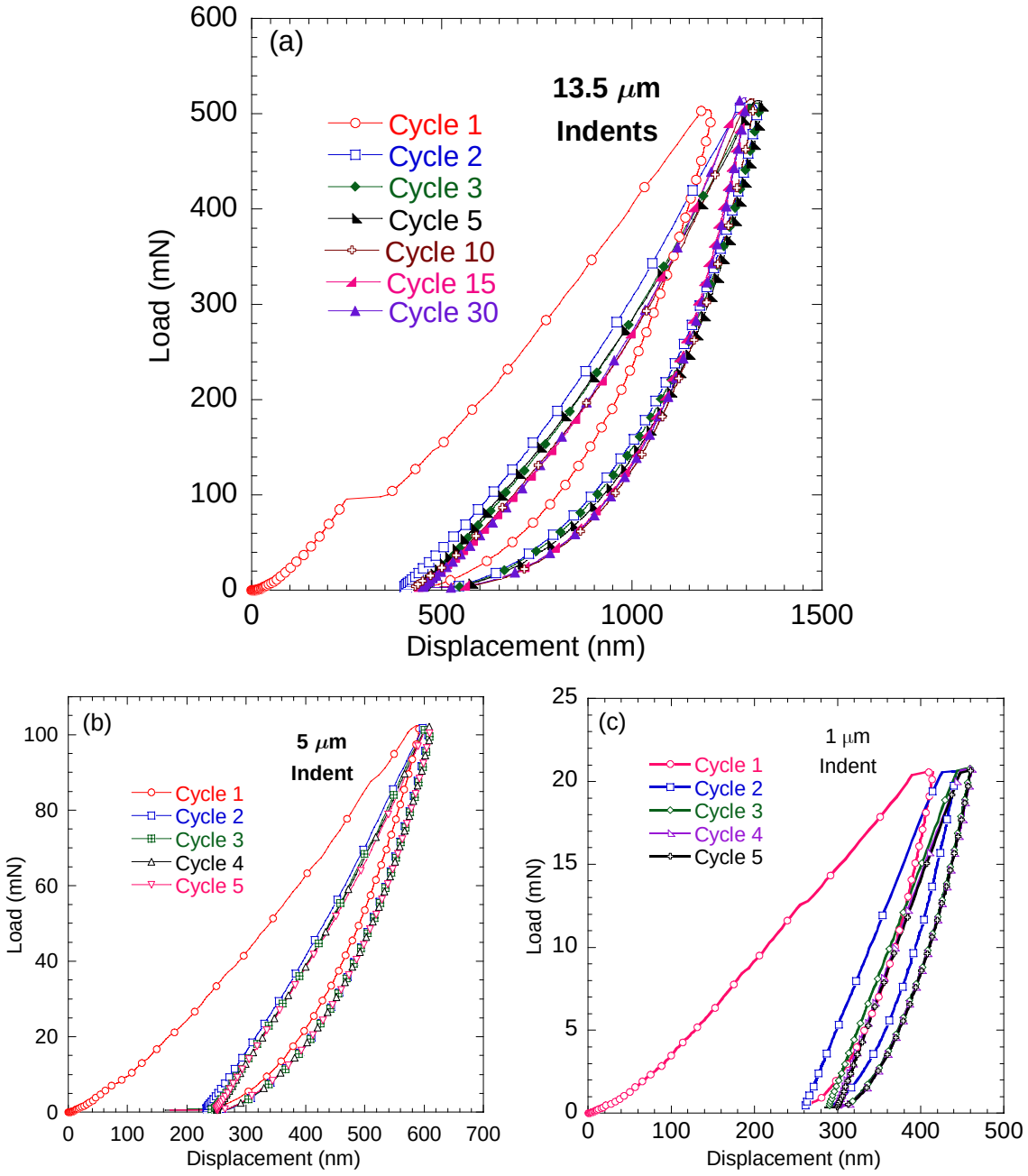

Fig. 5.2. Typical load-displacement results obtained when a C-plane $LiNbO_3$ single crystal was cyclically loaded using a spherical indenter with tip radius of; a) 13.5 μm; b) 5 μm; and c) 1 μm.

To study the reversible motion of dislocations according to our KNE model – discussed in Ch. 1 – the crystal was also indented up to different maximum loads during cyclic loading (Fig. 5.3).

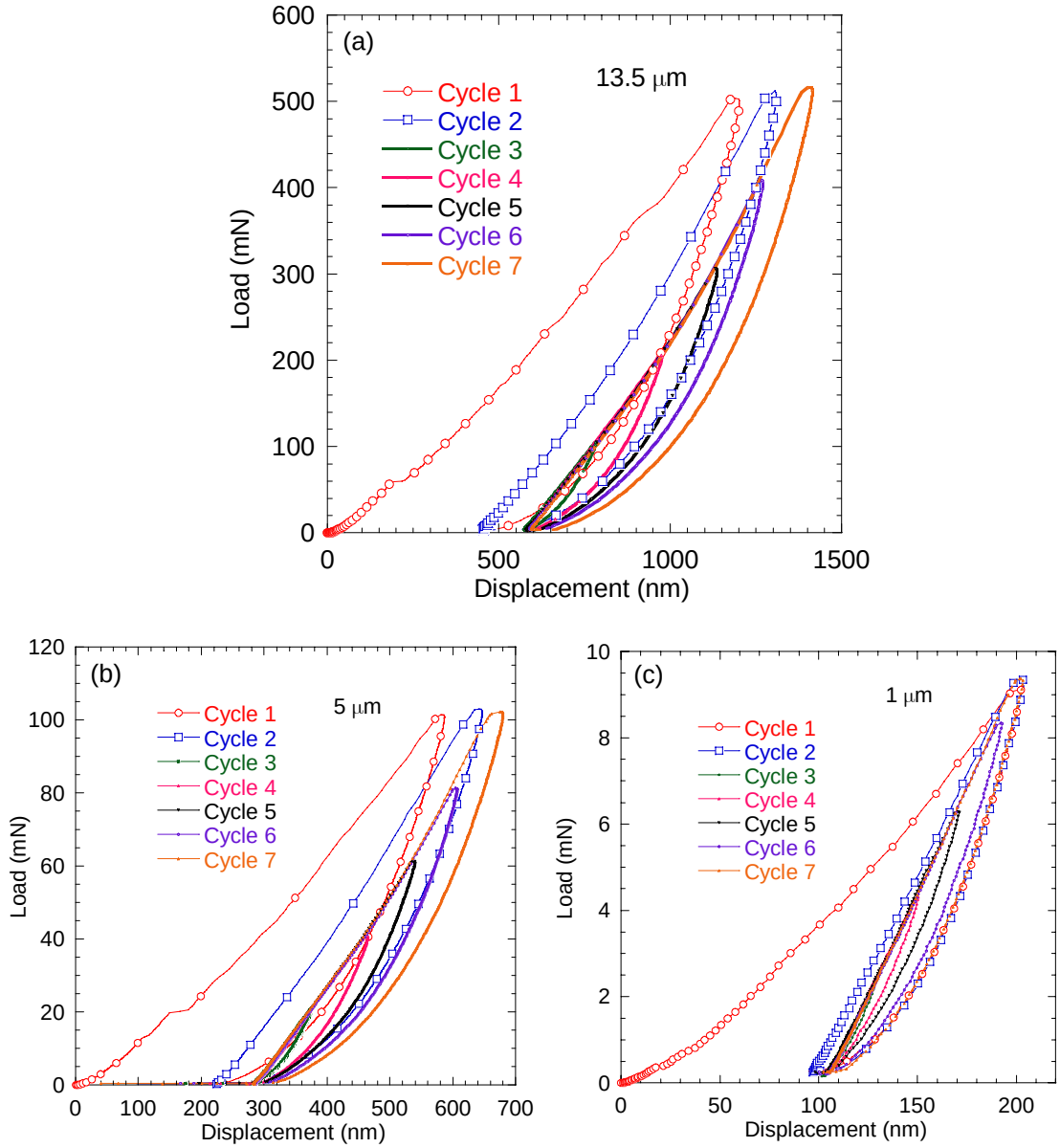

Fig. 5.3. Typical load-displacement results obtained when a C-plane $LiNbO_3$ single crystal was cyclically loaded up to progressively increased loads using a spherical indenter with tip radius of; a) 13.5 μm; b) 5 μm; and c) 1 μm.

When the contact stiffness was plotted against the calculated contact radii for three different tip sizes (Fig. 5.4), the curve was linear over the whole deformation range. The indentation modulus calculated from the slope was 186±2 GPa, which is in good agreement with the modulus measured from Berkovich nanoindentation on the same

surface (200±2 GPa) and the value of 1/s33 (199 GPa) calculated using the elastic constants for $LiNbO_3$.[82]

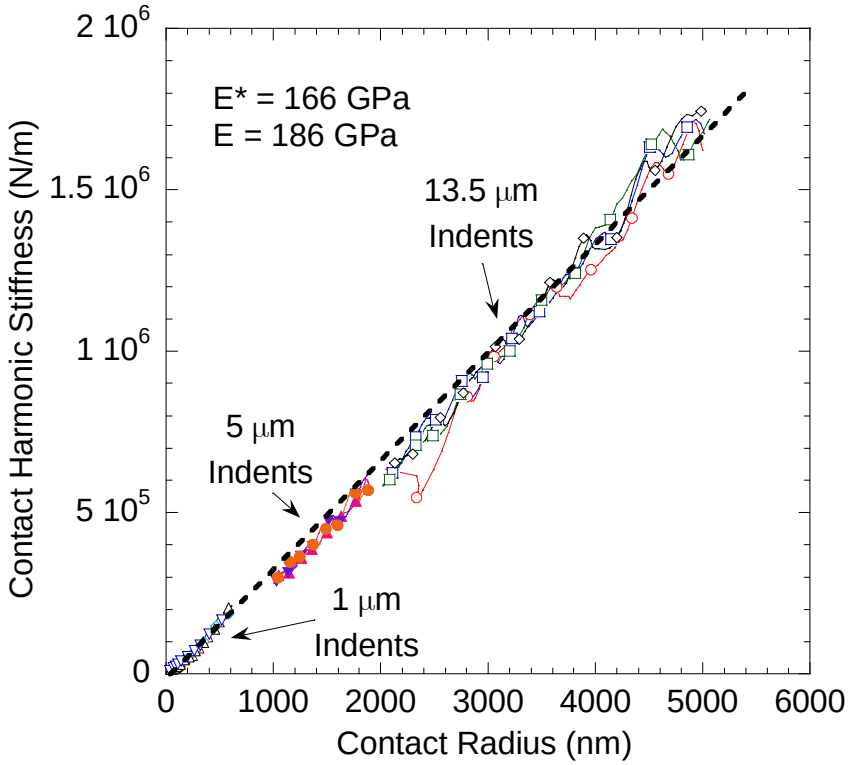

Fig. 5.4. Change in contact harmonic stiffness with contact radii for indentation on C-plane $LiNbO_3$ with 1, 5 and 13.5 μm spherical indenters. Note the excellent agreement in slope from three extremely different tip sizes.

The first cycle indentation stress-strain curves (Fig. 5.5a) - for the 3 tips explored herein - clearly show that, in both the linear elastic, and early on in the plastic regime, they are *not* a function of R, lending credence to our method of obtaining these type of curves.[24] Furthermore, at ≈ 4.5±0.2 GPa, the minima in the stress-strain curves are in excellent agreement with the Vickers microhardness value (dashed horizontal line) measured on the same sample. The hardness measured with Berkovich nanoindentation is also shown in Fig. 5.5a.

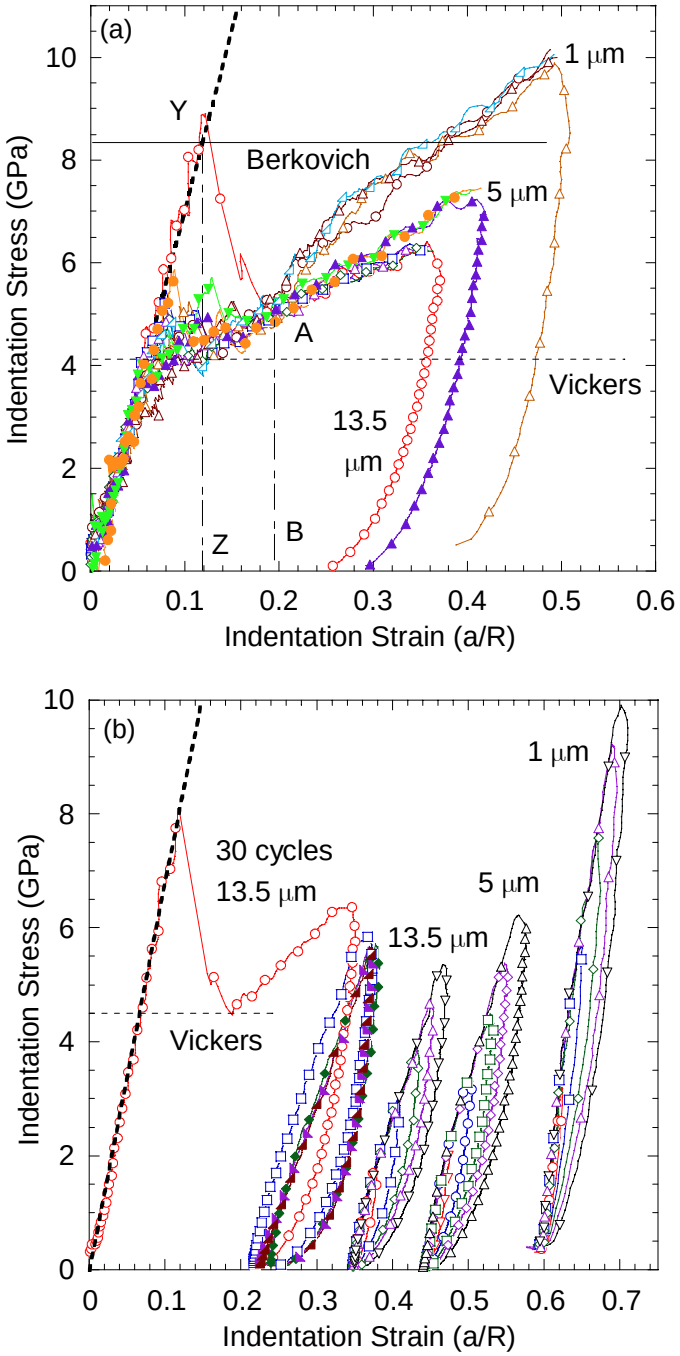

Fig. 5.5. a) Indentation stress-strain curves of the first cycle for results shown in Fig. 5.2. Dashed and solid horizontal lines represent the Vickers microhardness and the hardness measured by Berkovich nanoindentation, respectively. The dashed inclined line represents the elastic modulus, measured from S vs. a curves. b) Indentation stress-strain response for cyclic loading. The curves on the left are for the results shown in Fig. 5.2a. Center loops, and those on the right, were obtained after a location was indented to the highest load (500 mN for 13.5 μm, 100 mN for 5 μm, and 9 mN for 1 μm indents) for 2 cycles, unloaded and progressively loaded to higher stresses (Fig. 5.3). The nested loops, with one loading trajectory, were shifted from their original position to the right for clarity.

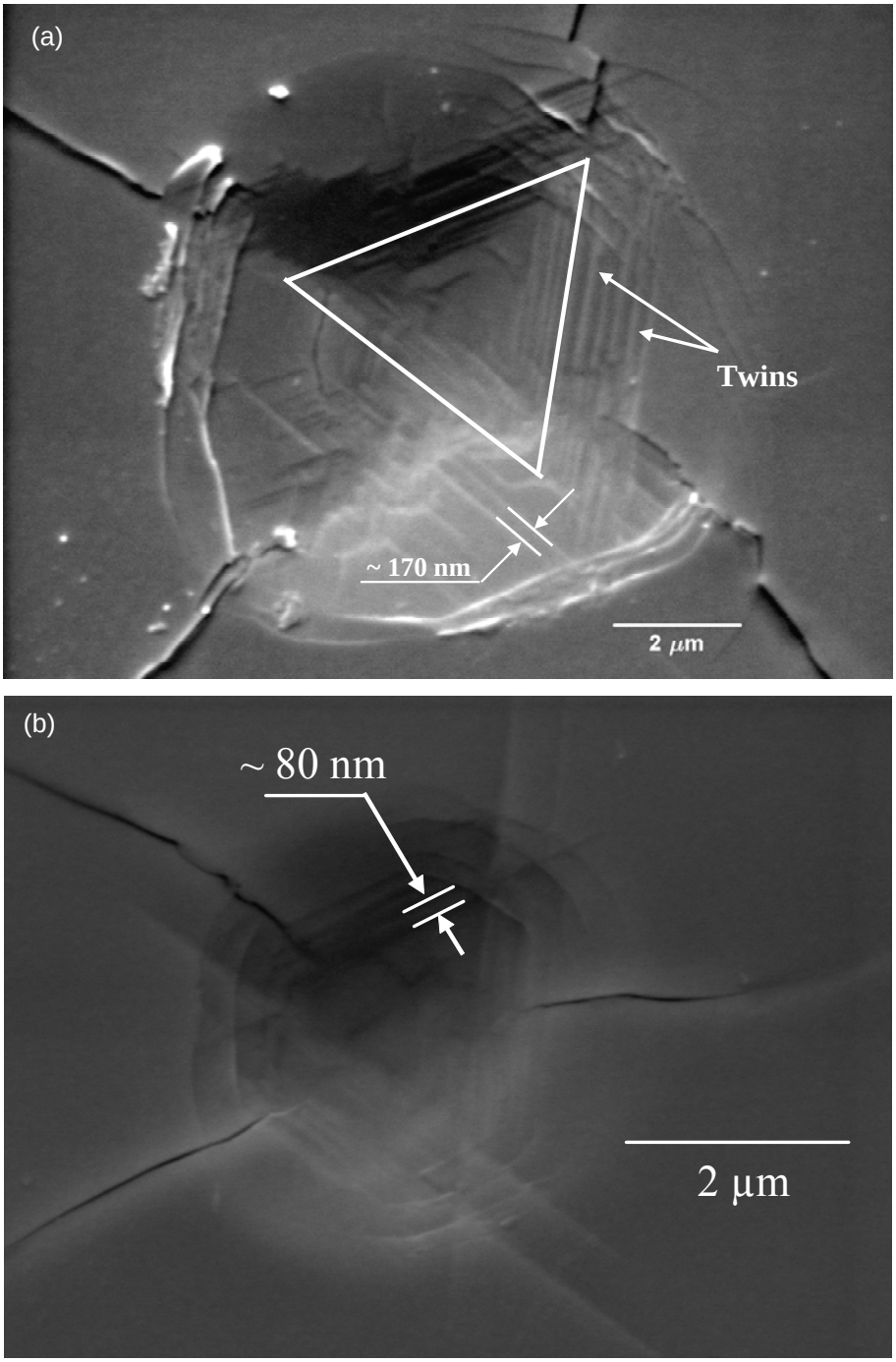

Fig. 5.6. SEM image of indentation mark made with the a) 13.5 μm tip loaded to 500 mN; and b) 5 μm tip loaded to 100 mN. Note 3-fold symmetry of the linear surface features.

The repeat loops shown in the center, and on the right in Fig. 5.5b, were obtained by loading a given indenter twice to the maximum load, unloading and then reloading to

progressively higher loads to generate the nested loops observed. Note that in all cases, as for all other KNE solids,[30,31,42] there is only one loading trajectory.

Despite the sphericity of the indenters, the indentation marks - made by both 13.5 and 5 μm indenters - clearly exhibits 3-fold symmetry (Fig. 5.6). The relationships of the terraces and steps - clearly visible on the micrograph – to each other are remarkably similar to those observed by Park et al.[76,77] (Fig. 5.1) which leads us to conclude that they are indeed $(10\bar{1}2)[\bar{1}011]$ twins.[74,76,77]

Given that the cyclic indentation stress-strain curves for $LiNbO_3$ (Fig. 5.5b) are quite similar to those observed in other KNE solids, in that they are fully reversible and hysteretic, it is reasonable to explore whether the results obtained here are consistent with our IKB model.[30,43] To do so we assumed: $G = c_{44} = 59.5$ GPa, $\nu = 0.2$, b = a-lattice parameter = 0.515 nm, $\gamma_c \approx 0.07$, and $k_1 = k_2 = 2$. According to Eqs. 1.8 and 1.9, U_{NL} vs. $\varepsilon_{NL}^{1.5}$ and W_d vs. σ^2, plots should result in straight lines, as observed in Figs. 5.7a and b, respectively. The minimum in the square of the least squares correlation coefficients, θ^2, (shown on figures) is 0.97; most are > 0.99. This agreement between theory and experiment has to be considered exceptionally good given the many simplifying assumptions made in deriving Eqs. 1.8 and 1.9, and the fact that the model assumes a uniform stress state, while the situation under the indenter is highly non-uniform.

Further analysis is possible. First, σ_t can be determined from the x-axis intercept of Fig. 5.7b. Eq. 1.2 can then be used to estimate the lengths of the IKB or the domain size, 2α. Next $2\beta_x$ and $2\beta_y$ at any σ, can be calculated. Making use of Eq. 1.8 and the slope of

the lines shown in Fig. 5.7a, $N_k\alpha^3$ can be determined. When the latter is combined with Eq. 1.9 and the slope of the lines shown in Fig. 5.7b, $\frac{\Omega}{b}$ can be estimated. Lastly, the dislocation density, ρ, can be estimated by assuming:[83]

$$\rho = \frac{4\pi N_k \alpha \beta_{av} \gamma_c}{b} \tag{5.1}$$

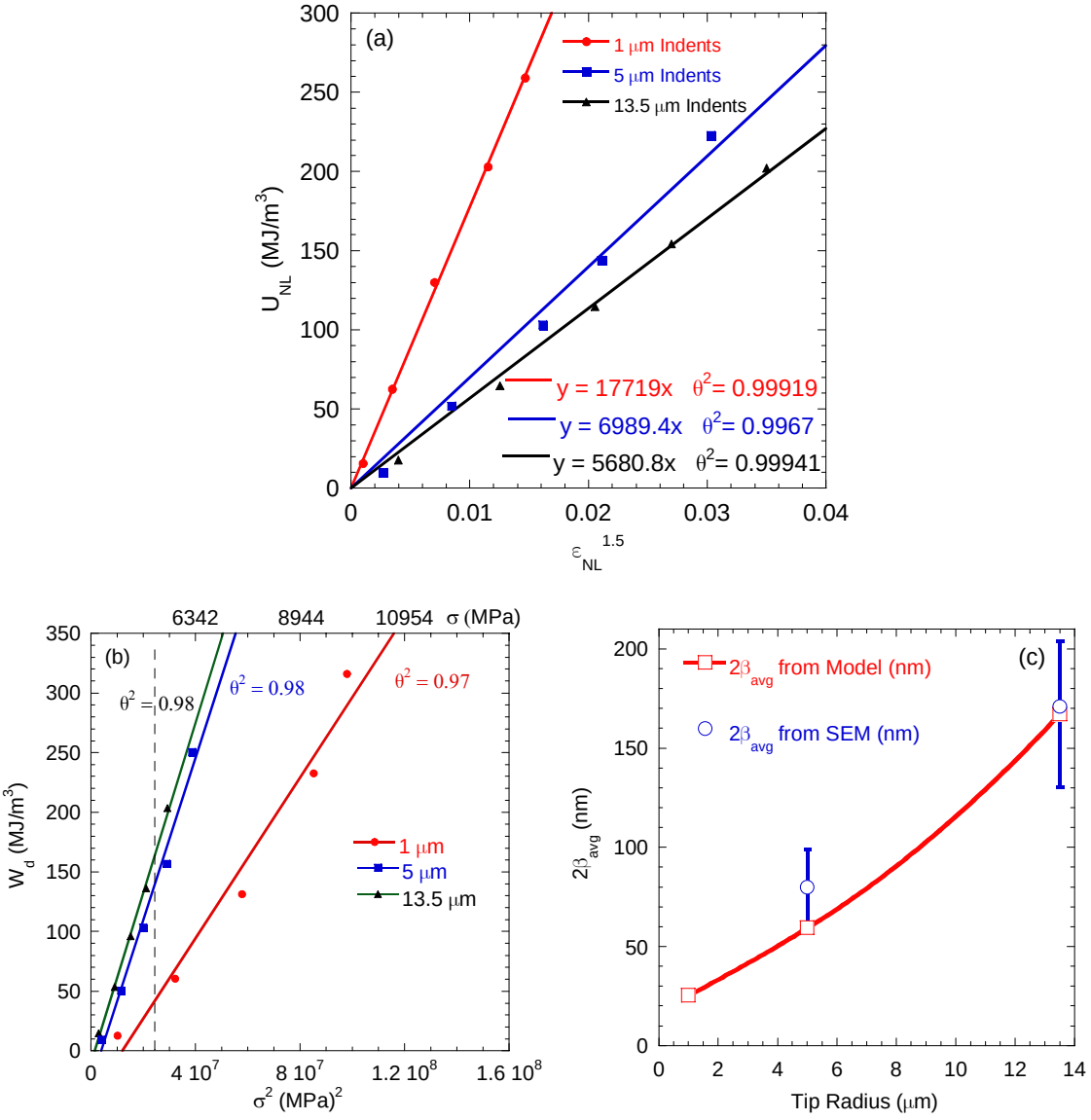

Fig. 5.7. Plots of, a) U_{NL} with $\varepsilon_{NL}^{1.5}$ and, (b) W_d vs. σ^2, as a function of indenter radius. Note high correlation coefficients ($\theta^2 > 0.9$). c) The variation of domain width, estimated from both the theoretical model (squares) and microstructural observations in SEM (circles), with R.

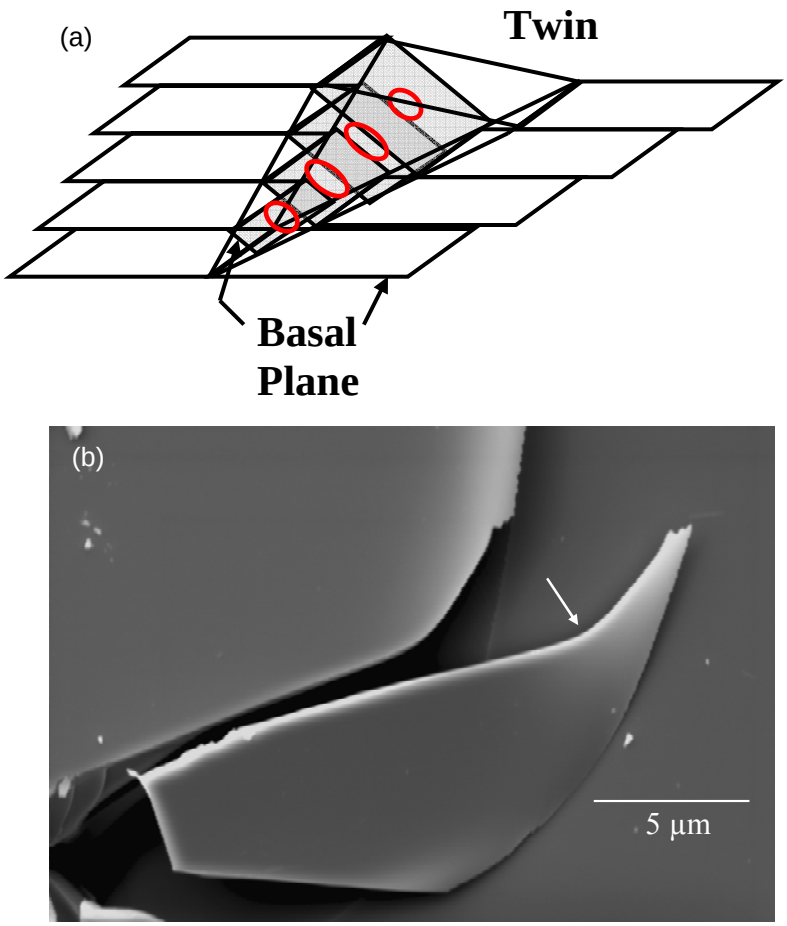

Fig. 5.8. a) A schematic of an IKB inside a twinned region. b) SEM image of a flake that formed in the vicinity of a Vickers indent, showing the curvature presumably due to the presence of basal dislocations.

Table 5.1: Dependencies of measured and calculated parameters, obtained herein, on indenter radii.

Tip radius (μm)	13.5	5	1
σ_t (GPa) from Fig. 3b	1.2	2.0	3.0
2α (nm) calculated	309	110	47
$N_k\alpha^3$	4.6	3.0	0.5
N_k (m^{-3})	1×10^{21}	2×10^{22}	4×10^{22}
Ω/b (MPa)	153	222	579
$2\beta_x$, (nm) at 5 GPa	150	53	22
$2\beta_y$, (nm) at 5 GPa	186	66	28
ρ (m^{-2}), at 5 GPa	3×10^{16}	5×10^{16}	2×10^{16}

The values for σ_t, α, β, N_k, $\frac{\Omega}{b}$ and ρ for the 3 different tip sizes are listed in Table 5.1. The calculated dimensions of the IKBs – $2\alpha \approx 310$ nm for the 13.5 μm indents, 110 nm for the 5 μm indents, and 47 nm for 1 μm indents – are quite reasonable and scale with the indenter radius. More important, as shown in Fig. 5.7c, the latter also scale with the widths of the steps formed by the 13.5 μm (Fig. 5.6a) and 5 μm indenters (Fig. 5.6b) estimated to be ≈ 171±37 nm and 80±19 nm, respectively. The steps for the 1 μm indenter were beyond the resolution of our microscope. Note that in this geometry, the IKBs should form normal to the long dimension of the step (Fig. 5.8a). Figure 5.8b shows a flake, around a Vickers indent, with a clear curvature. Since the elastic stress needed to maintain that curvature is of the order of 10 GPa, we conclude that the shape can only be maintained by the presence of basal plane dislocations, most probably arranged in a series of parallel dislocation walls.[28]

The resulting ρ's (of the order of 10^{16} m^{-2}) are comparable to heavily deformed metals[46] and are, again, reasonable considering they are calculated at a stress of 5 GPa. More importantly, and despite some differences in the shape of the loops shown in Fig. 5.5b, clearly, at the same stress, ρ is a weak function of R (Table 5.1). The importance of this conclusion lies in the fact that the crystal responds to the applied stress by forming dislocation loops whose total lengths per unit volume is apparently only a function of σ.

Combining the aforementioned results and calculations, the atomistics of the contact deformation of $LiNbO_3$ single crystal loaded along the [0001] can be reconstructed. At popin, the strain energy is converted to a large number of $(10\bar{1}2)$ twins, kink boundaries

and possibly, dislocation pileups. Twins and kink boundaries, in turn, reduce the domain size to a size proportional to the indenter radius, R (Fig. 5.7c). This is clearly manifested by the increase in σ_t with decreasing R (Table 5.1). Furthermore, that the domain size was independently confirmed from the SEM micrographs to scale with R and be comparable to that calculated from our model cannot be overemphasized.

As defined here, Ω/b should not be a function of stress and yet it is (Table 5.1). The reason for this state of affairs is unclear at this time but could be due to the large hydrostatic component that exists under the indenter.

5.3.2 A-Plane

A typical load-displacement result for the 13.5 μm indenter (Fig. 5.9a) clearly shows large pop-in during loading. Figures 5.9b shows similar deformation behavior for 1 μm indenter, with not-so-pronounced pop-in event.

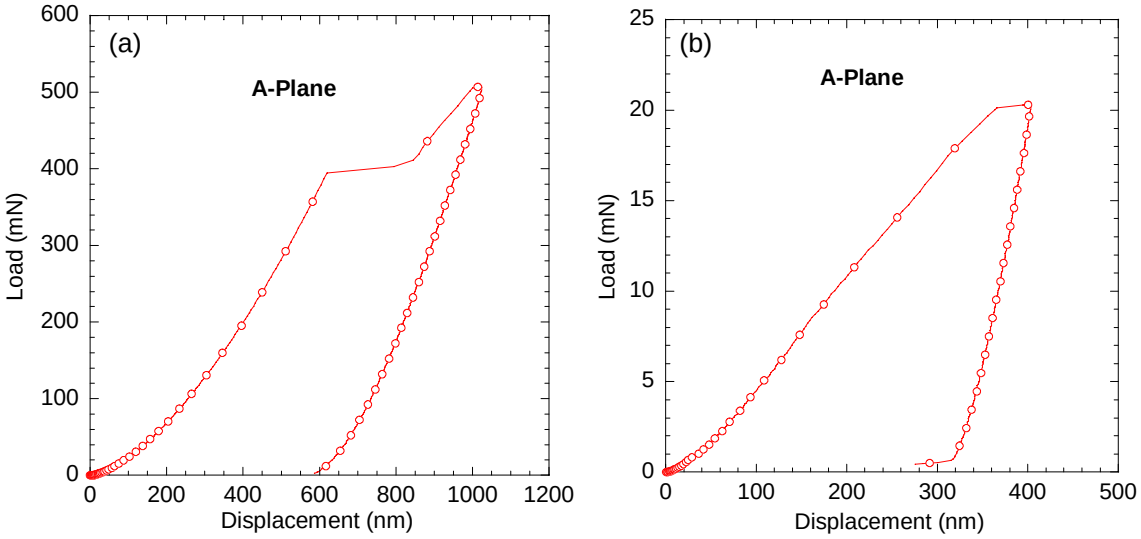

Fig. 5.9 Typical load-displacement results obtained when a A-plane $LiNbO_3$ single crystal was loaded using a spherical indenter with tip radius of; a) 13.5 μm; and b) 1 μm.

When the contact stiffness was plotted against the calculated contact radii for 13.5 and 1 μm tip sizes (Fig. 5.10), the curve was linear over the whole deformation range. The indentation modulus calculated from the slope was 190±3 GPa, which is saddled in between the modulus measured from Berkovich nanoindentation on the same surface (234±5 GPa) and the value of 1/s11 (173 GPa) calculated using the elastic constants for $LiNbO_3$.[82] The reason for the discrepancy between these numbers is unclear at this moment and more work is underway to better correlate the modulus values measured with different methods.

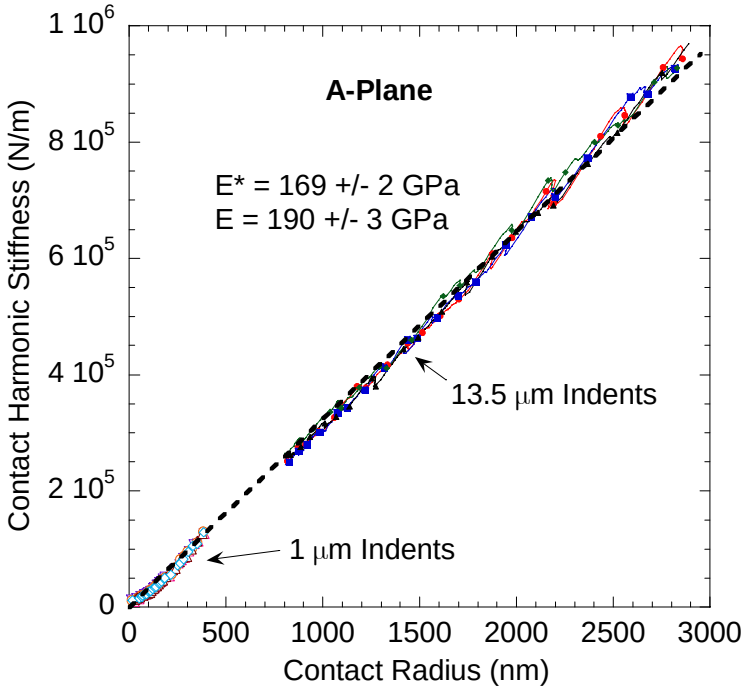

Fig. 5.10. Change in contact harmonic stiffness with contact radii for indentation on C-plane $LiNbO_3$ with 1 and 13.5 μm spherical indenters. Note the excellent agreement in slope from two extremely different tip sizes.

The first cycle indentation stress-strain curves (Fig. 5.11) - for the 2 tips explored herein - clearly show that, in the linear elastic regime, they are *not* a function of R,

lending credence to our method of obtaining these type of curves.[24] Although after the pop-in the curves exhibit a size effect, more work is needed with different tip sizes. Furthermore, at ≈ 5.7±0.2 GPa, the minima in the stress-strain curves are in reasonable agreement with the Vickers microhardness value (dashed horizontal line) measured on the same sample. The hardness measured with Berkovich nanoindentation is also shown in Fig. 5.11.

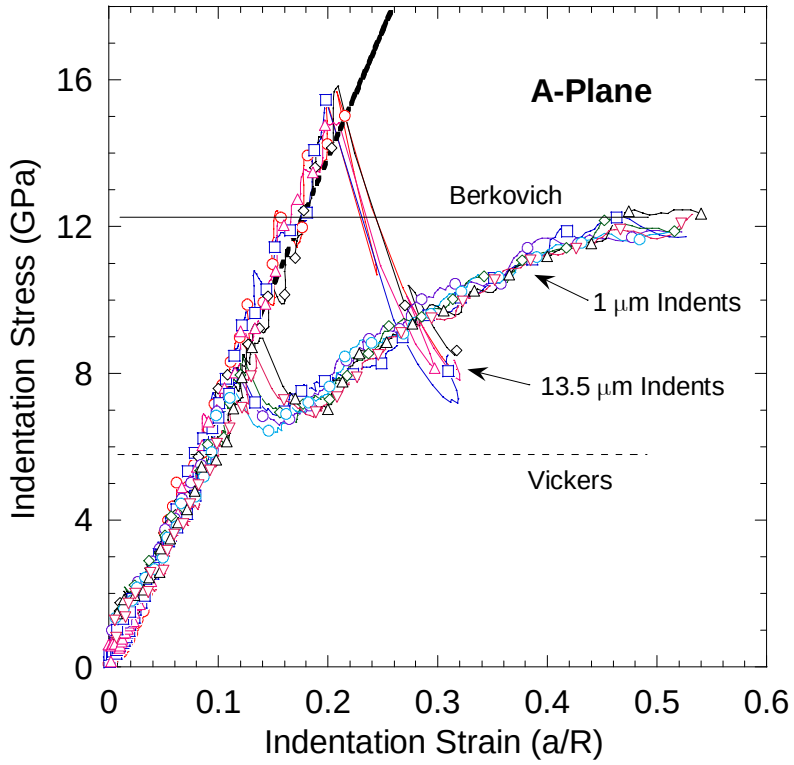

Fig. 5.11. Indentation stress-strain curves of the first cycle with the 1 and 13.5 μm indenters. Dashed and solid horizontal lines represent the Vickers microhardness and the hardness measured by Berkovich nanoindentation, respectively. The dashed inclined line represents the elastic modulus, measured from S vs. a curves.

Interestingly, and in contradistinction to ZnO (Ch. 3),[17] the A-plane shows higher hardness compared to the C-plane. This is most probably due to higher resistance to form the $(10\bar{1}2)$ twins in this orientation. This comment notwithstanding, some in-situ

indentation work is needed to better understand the effect of orientation on deformation twinning. Another interesting feature observed in Fig. 5.11 is the higher pop-in stresses for 13.5 μm indents compared to 1 μm ones. Again, from our study on pop-in stresses in ZnO,[17] it is not unreasonable to assume that there might be a very thin layer – thickness more comparable to 1 μm – of surface defects present in the A-plane sample, studied herein. It is also possible that radius of curvature might have an effect on the stress to form deformation twins – that is what happens during the pop-ins in $LiNbO_3$ single crystals.

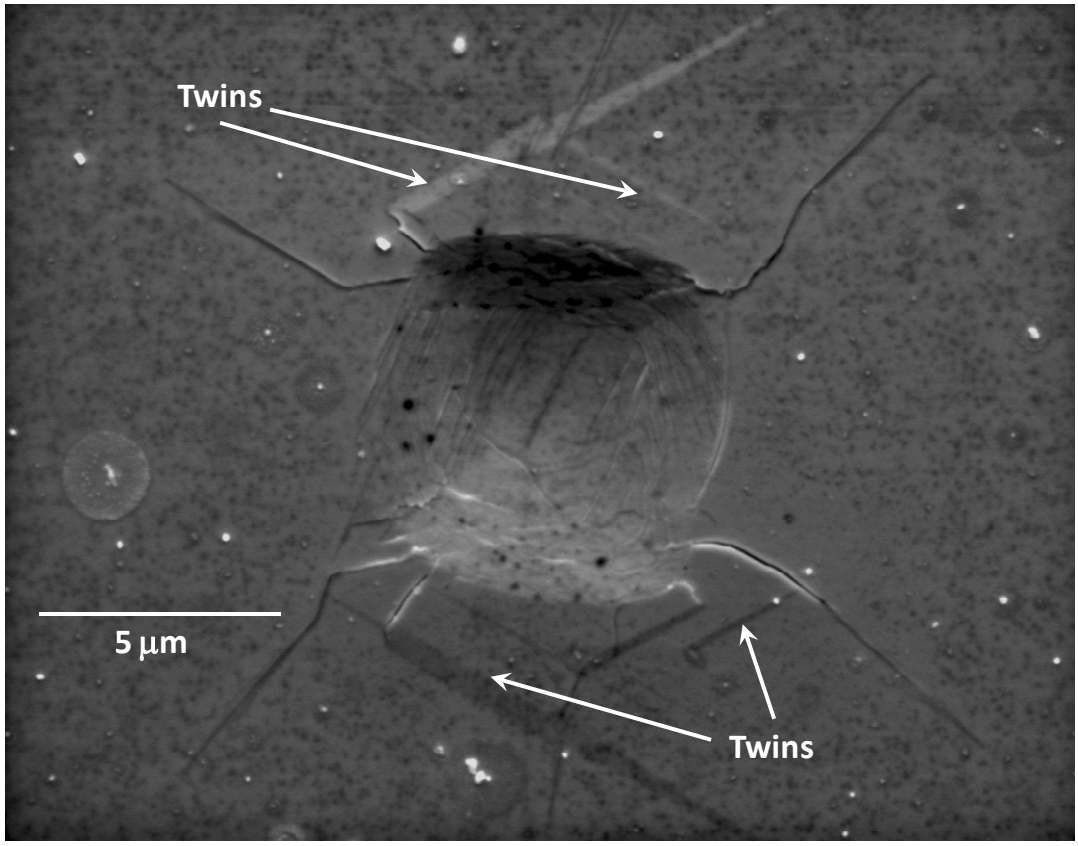

Fig. 5.12. SEM image of indentation mark made with the 13.5 μm tip loaded to 500 mN. Note the twinning outside the indented region and linear features, with two-fold symmetry, inside the indent.

The indentation marks on the A-plane sample - made by the 13.5 µm indenter – are more or less spherical (Fig. 5.12). The terraces formed by twins in this orientation are more pronounced outside the indented region and displays a four-fold symmetry. The linear features inside the indented region – with a two-fold symmetry – most probably are evidence of slip on the basal planes, oriented parallel to the indentation axis. Similar linear features have been observed when A orientation of ZnO single crystal was indented (Ch. 3).

The cyclic load-displacement results and the corresponding stress-strain curves for the 13.5 µm indenter (Fig. 5.13a and b, respectively) clearly show that while the first cycle is open, the repeat cycles are closed, fully reversible and reproducible. Note that cycles 6 to 10 are, within the resolution of our indenter, almost identical.

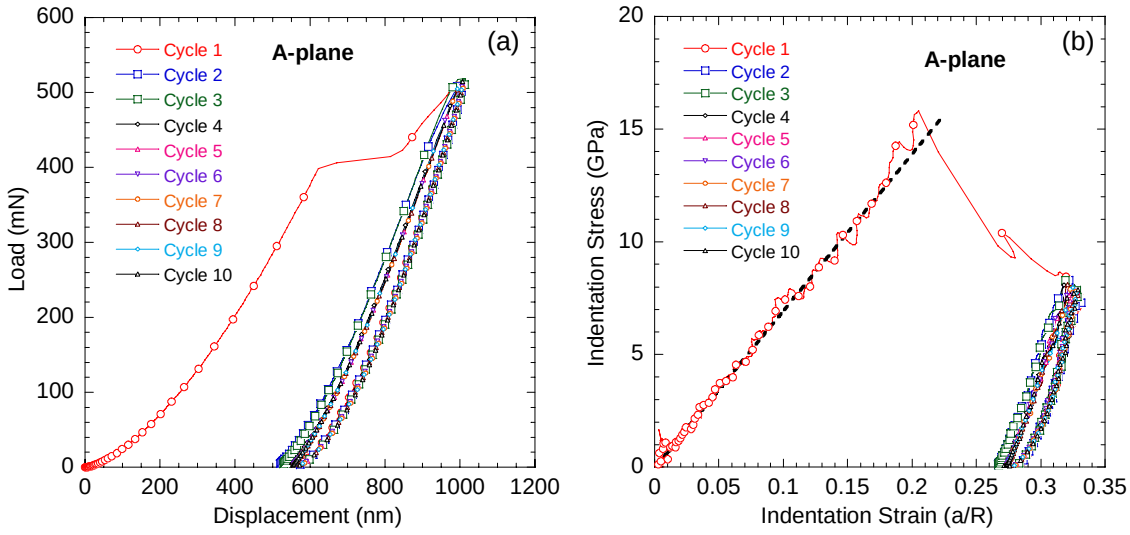

Fig. 5.13. Typical a) load-displacement; and b) corresponding stress-strain – results obtained when a A-plane $LiNbO_3$ single crystal was cyclically loaded using a spherical indenter with tip radius of 13.5 µm.

To study the reversible motion of dislocations according to our KNE model – discussed in Ch. 1 and in a similar way as the C-plane – the crystal was also indented up to different maximum loads during cyclic loading (Fig. 5.14).

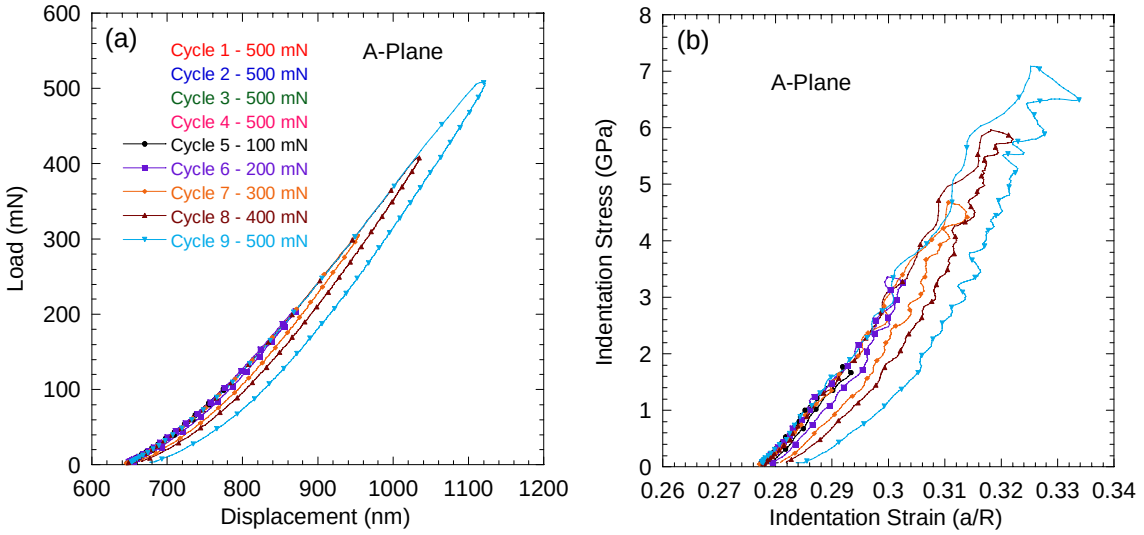

Fig. 5.14. Typical a) load-displacement; and b) stress-strain – results obtained when a A-plane $LiNbO_3$ single crystal was cyclically loaded up to progressively increased loads using a spherical indenter with tip radius of 13.5 μm.

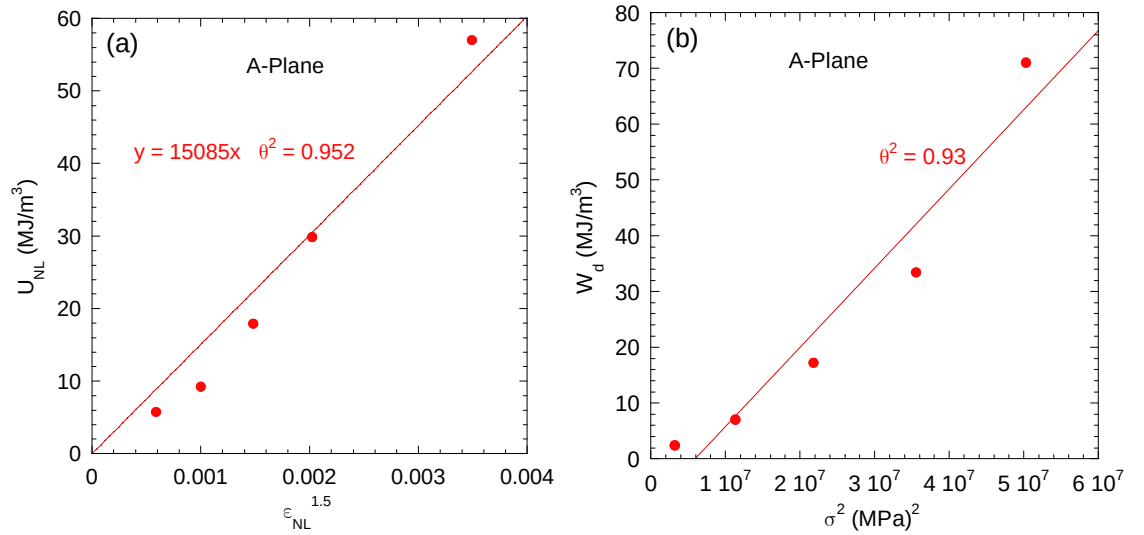

Fig. 5.15. Plots of, a) U_{NL} with $\varepsilon_{NL}^{1.5}$ and, b) W_d vs. σ^2, for the indents with 13.5 μm indenter. Note the non-linearity in both the curves, which is inconsistent with the KNE theory.

The repeat loops shown in Fig. 5.14a, were obtained by loading the 13.5 μm indenter four times to the maximum load, unloading and then reloading to progressively higher loads to generate the nested loops observed. Note that in all cases, as for all other KNE solids,[30,31,42] there is only one loading trajectory. The corresponding indentation stress-strain curves are shown in Fig. 5.14b.

To better understand our KNE model in this orientation, U_{NL} vs. $\varepsilon_{NL}^{1.5}$ and W_d vs. σ^2 plots are shown in Figs. 5.15a and b, respectively. According to Eq. 1.8 and 1.9 these two curves should result in a straight line, which is clearly not the case here. Hence, it is not reasonable to consider the deformation in this orientation of $LiNbO_3$ to be similar to that of the C-plane. Whether this is caused by the different arrangement of twins, that formed, or there are dislocation pileups – as observed in ZnO A-plane – affecting the deformation behavior still needs to be answered. Despite the deviation from the KNE model (Ch. 1), reversible dislocation motion inside the twinned domains is the most plausible explanation behind the hysteretic loops observed in Figs. 5.13 and 5.14.

5.4 Conclusions

In conclusion, we have shown that the C and A orientations of $LiNbO_3$ single crystals behave differently under spherical nanoindenter and twinning plays an important role in the deformation behavior. We note that the areas of the loops observed in C-plane $LiNbO_3$ are some of the largest seen to date, which translates to exceptionally high values of Ω/b (Table 5.1). This is especially true when Ω/b is normalized by G. For example, for the 1 μm indenter, Ω/bG for sapphire[16] was estimated to be ~ 0.007; for $LiNbO_3$ that value is ~ 0.01. This is true despite the fact that the stress under the indenter in sapphire

is substantially higher than the ones applied here. If the high values of Ω/b are not an artifact of our methodology, then it would represent an important discovery suggesting that, in addition to a high Peierls stress, another energy dissipating mechanism, most probably electrostatic in nature, is operative. In other words, it is reasonable to assume a relationship – the exact nature of which is unclear at this time - between IKBs and ferroelectric domains.

This hypothesis gains traction when it is appreciated that ferroelectric domain switching under cyclic mechanical loading has been observed for several ferroelectric materials.[84,85] For example, using in-situ neutron diffraction, during cyclic loading, on lead zirconate titanate, Pojprapai et al.[84] showed that nearly 80 % of the macroscopic strain arose from ferroelastic domain switching. Similarly Kounga Njiwa et al.[85] showed that ferroelastic domain switching can explain the hysteretic stress-strain behavior of some $BiFeO_3$-$PbTiO_3$ compositions. Interestingly, to date, and despite considerable work, there is *no* good explanation for the reversibility of these ferroelectric domains. Assuming them to be somewhat linked, or identical, to IKBs would provide the missing mechanism.

CHAPTER 6: SPHERICAL NANOINDENTATION AND DEFORMATION MECHANISMS IN FREE-STANDING GaN FILMS

6.1 Introduction

Single crystal GaN, a III-V wide band-gap semiconductor, has received a great deal of attention in the recent past due to its potential for the realization of photonic devices such as laser and light emitting diodes (LEDs) operating in the ultraviolet portion of the electromagnetic spectrum as well as solar-blind photo-detectors.[86] Its wide band-gap, high breakdown field, and high electron saturation velocity also make it an attractive candidate for the development of electronic devices operating at high temperatures, high power, and high frequency relative to competing materials such as silicon and gallium arsenide.[87,88] While GaN holds the promise for the advancement of a number of technologies, its ascension to maturity has been rather sluggish. Technological hurdles in the growth of bulk GaN by standard melt techniques and the nonexistence of a suitable lattice-matched substrate, have forced researchers to conduct the vast majority of studies in this material on heteroepitaxially grown thin films, with C-plane (0001) sapphire and silicon carbide being the traditional substrates of choice.[89] The mismatch of lattice constants and thermal expansion coefficients in such heteroepitaxy results in high dislocation densities and a high level of residual strain in the GaN film post-growth, which inevitably affects measurement of its physical properties.

To date an accurate accounting of the various physical properties of GaN remains a task of significant interest in the scientific community, requiring a decoupling of the substrate influence from the GaN layer prior to measurement. Much effort has been made to develop processes to generate thick GaN layers and subsequently separate them from their substrates as evidenced by the open literature.[90-93] Once separated, the GaN is said to be freestanding. In this work, the mechanical deformation of bulk freestanding GaN films under spherical nanoindenters is examined. Such knowledge is of great importance for realizing better manufacturing processes and device stability.

Most of the earlier nanoindentation studies, carried out on GaN thin films or bulk single crystals,[94-97] reported pop-in events during loading which were explained by the activation of pyramidal slip.[95] Yu et. al.[94] observed popins in GaN thin films deposited on sapphire substrates using both Berkovich and a 5 μm spherical indenter. Navamathavan et. al.[96] reported similar behavior when thin films deposited on sapphire substrates were indented with a Berkovich indenter. Popins due to dislocation nucleation during spherical nanoindentation were also confirmed by Caceres et. al.[97] and Kucheyev et. al.[95] On the other hand, Nowak et. al.[98] did not observe popin events when they used a Berkovich indenter on bulk crystals. Using a 4.2 μm spherical indenter, Kucheyev et. al.[95] reported that the hardness of C-plane (0001) GaN epilayers on sapphire substrates to be 15.5±0.9 GPa at 150 nm displacement into surface. The modulus value reported was 210±23 GPa. They also showed evidence of slip bands on the indented surfaces. In a more recent paper on similar films, Bradby et al.[99] using a combination of spherical nanoindentations and cross-sectional transmission electron microscopy (TEM) showed

that at loads greater than the pop-in loads, the deformation in the C-plane under the indenter was due to extensive slip, mostly on basal planes.

Recently, we have shown that spherical nanoindentation can be a powerful tool to characterize the mechanical deformation of single crystals.[11,12,16,17,23,24] This is especially true since we developed a procedure to convert indentation load-displacement curves to indentation stress-strain curves for a wide range of materials.[24] Prior to our work, there had been some attempts in that direction, but for reasons that are unclear, were not pursued and/or their usefulness was not emphasized.[10,20] In this work we apply this technique to understand the response of two different GaN surfaces to a highly localized stress. Herein repeated spherical nanoindentations, into the same location - of both C (basal) and A (prismatic) GaN orientations - with two different tip radii were carried out. We also indented the surfaces with measured Vickers and Berkovich indenters.

6.2 Experimental Details

The bulk GaN free-standing films, used in this study, were grown by Adrian Williams and Theodore D. Moustakas at Boston University, MA, using the hydride vapor phase epitaxy (HVPE) method onto both C-Plane (0001) and R-Plane $(10\bar{1}2)$ sapphire substrates. The GaN deposited on (0001) sapphire is of [0001] orientation (C-plane), while the film deposited on the latter has a $[11\bar{2}0]$ orientation (A-Plane).[100] Both GaN films were grown to a thickness of ≈ 1.3 mm. The separation of film and substrate was achieved through a novel process employing an engineered GaN buffer layer, 100 nm thick, at the hetero-interface. This buffer layer is designed to fail mechanically under the effects of thermal stress during the cooling phase of the growth process, thereby

liberating the GaN layer from the substrate. Details of this method can be found in Ref. 101.[101]

The nanoindentation experiments were performed at room temperature, using a nanoindenter (XP system, MTS Corp, TN) with a continuous stiffness measurement (CSM) attachment. Two diamond hemispherical indenters with radii, R, of 13.5 μm and 1 μm were used. The radii of the sphero-conical tips were verified by careful measurements in a scanning electron microscope, SEM. A constant loading rate/load ratio of 0.1 was employed. Typically, the tip was indented into the *same* location at least 5 times at a given load. To correct for a small instrumental drift, the unloading segments of the second and subsequent cycles were shifted so as to align them with the corresponding unloading segment of the previous cycle. This was only carried out, if and only, if successive cycles had identical areas under the load-displacement curves. Once corrected, the load-displacement data were converted to indentation stress-strain curves, following the protocol explained in Ch. 2.

Post-indentation surface features were examined using a SEM (FEI, XL30). We also measured the Vickers microhardness using a load of 10 N. The moduli and hardness values of the two surfaces were also measured using a Berkovich indenter and the Oliver and Pharr method.[2]

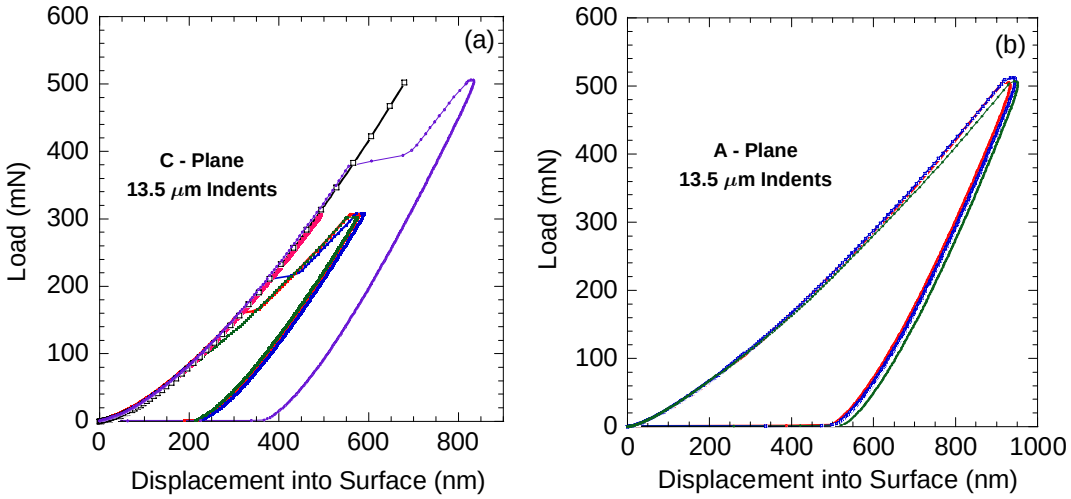

Fig. 6.1. Load-displacement response for spherical nanoindentation of GaN free-standing films with a 13.5 μm indenter up to a 500 mN load. a) C orientation; b) A orientation.

6.3 Results and Discussion

6.3.1 C-Plane

Typical nanoindentation load-displacement results for the C-orientation obtained with the 13.5 μm indenter in 6 different locations (Fig. 6.1a) were characterized by pop-ins. The pop-in loads were quite variable; their extent increased as the pop-in loads increased. After the pop-ins, the loading and unloading curves taken to the same maximum load for all locations coincided. In one location (open squares in Fig. 6.1a) the response was linear elastic up to the maximum load of 500 mN.

Since S = 2aE*, where E* is the effective spherical indentation modulus of the sample, it follows that the latter can be readily determined from S vs. a plots.[24] Such plots, for both orientations and for both indenter tips, are shown in Fig. 6.2. (The results for the A-plane, are shifted to the right by 2000 nm for clarity.) The 13.5 μm indents on the C-plane resulted in a sample modulus, E, of 212±9 GPa, which is in excellent agreement with the value of 210±23 GPa, where a 4.2 μm radius spherical indenter was

used.[95] The moduli values obtained when the 1 μm indenter was used - 297±15 GPa - are significantly higher. At 261±3, the Berkovich modulus is in between the two. Clearly the indentation moduli are tip size and shape dependent. At this time the origin of these differences are not understood; more work is needed to understand them. Note that $1/s_{33}$ for GaN is 328 GPa[57] and thus, for this orientation, the result for the 1 μm indenter are the closest to the theoretical value. This comment notwithstanding, it is hereby acknowledged that the indentation elastic modulus is not necessarily equal to $1/s_{33}$, but is a more complicated function of the elastic constants.[102]

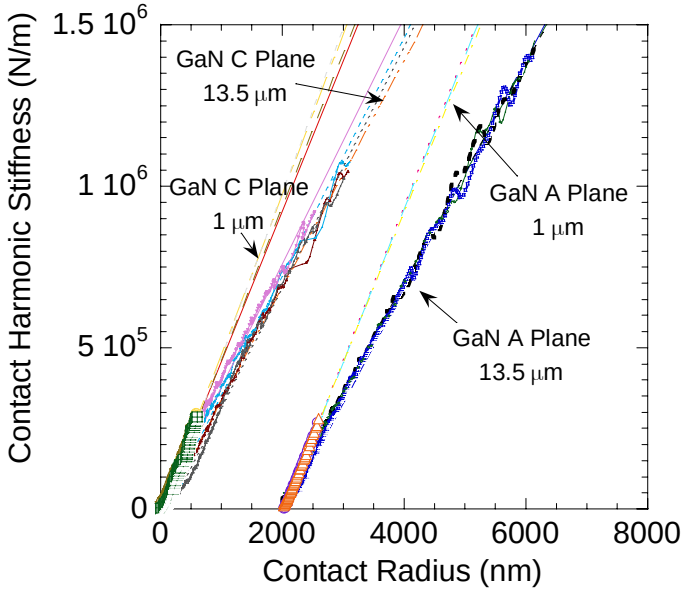

Fig. 6.2. The variation in harmonic contact stiffness, S, with contact radii, a, for both C and A orientations measured with the 1 μm and 13.5 μm spherical tips. The results for the A plane are shifted by 2000 nm to the right for clarity.

Typical indentation stress-strain curves, for both tips, obtained on the C-plane are shown in Fig. 6.3a. The zero-point corrections (see Ch. 2) were of the order of ± 2 to 5 nm. The curves are characterized by a linear elastic region (the dashed inclined lines correspond to the moduli determined from Fig. 6.2 for the two indenter tips), followed by

a, not too precipitous, drop in stress that accompanies the pop-ins. After the pop-ins, the stress either remains more or less constant at ≈ 10 GPa for the 13.5 μm indents (Fig. 6.3a), or exhibits a shallow minimum, after which it increases more or less linearly at a slope that is significantly lower than the slope during the elastic regime. The pop-in stresses are quite stochastic for both indenter sizes. Note that for the former no results are obtained for indentation strains > 0.27 since that was the limit of our load; for the 1 μm indenter the results were truncated at a strain of 0.5, which corresponds to the maximum depth up to which the assumption that the indenter was spherical is valid.

For reasons that are not clear, and despite the fact that the slopes of the S vs. a lines in Fig. 6.2 for the 1 μm and 13.5 μm are different, when these results are used to obtain the indentation stress-strain curves, the initial slopes of the latter are almost identical. In other words, they are not different, as one would expect. The same is true of the A-plane (see Fig. 6.3b). Such a discrepancy was not observed in either ZnO (Ch. 3),[17] sapphire (Ch. 7)[16] or $LiNbO_3$ (Ch. 5)[18] where both tips resulted in almost identical moduli and is thus not an artifact of our procedure.

Interestingly, and possibly coincidentally, the stress level after the pop-ins for the most part fall in between the Vickers microhardness value – 10.9±0.1 GPa (shown as dashed horizontal line in Fig. 6.3a) and Berkovich nanoindentation values – 15.2±0.1 GPa (shown as horizontal solid line in Fig. 6.3a). The Vickers hardness values measured herein are in reasonable agreement with earlier reported values for GaN.[103] This comment notwithstanding, defining a hardness value from the spherical nanoindentation stress-

strain curves is problematic because of work hardening. The same was true for the single crystals of sapphire[16] and ZnO.[17]

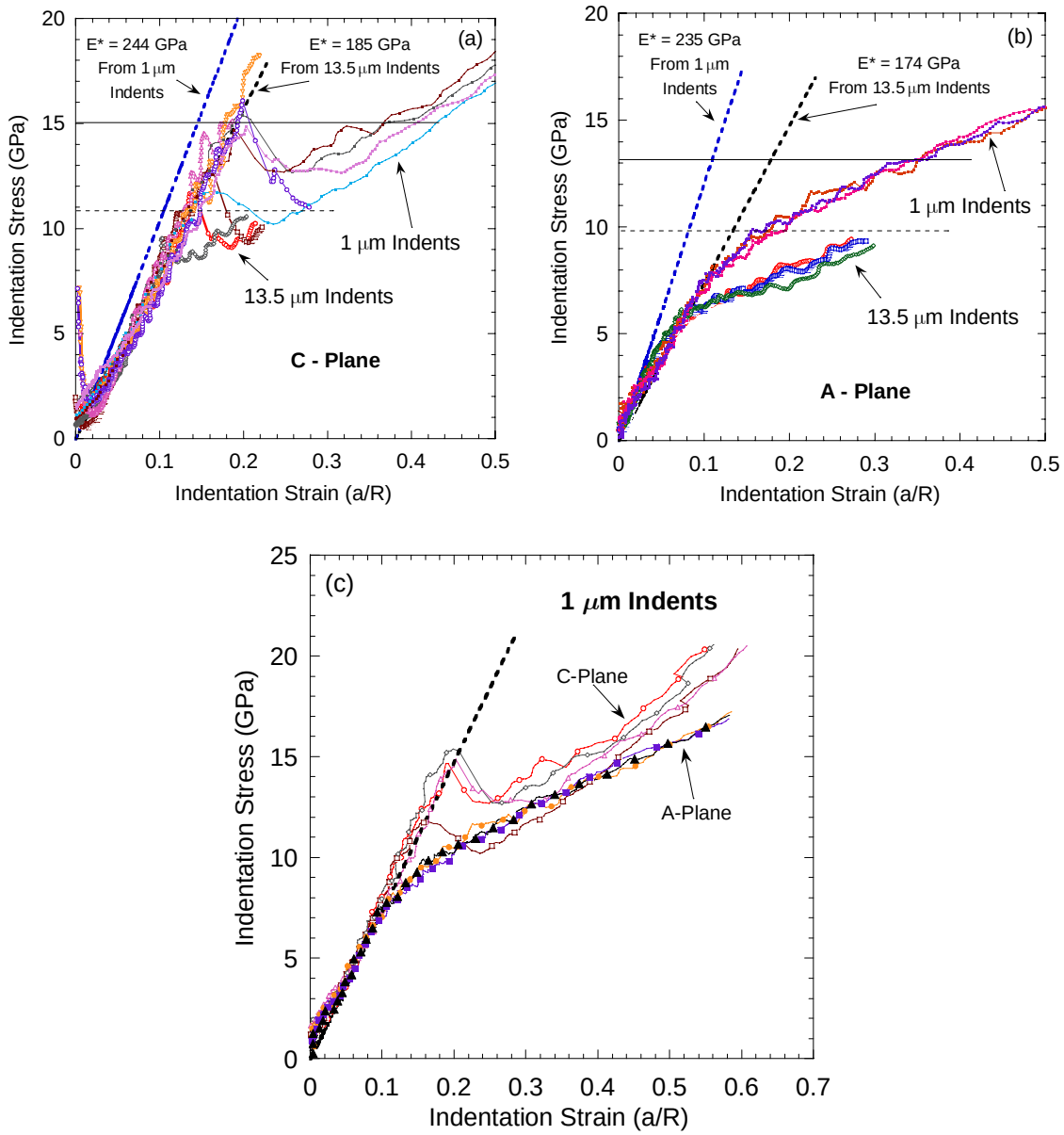

Fig. 6.3. Indentation stress strain curves for the first loading calculated from the load displacement results of both 1 and 13.5 μm nanoindenters for the, a) C orientation, and, b) A orientation. The dashed and solid horizontal lines represent the Vickers and Berkovich hardness values, respectively. c) Superimposed indentation stress-strain curves for the 1 μm indents on both C and A-orientation. Note almost similar hardening rate for the two orientations.

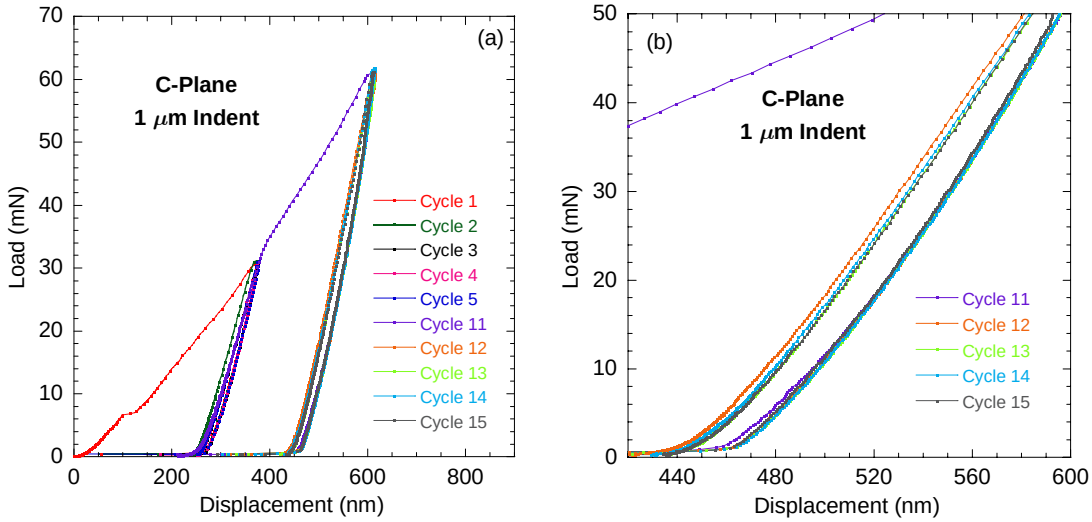

Fig. 6.4. a) Spherical nanoindentation load-displacement response on the C-orientation for repeated spherical nanoindentation on the same location with the 1μm indenter. The applied load was 30 mN for the first 10 cycles and 60 mN thereafter. b) The magnified view of cycles 11 to 15. Note the fully reversible hysteretic loops in this orientation.

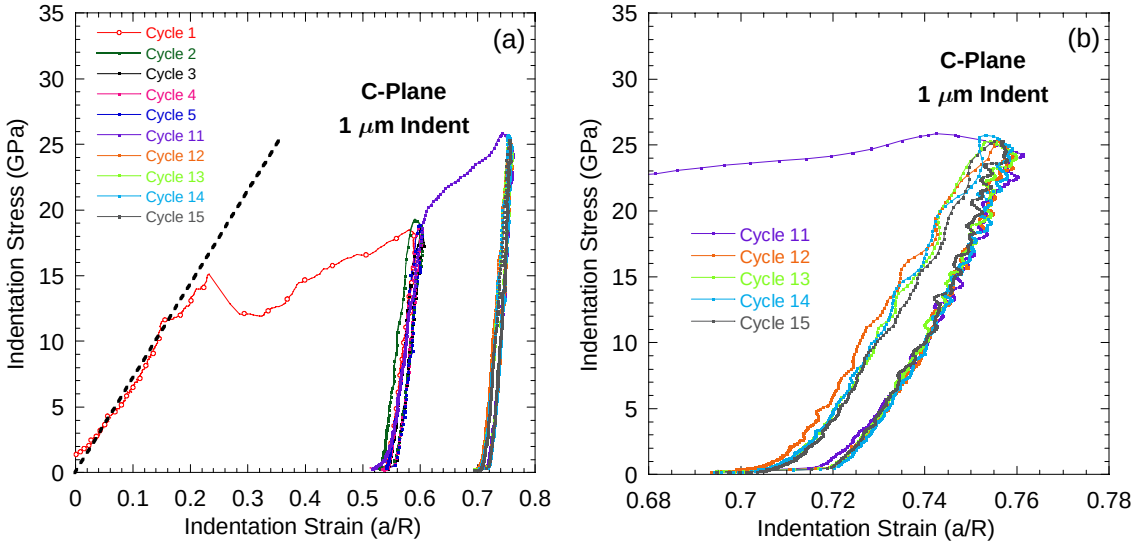

Fig. 6.5. a) Spherical nanoindentation stress-strain response corresponding to the data shown in Fig. 6.4a. b) The magnified view of cycles 11 to 15. Note the fully reversible hysteretic loops in this orientation.

Typical nanoindentation load-displacement plots for the repeat cycles in a given location are shown in Fig. 6.4a. Here the same location was indented first to a load of 30 mN for 10 cycles with the 1 μm spherical tip before increasing the load to 60 mN for another 10 cycles. Note the fully reversible and reproducible nature of the loops at each

load (Fig. 6.4b). The corresponding indentation stress-strain curves are shown in Fig. 6.5. As discussed below, we take that to be evidence for the formation and annihilation of incipient kink bands, IKBs, and/or the to-and-fro movement of mobile dislocation walls.

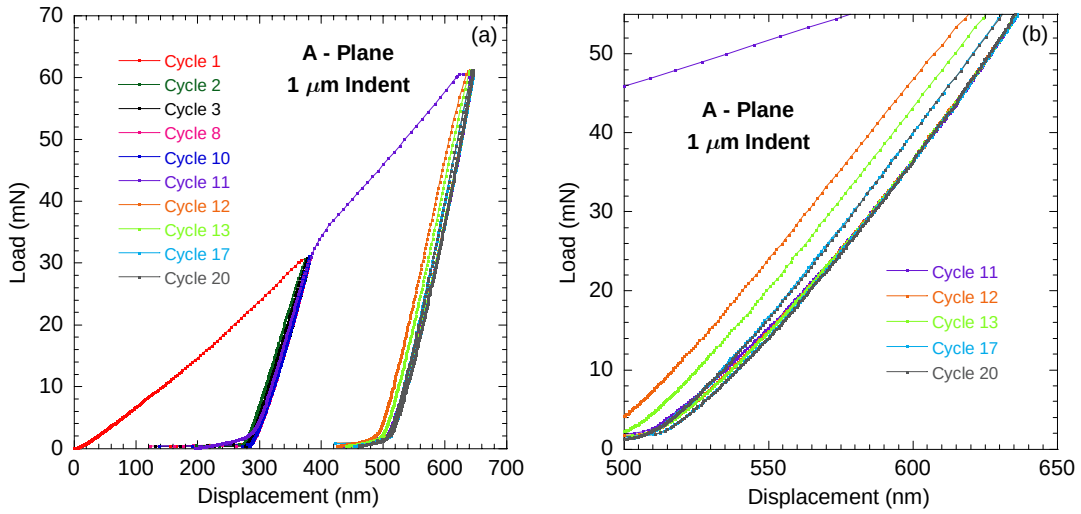

Fig. 6.6. a) Spherical nanoindentation load-displacement response on the A-orientation for repeated spherical nanoindentation on the same location with the 1μm indenter. The applied load was 30 mN for the first 10 cycles and 60 mN thereafter. b) The magnified view of the cycles 11 to 20. Note the hysteretic nature of the loops decreases with number of cycles.

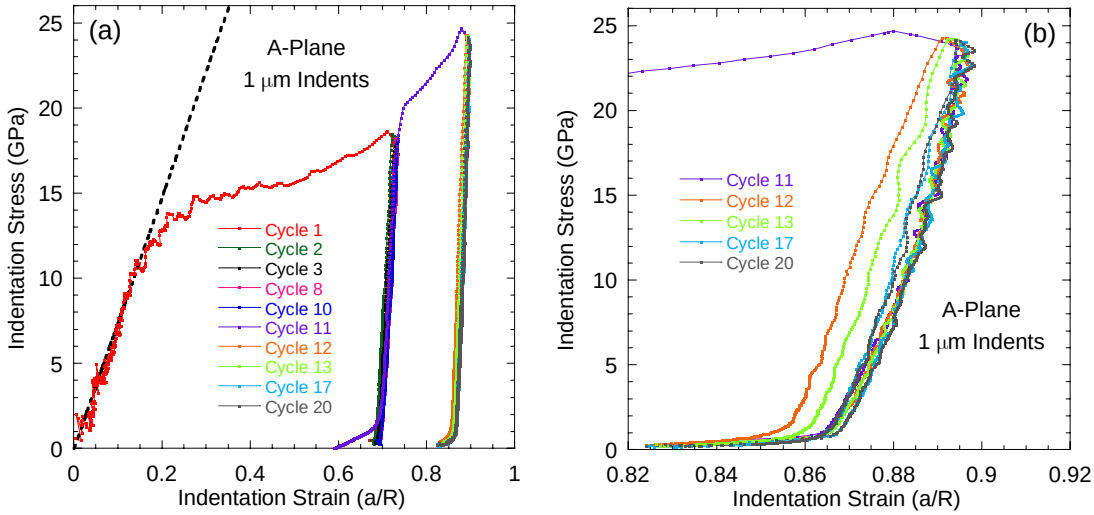

Fig. 6.7. a) Spherical nanoindentation stress-strain response on the A-orientation corresponding to the data shown in Fig. 6.6a. b) The magnified view of the cycles 11 to 20. Note the hysteretic nature of the loops decreases with number of cycles.

6.3.2 A-Plane

Typical load-displacement plots for the A-plane are shown in Fig. 6.1b. In this orientation pop-in events were not observed. The S vs. a plots (Fig. 6.2) clearly show that the slopes obtained are a function of indenter diameter. The 13.5 μm indents yield a modulus of 196±5 GPa; the 1 μm indents, 284±6 GPa. The Berkovich indenter yielded a modulus of 255±3 GPa, viz. a value in between the other two values. Note that $1/s_{11}$ for GaN is 226 GPa.[57]

The dashed inclined lines in Fig. 6.3b correspond to the moduli measured by the 13.5 μm and 1 μm tips obtained from Fig. 6.2. Like in Fig. 6.3a, the initial slopes of the indentation stress strain plots are almost identical for the 1 μm and 13.5 μm indenters. In other words, the former are lower than one would expect based on the results shown in Fig. 6.2.

Here again, coincidentally or not, our results are in reasonable agreement with the Vickers microhardness value of 9.9±0.3 GPa (horizontal line marked V in Fig. 6.3b) and the Berkovich nanoindentation value of 13.2±0.2 GPa (horizontal line marked B in Fig. 6.3b) measured herein on the same surface. Note that data shown in Fig. 6.3b represent the limits of the load on our nanoindenter and the sphericity of the 1 μm indenter.

The typical indentation stress-strain curves, obtained for both tips in various locations (Fig. 6.3b), are characterized by a linear elastic regime, followed by what appears to be a "yield" point, beyond which the response is still linear, but at a different slope. In contradistinction to the results obtained for the C-plane (Fig. 6.3a), the variability between the results from the various locations is significantly reduced. The absence of

popins and the reduced variability is most probably due to a high defect concentration at and/or near the surface (see below).

The spherical nanoindentation load-displacement plots for repeat cycles in the A-orientation in a given location are shown in Fig. 6.6a. Here also the same location was indented, at 30 mN, for 10 cycles, and then to 60 mN for another 10 cycles with the 1 μm indenter. The corresponding indentation stress-strain curves are shown in Fig. 6.7a. In this orientation subsequent loop areas get progressively smaller with cycling until they saturate (Figs. 6.6b and 6.7b), but at an area much smaller than that obtained for the C-plane (Figs. 6.4b and 6.5b). Figure 6.6b shows the repeated indentation result in the same location on the A surface with the 1 μm indenter and up to 60 mN. Note that, unlike the C surface, the areas encompassed by the loops are reduced to a considerable extent up to cycle 17, before becoming almost constant.

6.3.3 Possible Deformation Mechanisms

Earlier work has shown that when the C planes of GaN are indented, basal slip is activated. In agreement with previous work,[24,48,95] there is little evidence for plastic deformation prior to the pop-ins (Fig. 6.3a). The excellent reproducibility of results - from location to location - *after* the pop-ins (Figs. 6.3a and b) is also consistent with a dislocation-based mechanism.

The variations in pop-in stresses suggest that - like in ZnO[17] - the initial defect concentrations on and/or near the surface is the rate-limiting factor. The effect of defects, or lack thereof, on pop-in stresses was best illustrated by Nowak et. al.,[104] who implanted Ni^{2+} and Au^{2+} ions into sapphire single crystals and showed that with increasing defect

concentrations, the popin stress decreased substantially. It follows that the fact that the A-plane did not exhibit popins could thus be either due to the fact the deformation is accommodated by basal slip for which nucleation of dislocations is *not* rate limiting and/or the surface is quite defective. The latter is the more probable, however, since popins were observed in this orientation in ZnO single crystals.[17] The nature of these defects is not clear, but recent work suggests it could be threading dislocations.[60]

In sapphire where presumably all slip is basal, the stress-strain curves both before and after the pop-ins for both C and A orientations were almost perfectly superimposable.[16] This is also true in this work. If the 1 μm indentation results were superimposed (Fig. 6.3c), it becomes evident that the strain hardening rates after the pop-ins are almost identical. It is thus reasonable to implicate basal slip for the deformation in the A orientation as well. In contradistinction, in ZnO single crystals, the flow stress for pyramidal slip was higher than basal slip and the hardening rates were quite different in the C and A-directions (Ch. 3).[17]

6.3.4 Kinking Non-Linear Elasticity

Recently we postulated that most solids with c/a ratios > 1.5 belong to the same class of solids we labeled kinking nonlinear elastic, KNE.[11,30] Experimentally, the signature of KNE solids is the formation of fully reversible, hysteretic stress-strain loops on repeat loadings.[31] This full reversibility is due to the formation of incipient kink bands, IKBs, that are comprised of two nearly parallel, dislocation walls of opposite polarity attracted to each other such that when the load is removed they annihilate. Given that the response of the C-plane to repeated indentations is indeed fully reversible and hysteretic (Figs. 6.4

and 6.5) we conclude that IKBs are implicated. This response is similar to the deformation behavior observed in other KNE solids such as layered ternary carbides,[23,31] mica,[11] graphite,[12], and more recently, sapphire,[16] ZnO[17] and $LiNbO_3$[18] single crystals.

The energy dissipation per cycle, per unit volume, W_d, is the area enclosed by the fully reversible hysteretic loops in the indentation stress-strain plots (Figs. 6.5b and 6.7b). To measure W_d usually the last cycle is used. The W_d (~ 20 MJ/m^3), for the repeated indentations on C-plane samples can be possible only by to-and-fro motion of dislocations.[31] The other two possibilities – fracture and phase transformation – can readily be ruled out as fracture cannot lead to hardening as observed in Fig. 6.3a and there is no evidence of a phase transformation in GaN at the stresses reported here.

To examine the assumptions of our IKB model[30] - embodied in Eqs. 1.1 to 1.10 - we need to estimate γ_c. From Fig. 6.3a, the threshold stress for the formation of the initial KBs (the popin stress) is ≈ 12 GPa. Assuming the shear stress under the indenter is ≈ half the normal stress, it follows that τ_c in Eq. 1.3 is ≈ 6 GPa. For GaN c_{44} is 241 GPa[57] and consequently, $\tau_c \approx c_{44}/40$, which is not unreasonable. Assuming, $G = c_{44} = 241$ GPa, $\nu = 0.2$, and $b = a = 0.319$ nm, [105] from Eq. 1.3 we calculate γ_c to be ≈ 0.05. Hence, the distance between two parallel dislocation loops, D, inside an IKB, is almost 6.4 nm. In other words, a dislocation is present along the c-axis every ≈ 64 Å. (The c-lattice parameter is 5.185 Å[105]) and the total length of the IKB, 2α, as calculated from Eq. 1.2, is 51.5 nm. Then according to Eq. 1.10, $\Omega/b \approx 1 \pm 0.4$ GPa. According to our previous work it was postulated that Ω/b should be of the order of, if not identical to, the critical resolved shear stress of basal plane dislocations.[30] Therefore our values are, given all the

assumptions made in obtaining them, quite reasonable and lend credence to both our model and results.

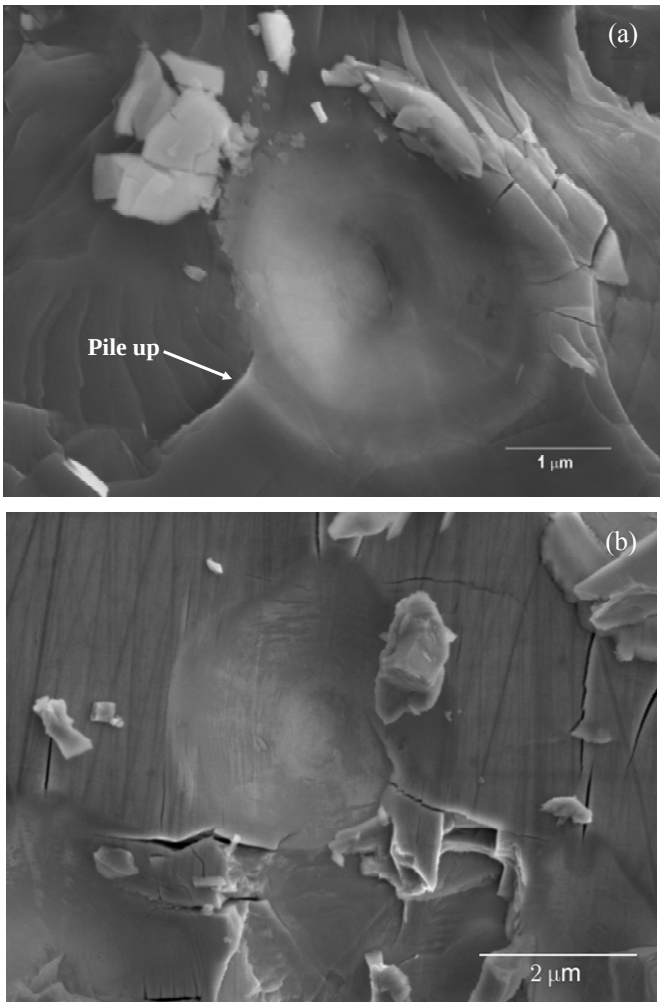

Fig. 6.8. Scanning electron micrograph of an indented region on, a) C-orientation; and b) A-orientation. The surface damage was caused by closely spaced (≈ 20 μm) square (4 x 4) array indentations made with the 13.5 μm tip and a 400mN load.

Like in sapphire,[16] we believe that the small hysteretic areas immediately after the pop-ins (i.e. during cycles 2 to 10 in Figs. 6.4a and 6.6a) is a consequence of the fact that the size of the domains (viz. 2α) that form at that juncture are too small for the initiation of IKBs, i.e. the applied stress is smaller than the threshold stress given by Eq. 1.2. This

is presumably why loading to the higher stresses results in larger loops, at least in the C-direction (Fig. 6.4b).

When a close square array of 400 mN indents with the 13.5 μm spherical tip were imaged in the SEM (Fig. 6.8), no slip lines – as in ZnO[17] - were observed. This does not mean they do not exist, however. Kucheyev et al.[95] observed clear traces of slip lines in GaN thin films; interestingly the slip lines did not trace out hexagons but parallelograms. These slip lines cannot be due to basal slip. More importantly, however, are the room temperature cathodoluminescence, CL, images of the indents by the same authors.[95] In those images a 6-fold symmetry – Star of David configuration, consistent with basal slip in three directions at an angle of 60^o (Fig. 3.13b) to each other and comprised of a series of parallel lines - is clearly visible. The star extends considerably *beyond* the contact diameter. This last observation cannot be overemphasized since it implies that the defects were *mobile* and clearly resulted from the indentation. It is important to note that another possible source of energy dissipation could be the to-and-fro motion of these mobile dislocation walls, MDWs.

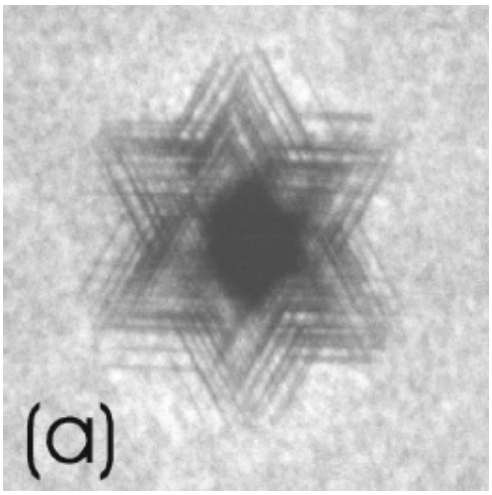

Fig. 6.9 Room temperature monochromatic CL image of a 900 mN indent in a GaN epilayer with a spheroconical tip of radius 4.2 μm (taken from Ref. 95).[95] The horizontal field width is 50 μm.

As discussed earlier in case of ZnO single crystals,[17] Fig. 3.13 shows how basal slip can cause the formation of MDWs and/or permanent kink boundaries.[64] It also explains the formation of pile-ups around the indented region, shown in Fig. 6.8a and also reported in Ref. 95.[95] In light of the above discussion and in conjunction with the results obtained on ZnO,[17] which has a similar crystal structure, it is reasonable to conclude that the defects observed in the CL images (Fig. 6.9)[95] are nothing but MDWs – the precursors of kink boundaries – and/or kink boundaries.[23,64] Note that neither pyramidal nor prismatic slip can account for these features. In situ CL studies, while a surface in being indented, are indicated and could prove to be invaluable. Also consistent with this conclusion is the *lack* of pileup in the A direction (Fig. 6.8b). Here presumably the kinking occurs, along with dislocation pileups, directly under the indenter in a similar way as in ZnO.[17] CL and/or XTEM studies of indents in this direction should confirm this hypothesis. Lastly in the section we note that Fig. 6.8b is quite reminiscent of indentations in the A planes of Ti_3SiC_2[23,63] in that there are no pile-up around the indentation, and microcracking – presumably parallel to the basal planes - is observed. Since in Ti_3SiC_2 deformation occurs strictly by basal slip, we assume the same occurs here. And while these observations do not prove that basal slip alone is implicated, they certainly show that the features observed can be obtained by basal slip alone.

It was postulated earlier that high c/a ratios render non-basal slip prohibitively expensive. Thus only kink band formation - made possible by basal slip - can be activated during deformation.[11,31] The results of this work are consistent with these notions since our results for the C-plane can be explained by invoking only basal slip. The fully

reversible loops (W_d is ~ 20 MJ/m^3) during the repeat cycles observed herein (Fig. 6.4b) suggest the GaN films explored herein belong to the larger group of KNE solids. Also based on our results, it is clear that the extent or even the observation of kinking nonlinear elastic deformation of hexagonal crystals depends on orientation since what is occurring in the A-direction is less clear. What is clear, however, is that in this orientation the area within the reversible loops are smaller than those that form when the C planes are indented. More single crystal work is needed to understand the variations in response of various orientations.

6.4 Summary and Conclusions

By converting load-depth of penetration curves to stress-strain curves, together with post-indentation SEM observations and previous work[95,99] we conclude that basal slip is initiated when both C- and A-orientations of GaN are indented with spherical nanoindenters. This is in contradistinction to our results on ZnO[17] single crystals where a large hardness anisotropy is observed due to the activation of two different slip systems.

The reversibility during the cyclic nanoindentation – specially in the C-orientation – was similar in nature to other KNE solids suggesting that IKBs form under the indenters. The formation and annihilation of these IKBs, in turn, result in considerable amounts of energy dissipation per cycle. The possibility of the to-and-fro motion of MDWs also cannot be excluded at this time.

The results presented herein should in principle be helpful when understanding machining damage and ultimately device stability. Lastly, this work is another example of how nanoindentation stress-strain curves can be used to shed important light on the

atomistics of the deformation processes in single crystals, that would be otherwise very difficult, if not impossible, to obtain.

CHAPTER 7: KINKING NONLINEAR ELASTIC DEFORMATION IN SAPPHIRE

7.1 Introduction

Understanding the room temperature plastic deformation of sapphire (α–Al_2O_3) single crystals is important for applications involving high speed loading or localized high stresses, as well as the polishing and machining of sapphire single crystals.[106] It is reasonably well established that at temperatures greater than ≈ 1100 °C, basal slip - with a Burgers vector of 0.476 nm - is the easy slip system. Sapphire single crystals loaded nearly parallel to their basal planes, above 1350 °C, form easily identifiable macroscopic kink bands.[107] At room temperature, sapphire will plastically deform, provided the hydrostatic pressure is sufficient to suppress fracture.[108] Since such conditions are naturally present under an indenter tip, and with the advent of instrumented nanoindenters, a number of papers have been published lately that have attempted to understand the deformation of sapphire single crystals. A comprehensive recent review can be found in a paper by Tymiak et al.[109]

Of special interest to our work are the basal C (0001) and prismatic A ($1\bar{2}10$) planes, subjected to spherical indentations.[109,110,111,112] During loading, sudden pop-ins are recorded. In analogy with metals, these pop-ins have been assumed by some to be evidence of a plastic or yield-point transition. It should be noted here however, that pop-

ins as large as the ones measured herein, and in previous work on sapphire, have never been reported for metals. To date the exact nature of what is occurring at the "yield point" is unclear. Some maintain the yield point corresponds to the nucleation of dislocations, others that dislocations nucleate before the observed yield point, with the latter a plastic instability that commences upon reaching a critical condition of a certain kind.

Recently we postulated that most solids, if not all, with c/a ratios > 1.5 belong to the same class of solids we labeled kinking nonlinear elastic, KNE.[11,30] The logic being that high c/a ratios render both non-basal slip and twinning prohibitively expensive. Thus only basal slip and kinking (made possible by basal slip) can be activated during deformation. Experimentally, the signature of KNE solids is the formation of fully reversible, almost rate-independent, hysteretic stress-strain loops on repeat loadings.[31] This full reversibility has been attributed to the formation of incipient kink bands, IKBs, that are comprised of two, nearly parallel, dislocation walls of opposite polarity attracted to each other such that when the load is removed they annihilate (see Ch. 1).[31]

The purpose of this work is to shed more light on the room temperature deformation of sapphire and provide compelling evidence that sapphire can deform by the formation of kink bands even at room temperature. This was carried out by repeatedly (up to 30 times in some cases) loading a 1 μm radius diamond sphere, into the same location, on C and A sapphire planes.

7.2 Experimental Details

In this work we tested two - C and A orientations - sapphire single crystals (Kyocera Industrial Ceramics, Vancouver, WA). A 1 μm radius spherical diamond tip indenter was used with our nanoindenter (XP System, MTS Corporation, Oak Ridge, TN). A constant loading rate over load ratio of 0.1 was used in each test. Typically, each location was indented 5 times, to a load of 50 mN, followed by up to 30 indentations in the same location to a load of 100 mN. The protocol, described in Ch. 2, was then used to convert the load-displacement plots to indentation stress-strain curves.

The post-indentation surface features were scanned with atomic force microscopy, AFM, (MFP-3D, Asylum Research) in a non-contact mode using an Olympus AC 240 tip. The indented surfaces were also coated with Pt and examined using a field emission scanning electron microscope, FESEM (XL30, FEI Corporation, Hillsboro, OR).

An estimate of W_d was obtained by measuring the loop areas from figures similar to the ones shown in Figs. 7.1b and 7.3b, and dividing the result by πa^3. In so doing it is implicitly assumed that the volume under the indenter affected is a cylinder of radius and height a. This assumption has previously been shown to be reasonably valid.[23]

7.3 Results

7.3.1 C-Plane

Typical load-displacement results for the C-plane are shown in Figs. 7.1a and b; the S vs. a curves are shown in Fig. 7.2. The corresponding indentation stress-strain curves are shown in Fig. 7.5a. In this orientation a relatively large (≈ 100 nm) pop-in is observed at ≈ 20 mN (Fig. 7.1a).

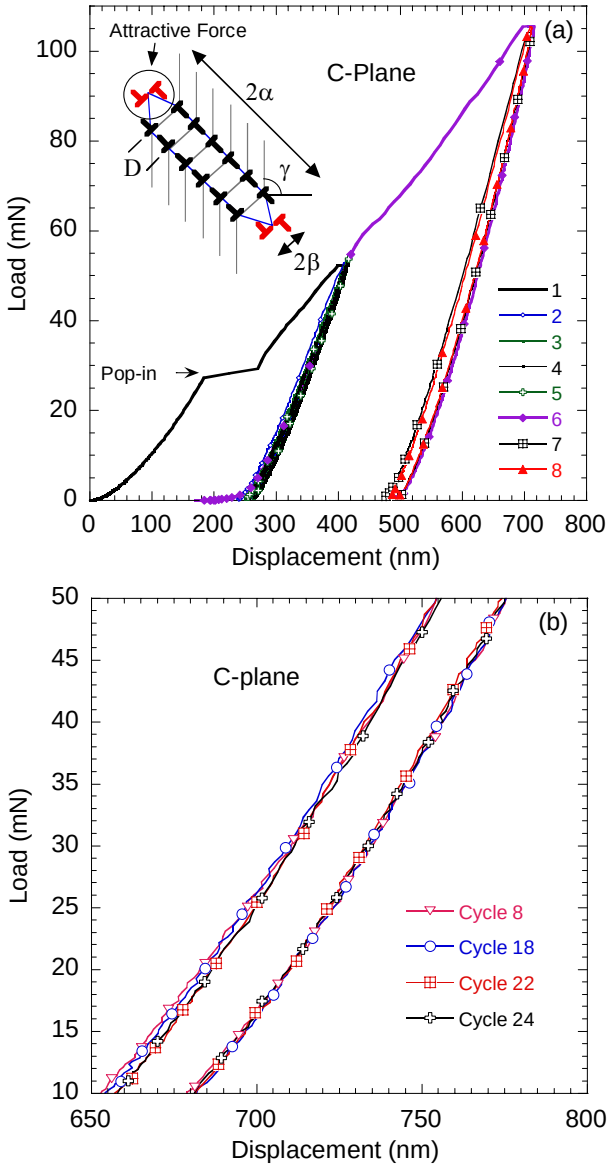

Fig. 7.1 Cyclic nanoindentation results obtained when a 1 μm radius sphere is indented into the same location of a sapphire C (0001) crystal surface. (a) Load-displacement for 5 cycles to 50 mN, followed by 8 cycles at 100 mN. Inset is a schematic of an IKB. (b) Magnified view of the center of select loops for an area indented *24 times* to 100 mN. The reproducibility of the loops is noteworthy. In both a and b only a fraction of the data points collected are plotted.

This load corresponds to a stress of ≈ 44 GPa (Fig. 7.5a). The slope of the inclined dashed line corresponds to an elastic modulus of 381 GPa, calculated from Fig. 7.2, and is little different than 1/s33 (458 GPa) – estimated using the elastic constants reported in

the literature for sapphire.[113] The pop-ins result in a rapid reduction in stress, to ≈ 27 GPa, as the contact area increases suddenly, before it rises again to ≈ 32 GPa.

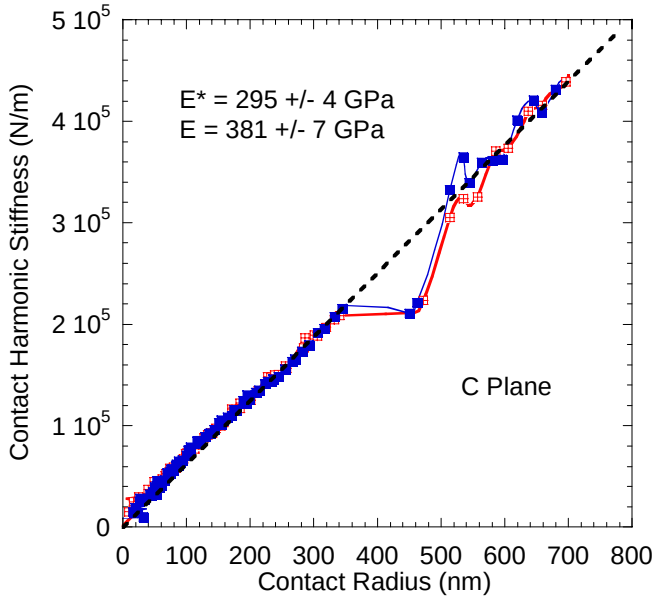

Fig. 7.2 Variation in contact stiffness with contact radius when the C-plane sample was indented with 1 μm indenter.

At this juncture unloading and reloading (cycles 2 to 5) results in fully reversible, reproducible hysteretic loops. The areas enclosed by the loops are quite small, however. In cycle 6 (Fig. 7.1a) the load is increased to 100 mN, which causes the stress to increase to ≈ 40 GPa, before the load is reversed (Fig. 7.5a). Cycles 7 and 8, however, once again, result in fully reversible, reproducible loops; in this case the areas enclosed are clearly visible.

In another experiment, the same procedure was employed except that 24 cycles at 100 mN, in the same location, were carried out. Select cycles are plotted in Fig. 7.1b, with emphasis on the center of the loop. Even at that magnification the reproducibility of cycles 8 to 24 is evident.

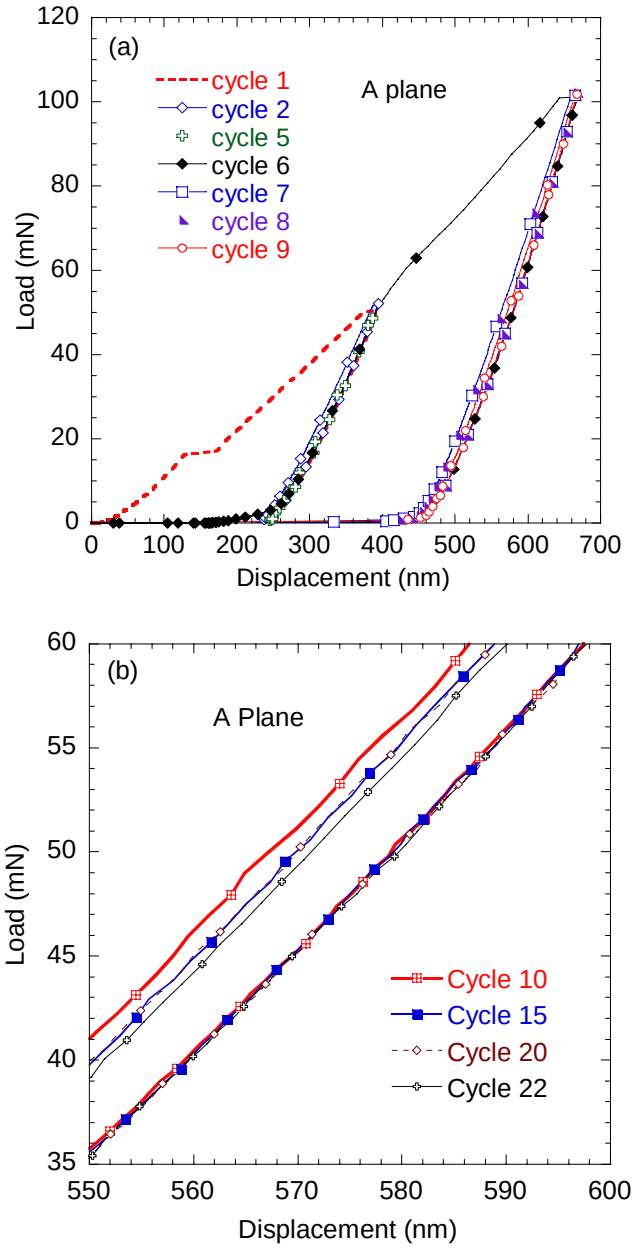

Fig. 7.3 Cyclic nanoindentation results obtained when a 1 μm radius sphere is indented into the same location of a sapphire A crystal surface. (a) Load-displacement for 5 cycles to 50 mN, followed by 8 cycles at 100 mN. (b) Magnified view of the center of select loops for an area indented *22 times* to 100 mN. The reproducibility of the loops is noteworthy. In both a and b only a fraction of the data points collected are plotted.

7.3.2 A-Plane

The response of the A-plane is qualitatively similar to that of the C-plane (Figs. 7.3a and b). A slightly smaller (50 nm) pop-in is observed at ≈ 16 mN. This load corresponds

to a stress of ≈ 44 GPa (Fig. 7.5a). The S vs. a curves are shown in Fig. 7.4. Figure 7.3b plots the central portions of cycles 10, 15, 20 and 22 obtained from another location. Here again it is clear that the later cycles are fully reversible and reproducible.

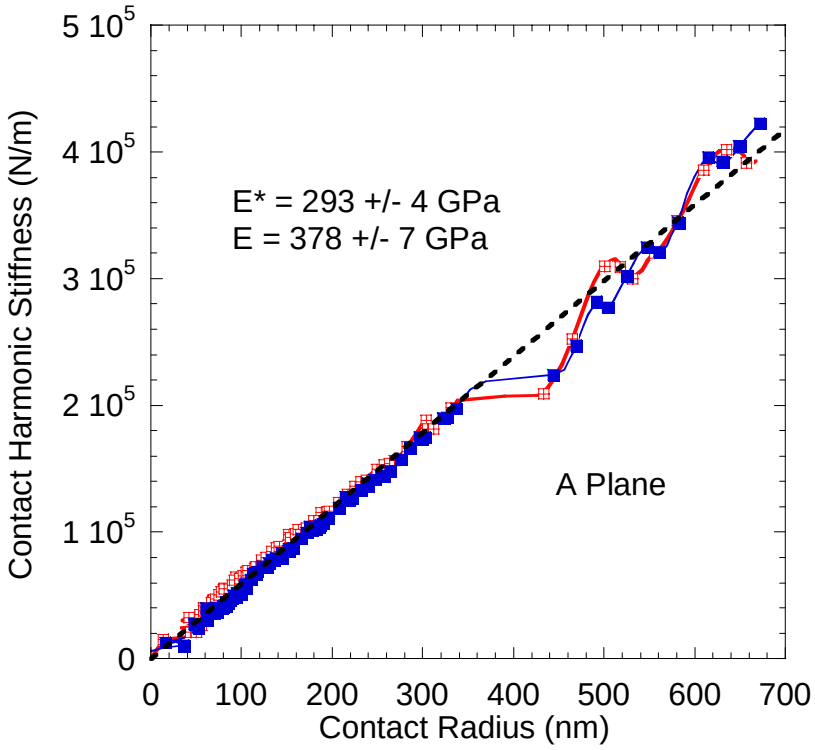

Fig. 7.4 Variation in contact stiffness with contact radius when the A-plane sample was indented with 1 μm indenter.

7.4 Discussion

As discussed in our previous work,[11,12,23] any model put forth to explain the results presented here has to account for the large pop-ins, the fully reversible nature of the loops shown, the cyclic hardening after the pop-ins, as well as the substantial - 0.5 to 1.0 GJ/m^3 - energy dissipated per unit volume per cycle, W_d. Based on the extreme values of W_d (≈ 0.5 GJ/m^3, see below) the reversible nature of the transformation, and our previous work,[12,23,30] there can be little doubt that W_d is due to the to and fro motion of dislocations. The only two other possibilities – fracture or phase transformations – can be

readily ruled out. Fracture cannot lead to hardening and phase transitions have not been reported for sapphire at the stresses reported here.

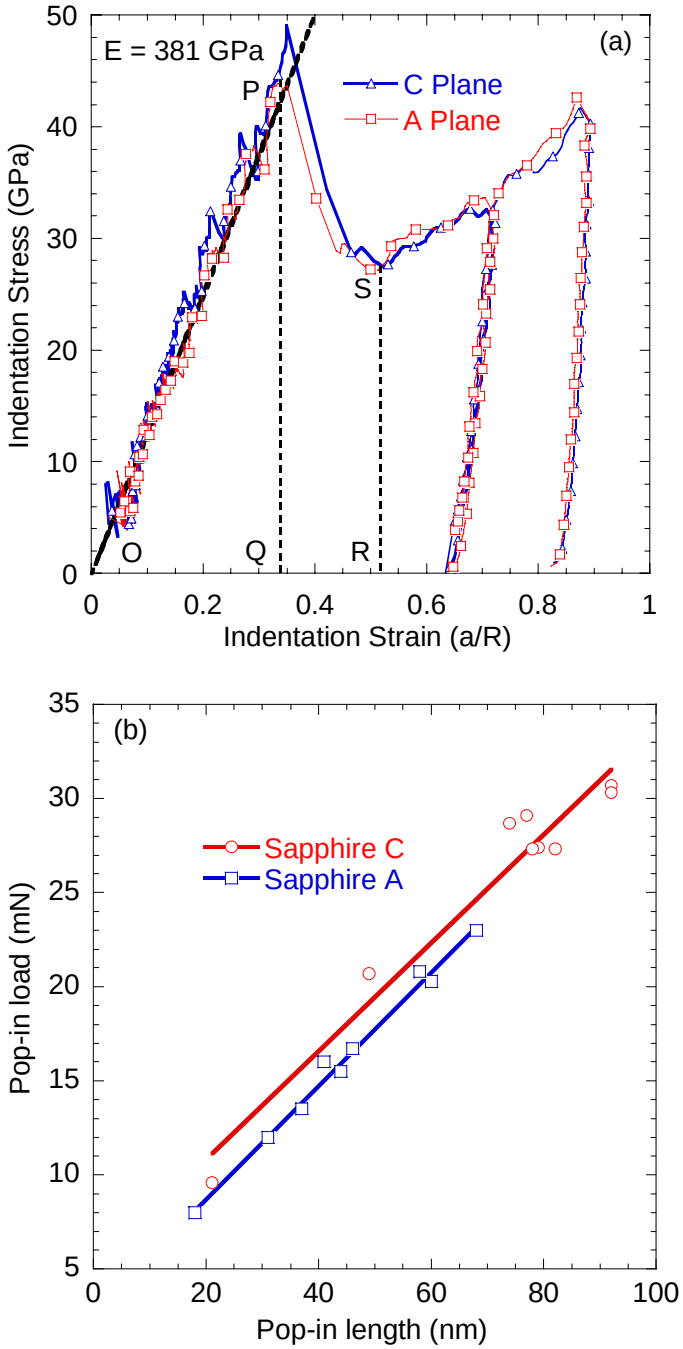

Fig. 7.5 a) Indentation stress-strain curves corresponding to the results shown in Fig. 7.1a (triangles) and 7.3a (squares). Dashed line on left represents elastic response assuming elastic constant is ≈ 500 GPa. Note almost identical response after pop-ins. b) Variation of pop-in load with pop-in length for both orientations. Note the similarity in slope.

Furthermore, the results presented here are in total agreement with, and can be interpreted in the context of, our kink-band based model (Ch. 1).[11,30,31] The pop-ins result in the formation of a large number of mobile dislocation walls, that end up in the kink boundaries.[31] In other words, the majority of the area under the stress-strain curves in the initial cycles is due to the motion of these walls. More importantly, in analogy with graphite[12] and mica,[11] it is reasonable to assume that the massive pop-ins result in the formation of multiple domains – with a size that is smaller than a, the contact radius under the indenter. Upon reloading to 50 mN, presumably the domain size is too small to initiate many IKBs and the response is almost – at higher resolution loops are clear - linear elastic (cycles 2 to 5 in Figs. 7.1a and 7.3a). When in the sixth cycle the load is increased to 100 mN, this presumably results in: i) the formation of more mobile dislocation walls, that again end up in the KBs. This is evidenced by new area under the stress-strain curves and the permanent deformation observed, and, ii) the nucleation of fully reversible IKBs. After a few more re-loadings to 100 mN, an equilibrium microstructure (see below) is reached. Based on the results shown in Fig. 7.1b, cycles 6 and 7 are the ones that are not fully reversible. By the 10th cycle, the response is *fully* reversible, and reproducible. This is best seen in Fig. 7.1b, where it is clear that differences between cycles 8, 18, 22 and 24 are quite small. The very slight decrease in area with increasing cycling is anticipated and is most likely due to the development of an equilibrium microstructure, defined as one where only IKBs are nucleated. In other words, a microstructure where all other dislocations are swept into the KBs and are thus non-reversible.[12,17,18,23,30,48] Similar results were also obtained for the A-plane, where it is clear that cycles 10 and 22 are nearly identical (Fig. 7.3b).

We emphasize again that W_d is substantial and can thus only be due to dislocation motion. It is also remarkable that - despite cycling to a stress of ≈ 40 GPa up to more than 20 times - the loops are as reproducible as they are in Figs. 7.1b and 7.3b. This implies that fatigue, creep, subcritical crack growth, and other time dependent phenomena do not play a role – at least for up to ≈ 20 cycles - despite the ultra high stresses. This results most certainly rules out that the source of W_d is microcracking and/or friction.

An excellent correlation was found between the extent of the pop-ins and the loads at which they occurred (Fig. 7.5b). The variations in pop-in stresses suggest that - like in ZnO[17] and GaN[48] - the initial defect concentrations on and/or near the surface is the rate-limiting factor. The effect of defects, or lack thereof, on pop-in stresses was best illustrated by Nowak et. al.,[104] who implanted Ni^{2+} and Au^{2+} ions into sapphire single crystals and showed that with increasing defect concentrations, the popin stress decreased substantially. This observation is important because it suggests that no plastic deformation is occurring before the pop-in and that the strain energy stored, during the elastic deformation, is almost completely utilized in nucleation and multiplication of dislocations forming kink boundaries. This can also be verified by the fact that the areas OPQ and PQRS in Fig. 7.5a are almost equal – this behavior has also been observed in case of ZnO (Ch. 3), GaN (Ch. 6) and $LiNbO_3$ (Ch. 5) single crystals. This is further bolstered by the excellent linear elastic response – with moduli corresponding to sapphire – obtained in Fig. 7.5a. It is also worth noting that if loaded to loads below the pop-in stresses no trace of the indentations is found in the SEM and/or the AFM.

According to our AFM scans (Fig. 7.6), the pop-ins resulted in impressions with depths that corresponded to the extent of residual penetration, or plastic deformation,

registered in the first cycle. A material pileup was also seen around the impressions; similar pileups have been observed by others.[109,110]

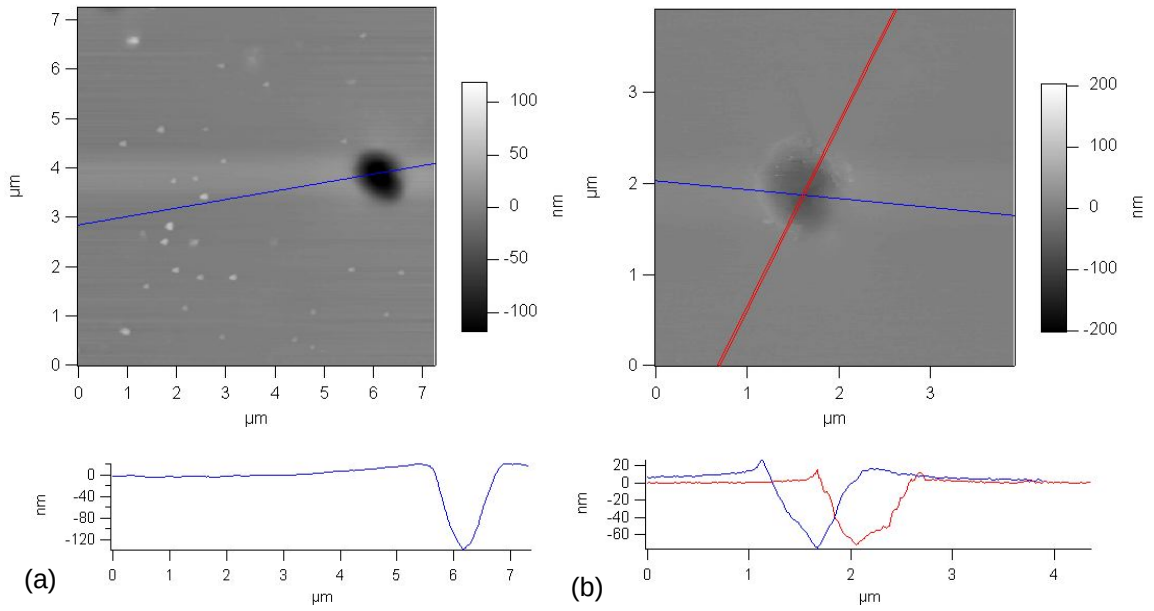

Fig. 7.6 Atomic force microscopy (AFM) scans showing residual displacement after the pop-in and pileup around the indents in a) C-plane; and b) A-plane.

Figure 7.7a shows a typical SEM micrograph of an indentation impression made when the indenter was loaded to 200 mN into the A-plane. Four cracks aligned at roughly 90° emanate from each impression. The cracks and their orientation are almost identical to the ones shown by Nowak et al.[110,112] Furthermore, two sets of near parallel linear features (labeled LF in Fig. 7.7a) are clearly visible. Note that the crater sides at ≈ 90° to the linear features are smooth. Direct evidence of a feature that can result from a kink boundary, but not a twin, is shown in Fig. 7.7b (see below).

The impressions left – after pop-in - on the C-plane were significantly different than those made on the A-plane. In general they were more difficult to find since the craters

were remarkably smooth, especially at lower loads. To help find these indentations, a 3x3 indentation array, using a load of 200 mN, was introduced.

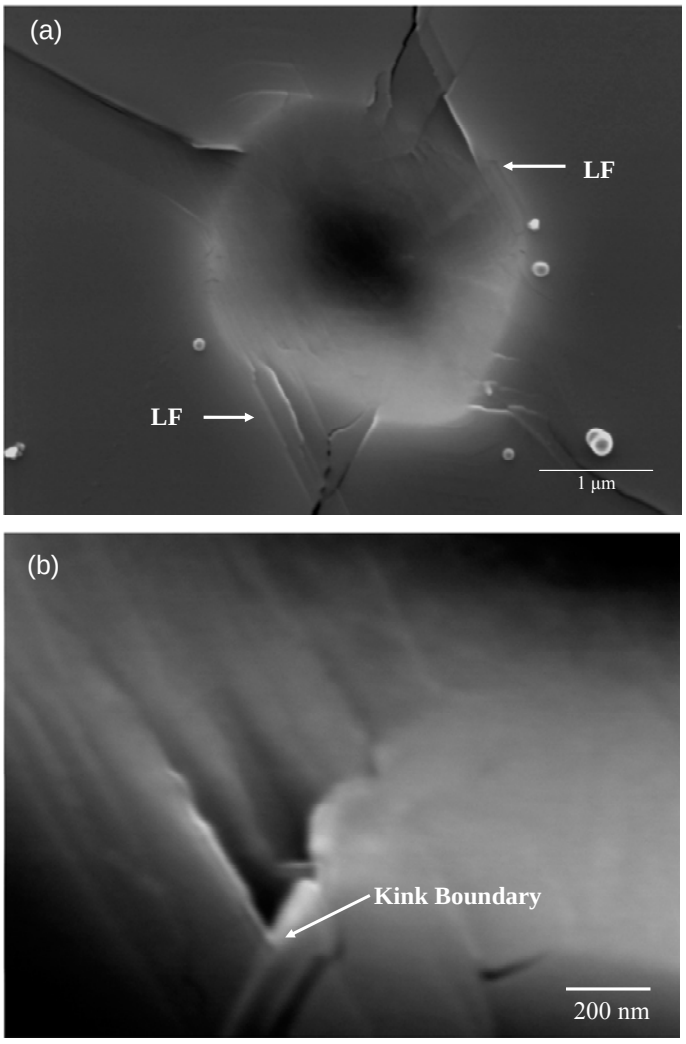

Fig. 7.7 ESEM images of the indented surface of sapphire A surface. (a) The crater after a 200 mN indent. Note the two-fold symmetry of the linear surface features. (b) Surface feature near the edge of a indent that is most likely a kink boundary.

A corner of such an array is shown in Fig. 7.8a. The near proximity of the indentations (~ 5 μm) resulted in substantial damage to the areas between them. In agreement with previous work, no linear features were observed in this direction.[109-111] In analogy with graphite loaded in the same direction,[12] and again in agreement with

previous work on sapphire,[110] the crack pattern exhibits 6-fold symmetry (Fig. 7.8b). At the same time it should be mentioned that there was no such pronounced linear features confirming active pyramidal or prismatic slip as can be seen in case of ZnO while indenting in the C direction.[17]

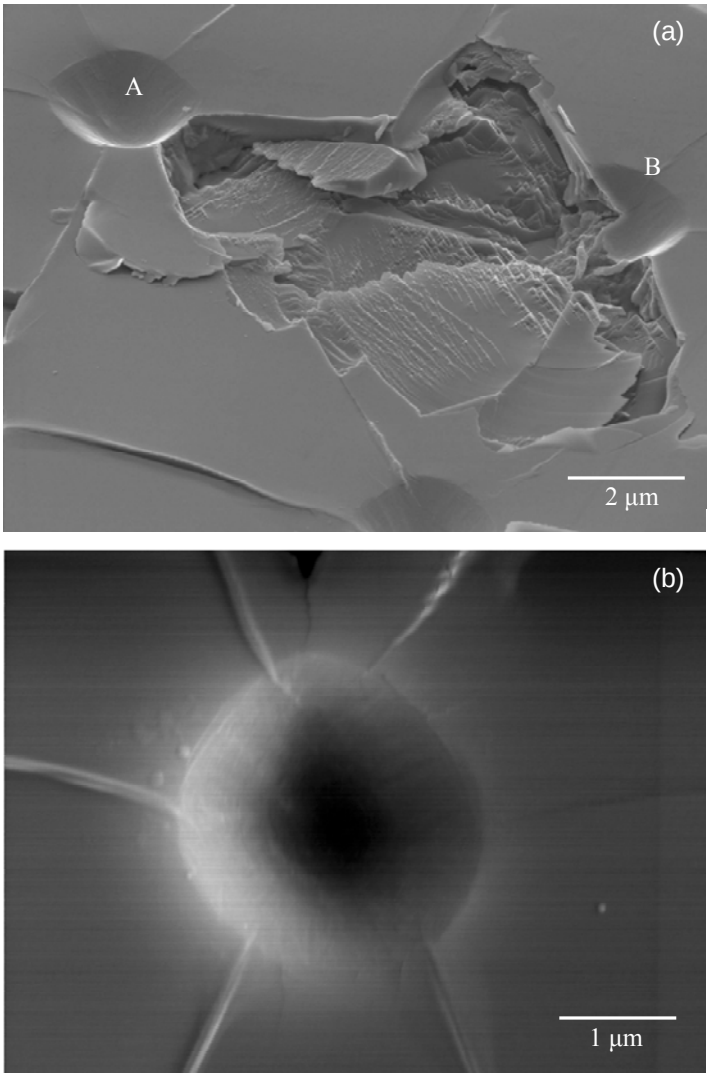

Fig. 7.8 *Continued...*

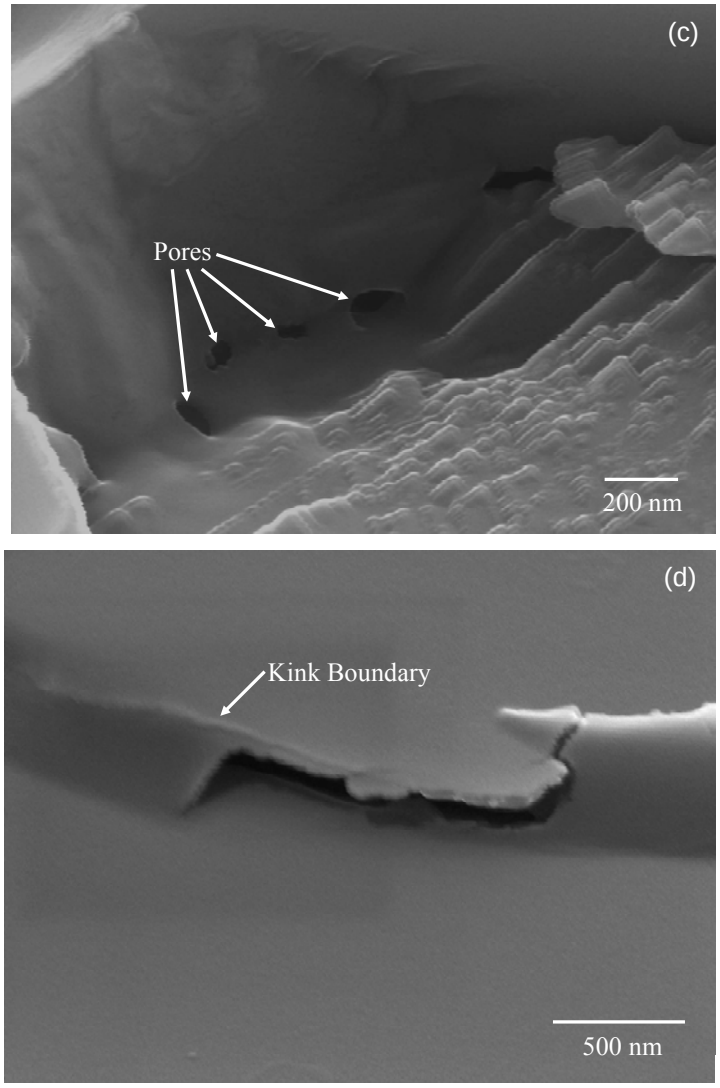

Fig. 7.8 ESEM images of the indented surface of sapphire C crystal. (a) A severely damaged region of a 3x3 array of 200 mN indents. (b) A 200 mN indent. Note the six-fold symmetry around the indentation. (c) Damaged area under the impression labeled A in a. Note presence of regular shaped pores at a distance of ≈ a below the indentation mark. (d) Surface feature near the edge of a 200mN indent that is most likely a kink boundary.

When the region just below the indentation (i.e. indent A in Fig. 7.8a), was imaged its polycrystalline nature is again suggested. Most surprising, however, was the presence of a number of ≈ 100 nm pores (Fig. 7.8c), roughly 500 nm below the indentation impression visible in top left of Fig. 7.8c. The implications of these pores are discussed below.

One of the major assumptions made in this work is that of the formation of small domains below the indenter after the massive pop-ins. In porous Ti_3SiC_2,[114] graphite[12] and mica[11] single crystals, the material under the indenter, after massive pop-ins, was unambiguously transformed into multiple domains wherein the domain size was << a, the contact radius. The results shown in Figs. 7.7 and 7.8 suggest the same is occurring here.

Interpretation of the SEM micrographs shown in Fig. 7.8, are consistent with our kink band-based model. In the case of the C-plane the situation is not unlike the one studied by Molina-Aldareguia et al.[64] who nanoindented epitaxial thin films of Ti_3SiC_2 and imaged the indentations by AFM and their cross-sections by TEM. In this orientation clear unambiguous evidence for the formation of kink bands below the indenter was obtained. Pileups occur without any of the basal planes intersecting the surface; we believe the same is true here, which explains why no surface linear features have ever observed in this orientation.[109,110] Mica basal planes also behave in a similar fashion when loaded parallel to the c-axis (see Fig. 3 in Ref. 11[11]). The nature and cause of the terraces and bumps shown in Figs. 7.8a and c is not clear at this time.

It is important to note that the elastic residual stresses required to maintain the features labeled kink bands in Figs. 7.7b and 7.8d would have to be ≈ 100 GPa. Since this is impossible we conclude that the features must be kink, or high angle, tilt boundaries. In other words, these features are compelling evidence for the formation of *kink boundaries.* Furthermore, Saito et al. have reported on the formation of low angle grain boundaries in sapphire single crystals when the latter were polished at room temperature.[106]

For impressions into the A-planes, however, the situation is different because basal-planes can, and most probably do, intersect the surface. It is that intersection that we

believe gives rise to the linear features documented in the literature.[109] How these features form and what role twinning and/or non-basal slip have in producing them is unclear at this time. It is worth noting here that one of the objectives of a recent study of Tymiak et al.[109] was to try and resolve this question by studying the acoustic emission signal of a spherical nanoindentation since twinning and slip have different AE signatures. For the A and C planes they were not able to discern much of a difference, again consistent with our conclusions. This comment notwithstanding, we concede that how the KBs are created and what role twinning and/or prismatic slip, believed to be the easier slip system at room temperature, are playing remains an open question.

In Fig. 7.5a we plotted a typical indentation stress-strain curve for the C plane alongside that of an A-plane. The similarity of the *post* pop-in curves is remarkable. The almost identical strain hardening rates over a relatively large strain is noteworthy and implies that *after* the pop-ins the microstructures under the indenter are *nearly identical* in every respect. We submit that can only be possible if no trace of the original microstructure is retained after the pop-in. The formation of a very large number of nanodomains (see below) is the simplest and most straightforward explanation. In other words, the response of the sapphire single crystal after the pop-ins is similar to other KNE solids, viz. graphite,[12] mica[11] and Ti_3SiC_2.[114]

At 41±3 GPa the average pop-in stress for the C-plane was quite similar to that of the A-plane; a conclusion reached by Tymiak et al.[109] The areas of the hysteresis loops, however, varied from location to location and were smaller for the A-plane. The averages and standard deviations for and the C and A planes were 0.5±0.1 GJ/m^3, and 0.24±0.06

GJ/m^3, respectively. This type of difference is consistent with our observation in GaN[48] and $LiNbO_3$.[18]

To examine the assumptions of our IKB model - embodied in Eqs. 1.1 to 1.10 - we need to estimate γ_c. From Fig. 7.5a, the threshold stress for the formation of the initial KBs is ≈ 40 GPa. Assuming the shear stress under the indenter is ≈ half the normal stress, it follows that τ_c in Eq. 1.3 is ≈ 20 GPa. c_{44} for sapphire is 148 GPa[113] and consequently, $\tau_c \approx c_{44}/7.5$, which is not unreasonable. Assuming, $G = c_{44} = 148$ GPa, $\nu = 0.25$, and $b = 0.476$ nm, from Eq. 1.3 we calculate γ_c to be ≈ 0.3. In other words, a dislocation is present along the c-axis every ≈ 16 Å. (The c-lattice parameter is 13 Å). Previously[30] we have shown that as the domain size shrinks, $\alpha^3 N_\kappa$ approaches 1. In other word as α decreases, it is unlikely that each domain can sustain more than one IKB. Given that for the C-plane, at 40 GPa, $W_d \approx 0.5$ GJ/m^3 and assuming a threshold shear stress of ≈ 20 GPa (small loops are present at 30 GPa), then according to Eq. 1.9, $\Omega/b \approx 0.8$ GPa. For a threshold stress of 35 GPa, $\Omega/b \approx 1$ GPa. Similarly, for the A-plane, assuming $W_d \approx 0.25$ GJ/m^3, $\Omega/b \approx 0.4$ GPa for a threshold stress of 20 GPa and ≈ 1 GPa for a threshold stress of 35 GPa.

In our previous work it was postulated that Ω/b should be of the order of, if not identical to, the critical resolved shear stress of basal plane dislocations.[30] The room temperature critical resolved shear stress for basal slip in sapphire is estimated to be between 2 and 3 GPa at 227 °C.[115] Therefore our values, while slightly lower than the ones reported in literature, are, given all the assumptions made in obtaining them, quite reasonable and lend credence to both our model and results.

There is a caveat, however. Using the aforementioned assumptions and Eq. 1.2, (assuming w = b) 2α is calculated to be ≈ 37 Å. Given the extreme pressures under the indenter, and the considerable energy dissipated during the first and sixth cycles, this number is not too surprising. At such lengths scales, however, it is more likely than not that the F&S model breaks down since we are dealing with IKBs consisting of a few dislocations each. What we are dealing with is thus quite possibly the formation of dislocation dipoles within the domains.

The transformation - or controlled "explosion" - that occurs under the indenter and the large amounts of energy dissipated in a short period is noteworthy. How the strain energy is transformed to mobile dislocation walls that self-assemble into kink boundaries is not understood at this time and more work is needed to better understand it. A careful transmission electron microscopy study of foils taken from the indentation impressions is called for and should be undertaken. The reason for the presence of pores under the indenter is a true mystery. The simplest explanation is that they existed in the original sample. This is quite unlikely, however, for several reasons. First the pores all appear roughly at a depth ≈ a, i.e. in the region of maximum shear. Second, the samples were transparent; pores are potent scatterers of light. Third, the highly polished surfaces appeared pore free in optical and SEM micrographs. Fourth, a similar set of pores was seen under impression B shown in Fig. 7.5a. It is worth noting that it is not the presence of pores per se that is surprising, but rather the fact that they are well spherodized, the implication being that at some time during their formation atomic mobility was sufficient to cause spherodization. The energy dissipated during the pop-in is substantial (≈ 2.7 to 5.5 GJ/m^3) and it thus conceivable that if the energy released were focused in a small

enough volume, localized melting may occur. This comment notwithstanding we concede the presence of those pores is totally unexpected and not understood.

Lastly we note that the results obtained here strongly buttress our claim that a sufficient requirement for a solid to be KNE is a high c/a ratio, regardless of the type of bonding. Based on our previous work,[30] the critical c/a ratio above which a solid is KNE is ≈ 1.6. With a c/a ratio of 2.73, sapphire is far to the right of this critical ratio and it would thus have been a surprise had it not been a KNE solid.

The implication of the results shown here can be far reaching. If the factors that result in the nucleation of IKBs are identified and manipulated to significantly reduce the stress at which they nucleate it may, in principle, be possible to endow otherwise brittle solids with some limited plasticity; an exciting possibility.

CHAPTER 8: KINKING NONLINEAR ELASTICITY IN MICA STUDIED BY SPHERICAL NANOINDENTATION, AND GEOLOGICAL IMPLICATIONS

8.1 Introduction

The importance of micas, and other layered silicates, in the deformation of geologic formations has long been appreciated.[116-118] These layered minerals are geologically abundant and typically deform by dislocation glide along their basal planes under modest shear stresses, which renders them relatively weak and deformable.[119] It has also long been appreciated that kinking is a favored mode of deformation mechanism in rocks and especially micaceous solids.[118,120-122] Kink bands, KBs, have been observed in micas, at many scales, from the macroscopic, to the transmission electron microscope, TEM, level.[118,122]

Mica belongs to a family of layered compounds that are formed by sheets of negatively charged silicate layers bonded together by interlayer cations, such as sodium or potassium. The interlayer bonding is typically weak compared to the in-plane bonds of the silicate sheets. Consequently, at 61 GPa, c_{33} is roughly 4 times c_{44} at 15 GPa.[123]

On another front, the mechanical response of many rocks – labeled nonlinear mesoscopic elastic (NME) – is known to exhibit nonlinear elastic, hysteretic behavior and discrete memory.[116,117,124] This behavior has been modeled mostly using the Preisach-Mayergoyz space (P-M space) model, that assumes discrete elements of rudimentary

hysteretic mesoscopic units (HMUs).[116,117] The HMUs are modeled as mechanical features, whose equilibrium lengths can switch hysteretically between one of two configurations – open, L_o, or closed, L_c, – at stresses σ_o and σ_c, respectively (Fig. 8.1a). It has been postulated that large numbers of such HMUs, with varying L_o, L_c, σ_o and σ_c values, can model the macroscopic response of these materials. The underlying mechanism of the HMUs, however, had until our recent work not been understood.[11]

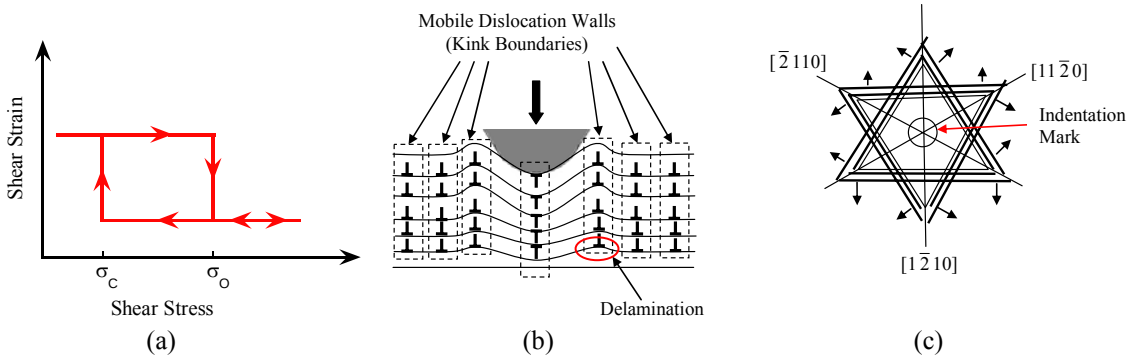

Fig. 8.1. Schematic of, a) phenomenological hysteretic mesoscopic unit (HMU), used to explain the hysteretic behavior in geological materials (*Guyer and Johnson*, 1999; *Guyer et al.*, 1995). b) cross-section of nested MDWs that can form below a spherical indentation. Note the MDWs cannot form without delamination. Once formed the MDWs can move away from the indented region. c) top view of hexagonal, Star of David configuration of MDWs that form and move away from central indentation mark denoted by circle (*Basu and Barsoum*, 2007).

Recently we established a connection between kinking and NME solids. Using mostly cyclic nanoindentation we made the case that incipient kink bands (IKBs), that by definition are fully reversible (see below), are indeed the HMUs invoked to model NME solids.[11] Using cyclic spherical nanoindentation in mica single crystals we showed that KBs play a more important role in the deformation of mica than hitherto been appreciated.[11] When loaded up to 100 mN, the response was characterized by a first loop that was slightly open; all subsequent loops to the same load were fully reversible and

closed.[11] The large amounts of energy dissipation per unit volume per cycle (≈ 80 MJ/m^3 at 3 GPa) were postulated to result from basal plane dislocations – making up the IKBs – sweeping large distances. The presence of basal plane dislocations has been observed earlier by Meike[122] and Kronenberg et al.[120] Not surprisingly, clear evidence of KB formation was obtained from post-indentation scanning electron microscope, SEM, micrographs.[11] As noted above, that mica kinks has been long appreciated; the kinking, however, had only been associated with the fracturing process.[125]

The purpose of this paper is to present further evidence confirming the KNE nature of mica and, more importantly, how different grades, with different defect concentrations, can affect this behavior. We apply our recently developed KNE model to spherical nanoindentation results.[30,43] Also discussed are the implications of our results to geology. Before describing our work, it is important to shortly describe the physics of IKB formation and how we convert nanoindentation, NI, load-displacement curves to NI stress-strain curves.[24]

8.2 Theoretical Considerations

Our recently developed microscale model[30,43] is discussed in Ch. 1 in details. The relevant constants those are needed for calculating different KNE parameters, for Mica, are the following: Burgers vector, b = 5.19 Å; shear modulus, G = 15 GPa (because these are mica single crystals, G is replaced by c_{44}); Poisson's ratio, $\nu = 0.25$; local shear strength, $\tau_{loc} \approx G/30$; and hence the critical shear angle, $\gamma_c = 0.065$ or $\approx 4°$.

A kink boundary is nothing but a low angle grain or tilt boundary. If such a boundary - of length 2α - is subjected to a shear stress, Stroh[126] showed that cleavage in a metal single crystal would occur when:

$$\sigma_n \sigma_s \geq \frac{M\gamma G}{2\alpha\pi}, \tag{8.1}$$

where σ_n is the applied stress, σ_s the resolved shear stress, γ the surface energy of the cleavage planes, and M is a numerical constant of the order of unity, that depends on the elastic anisotropy of the crystal and, as discussed below, the state of stress. This mechanism is particularly suited to solids in which the cleavage and slip planes coincide such as mica.[127] Equation 8.1 is important because it provides a mechanism for the delaminations observed in this work (see below). Note that the IKB to KB transformation *cannot* occur without delamination. Upon delamination, the IKBs are transformed into MDWs that are swept away from under the indenter and end up on the sides of the indenter mark, resulting in a pileup of material around the indentation marks (Fig. 8.1b) and give rise to a Star of David configuration of dislocations (Fig. 8.1c) around the indenter.[16,17,48,53]

In deriving Eq. 8.1,[126] Stroh only considered the situation where the crack grew unstably as a result of tensile stresses, which is why the numerator on the right hand side is essentially Griffith's criteria for brittle failure, i.e. the square of critical stress intensity factor $(K_{1c})^2$. The situation under the indenter, however, is not only more complex, but also highly constrained. These conditions do not alter the physics of the problem, but

simply increase the value of the right hand side. We thus believe Eq. 8.1 is still valid with the understanding that M can now be significantly larger than unity.

The spherical nanoindentation stress, $\frac{P}{\pi a^2}$, and strain, a/R – where P, a and R are the indentation load, contact radius and tip radius, respectively – are calculated from the load-displacement data. The details of the conversion procedure can be found in Ch. 2.[24,54]

8.3 Experimental Procedure

Cyclic NI experiments were carried out on freshly cleaved mica surfaces - that revealed atomically flat basal planes - with a nanoindenter (MTS Nanoindenter XP System, MTS Corporation, Oak Ridge, TN) using a 13.5 μm radius sphero-conical diamond tip and the continuous stiffness measurement (CSM) attachment. The tip radius was calibrated with standard amorphous silica and viewed in a SEM (XL30, FEI Corporation, Hillsboro, OR). The tests were carried out - under load control, at loading rate/load ratio of 0.1 - parallel to the c-axis. All tests were performed only after the instrumental drift was below 0.05 nm/s. A few tests were carried out using a 5 μm spherical indenter tip radius.

Grade A Grade B Grade C

Fig. 8.2. Photographs of three different grades of mica single crystals used in herein. Grades A and B are high quality; grade C, is the most defects, as evidenced from its lack of transparency.

To study the effect of cycling, typically multiple (mostly 5) indentations were carried out on the same location to a given load. In most cases, the first three cycles resulted in permanent residual displacements, while subsequent cycles were characterized by fully reversible hysteretic loops. In many of the repeat cycles a small (< 10 nm) residual deformation was recorded. By careful calibration with silica – which behaves elastically – we confirmed that these residual values were an artifact of the measurement, most probably due to thermal drift. In other words, the third, and subsequent loops are indeed *fully* reversible. As a further check on this important aspect, one sample was indented in the same location 30 times. Within the resolution of our measurements, there were no differences in the areas of the fourth and thirtieth load-displacement loops. To account for this artifact, the *unloading* curves on the fourth and subsequent loadings were forced to coincide with the *unload* curves of the third cycle.[11,12] The corrected or shifted load-displacement curves were then converted to stress-strain curves as described above.

Another indicator that the fourth and subsequent cycles are indeed fully reversible is the excellent reproducibility of these cycles. In materials that cyclically harden, the areas enclosed by the load-displacement loops decrease - and eventually vanish - when the response ultimately becomes linear elastic.[17,24]

Three commercially available natural muscovite single crystals – differing in purity and quality - were studied. The grades are classified here as A, B and C (Fig. 8.2). Mica A was the highest purity grade available; B was a slightly lower grade (both obtained from Ted Pella Inc., Redding, CA, commercially available as grades V1 and V2, respectively). The sheets were approx ~ 150 to 200 μm thick. Grade C mica (Muscovite

from Custer County, SD – Geoprime Earth Materials Co.) had a high defect population evident from its lack of transparency, attributed to defects such as air pockets and delaminations (Fig. 8.2). The grade C sample was a few millimeters thick and was cleaved to expose atomically flat surfaces prior to testing. The post-indent surface features, for all grades, were also observed in a SEM (XL 30, FEI Corporation, Hillsboro, OR).

8.4 Results

From the inception of this work, it was clear that the response depended on grade (Figs. 8.3a and b). For the most part, A grade samples resulted in either a linear elastic response, or fully reversible hysteresis cycles after large pop-ins (see below). The elastic behavior and pop-in stresses of grade B were similar to those of A, but resulted in slightly higher values of W_d. Amongst the 3 grades studied herein, grade C resulted in the largest hysteresis loops and, as important also, exhibited some plastic deformation prior to the pop-ins.

The variability of deformation behavior is clearly evidenced when the pop-in stresses are plotted on a Weibull plot (Fig. 8.3c). The Weibull distributions of A and B are quite comparable; both have Weibull moduli of ≈ 8; at 7±1 GPa, their average pop-in stresses are high. In contradistinction, the pop-in stresses and Weibull moduli for grade C were significantly lower (see dashed line in Fig. 8.3c). The results shown for grade C were taken on different days and on different areas. Interestingly, within a given region, the Weibull moduli are almost as high as those in grades A and B; the difference between the two regions, however, is significant.

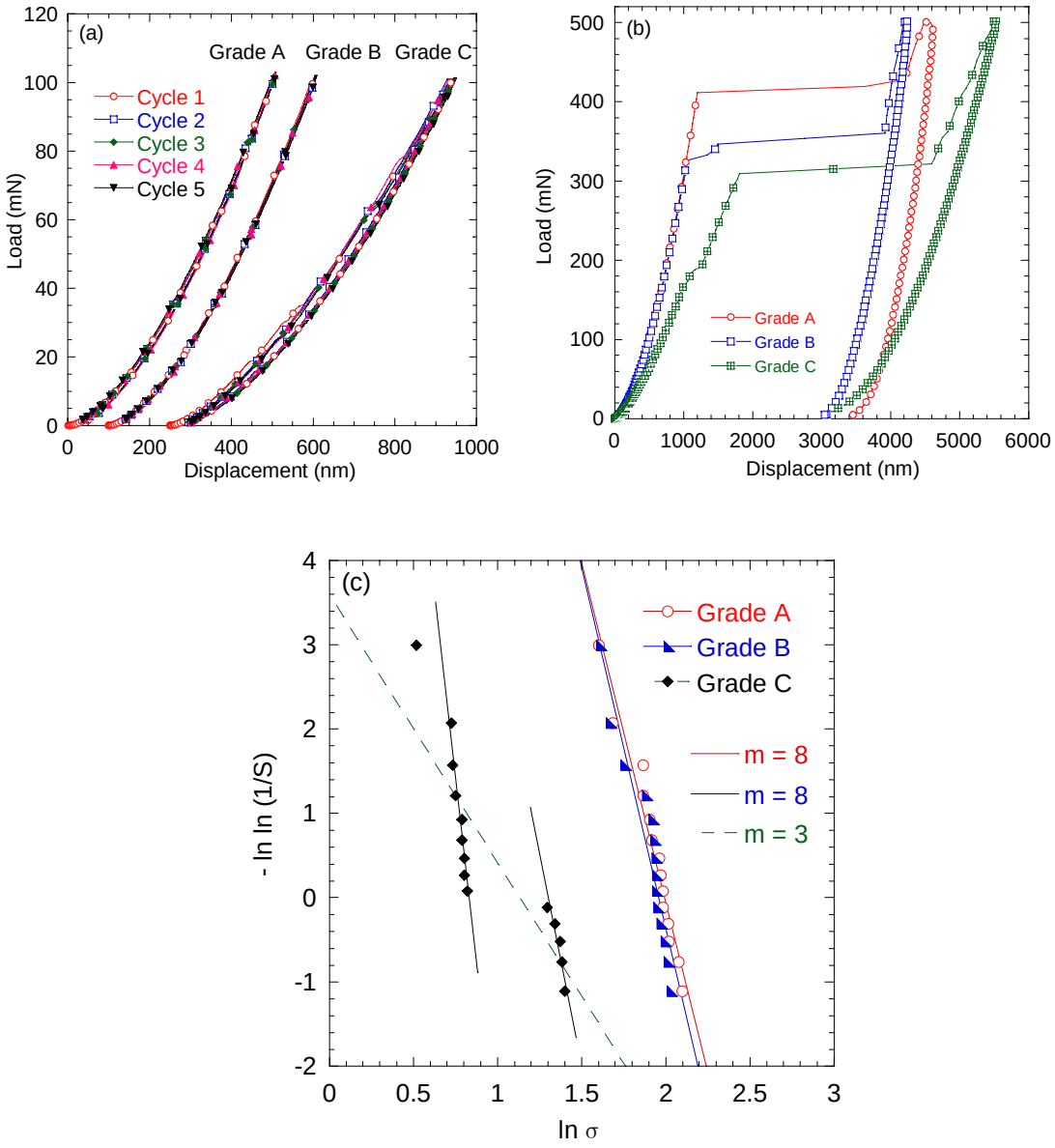

Fig. 8.3. a) Typical load-displacement curves for the three different grades of mica when the surfaces are indented to a load of 100 mN using a 13.5 μm radius indenter. The curves for grades B and C results are shifted to the right by 100 nm and 250 nm, respectively. The response of grades A and B is mostly elastic; grade C, on the other hand, has some small pop-ins during the first cycle and dissipates considerably more energy during the repeat cycles. b) Typical load-displacement curves for the three different grades of mica when the surfaces are indented to a load of 500 mN using a 13.5 μm radius indenter. Note while the behavior of grades A and B are similar, grade C exhibits plastic deformation prior to the pop-in. c) Weibull plots for pop-in stresses for the 3 grades. Grade C exhibited the lowest pop-in stresses and lowest overall Weibull moduli. However, two different regions in grade C resulted in Weibull moduli that were similar to those for grades A and B.

The variation in contact stiffness with contact radii, when the 13.5 μm indenter was loaded up to 500 mN, for grades A, B and C are shown in Fig. 8.4a, b and c, respectively. Grade A and Grade B show good agreement with the linear relationship over the complete deformation range (Ch. 2), indicating an elastic modulus of ~ 61 GPa. In contrast, Grade C samples show the linear agreement only in the initial elastic regime. The reason for this type of behavior is not clear at this moment but most probably it is caused by extensive rotation of the crystal (or, kinked domains) underneath the indenter. Given the variability, each grade is discussed separately below.

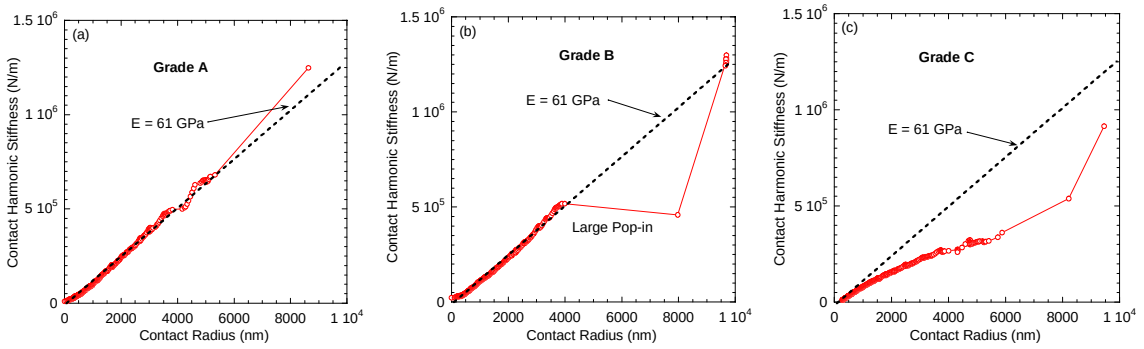

Fig. 8.4. Variation of contact stiffness with contact radii when a 13.5 μm indenter was loaded up to 500 mN on a) Grade A; b) Grade B; and c) Grade C, mica.

8.4.1 Grade A

Cyclic NI load-displacement curves to the maximum load of 500 mN and the corresponding NI stress-strain curves for grade A are shown in Fig. 8.5. Similarly, the load-displacement and NI stress-strain plots to a maximum load of 100 mN are shown in Figs. 8.6a and b, respectively. At least 3 different responses were observed:

A. linear elastic up to the highest load possible, viz. 500 mN, (open squares in Figs. 8.5a and c). When the load-displacement results were converted to stress-strain curves – according to the method mentioned above – the results confirmed the elastic nature of

the indentations prior to the pop-ins, as evidenced by slopes that corresponded to an elastic modulus of 61 GPa (dashed inclined line in Fig. 8.5c); the latter identical to the value of c_{33} reported for mica.[123] This is gratifying because it indirectly confirms the validity of our methodology of converting the NI load-displacement curves to stress-strain curves.

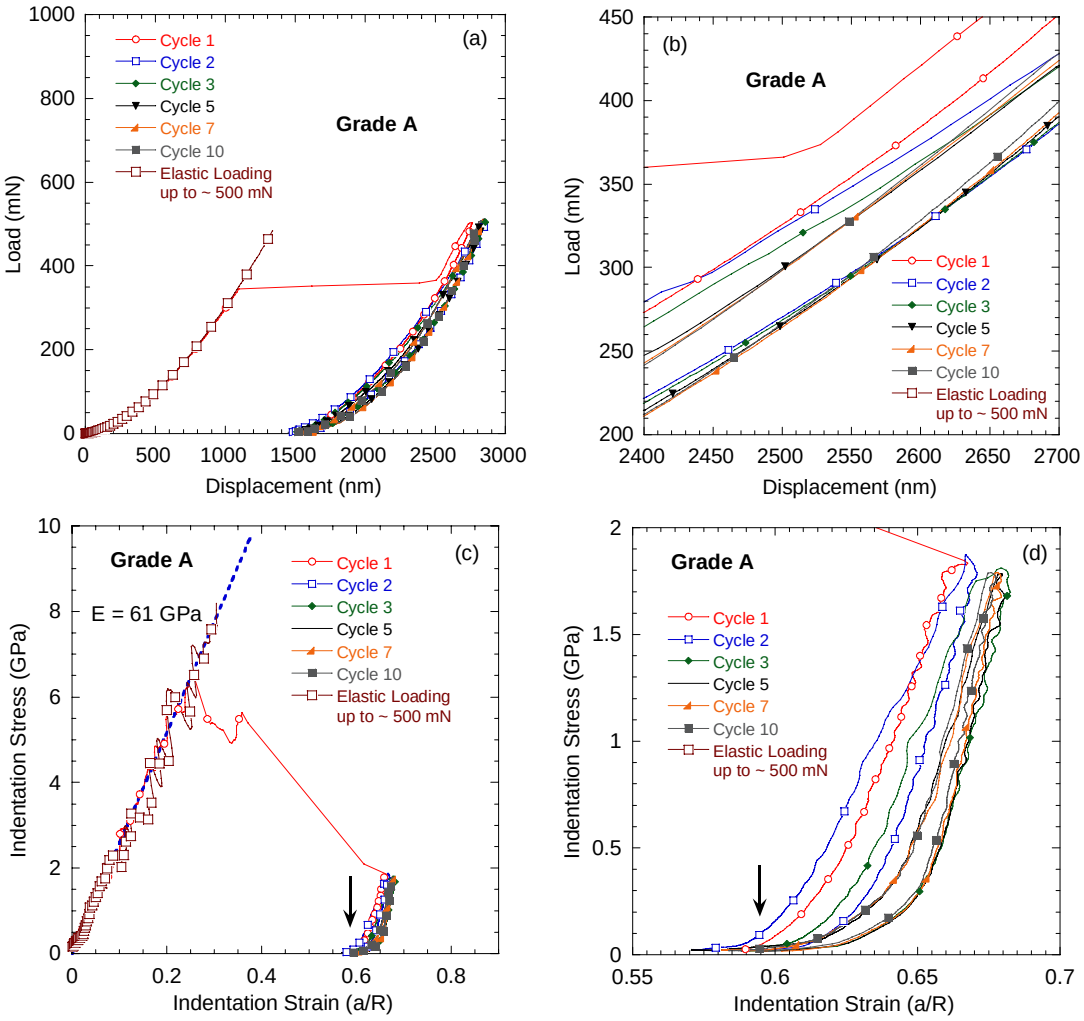

Fig. 8.5. a) Spherical nanoindentation load-displacement response of grade A mica when a 13.5 μm indenter is introduced up to a load of 500 mN. In some locations, large pop-ins were observed, whereas, some locations were elastic up to 500 mN (open squares). b) Magnified view of the deformation during cyclic loading. Note that cycles 5–10 are almost identical and show repeatable hysteretic behavior. c) The corresponding indentation stress-strain curves for the load-displacement data shown in (a). Note linear elastic behavior prior to the pop-ins with a slope that corresponds to a modulus of 61 GPa (dashed inclined line). d) Illustration of the reversible nature of deformation during cyclic loading after the pop-in. The short vertical arrows in (c) and (d) highlight the lower modulus obtained during initial loading after pop-ins.

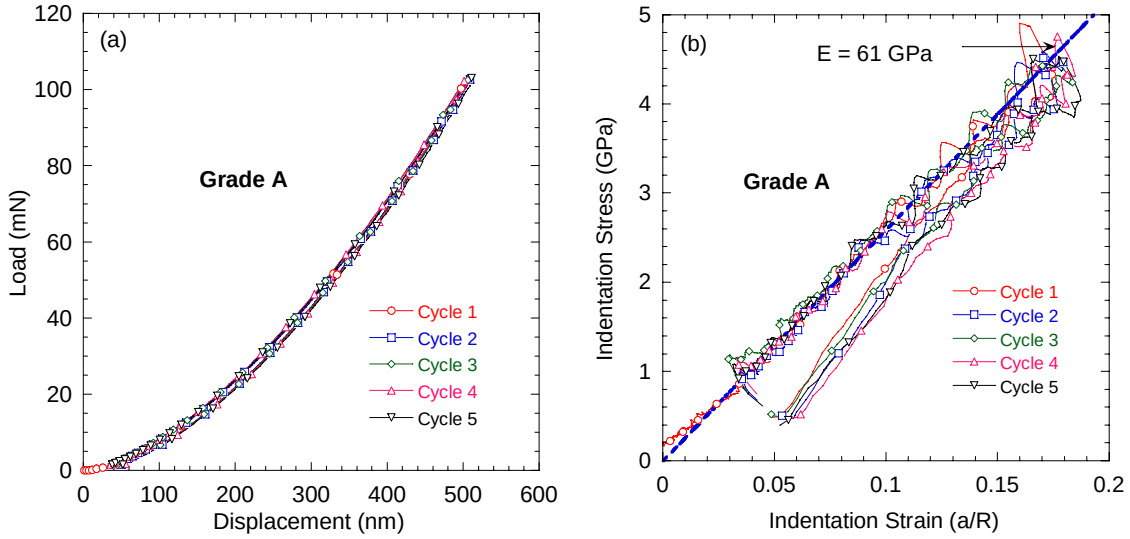

Fig. 8.6. Indentation – a) load-displacement; and b) stress-strain – response when the 13.5 μm indenter was loaded to 100 mN. The linear elastic behavior is represented by the inclined dashed line in (b). Although the deformation is almost elastic for 5 cycles, note reproducible appearance and disappearance of small undulations during loading and unloading, respectively. The residual deformation at the end of each cycle is due to instrumental drift.

B. linear elastic, initially, with a modulus of 61 GPa up to a stress of ≈ 2.5 GPa, after which small undulations are observed, during both loading and unloading (Fig. 8.6). Upon unloading, the undulations disappear, again at a stress of ≈ 2.5 GPa and as important reappear upon reloading. As noted above, the small gap on unloading is an artifact of the experiment.

C. linear elastic, followed by pop-ins of the order of ~ 2 μm during the first loading cycle (Fig. 8.5a); the second and third cycles do not have pop-ins but exhibit some minor plastic deformation. Subsequent cycles are hysteretic, reproducible and *fully* reversible (Fig. 8.5b). More importantly the shapes of the repeat stress-strain curves are quite different from those obtained during the first loading; they change from linear elastic with a modulus of 61 GPa, to one that is concave upwards (denoted by

short vertical arrow in Figs. 8.5c and d). As discussed below this is probably due to the closing of delamination cracks, formed during the pop-ins.

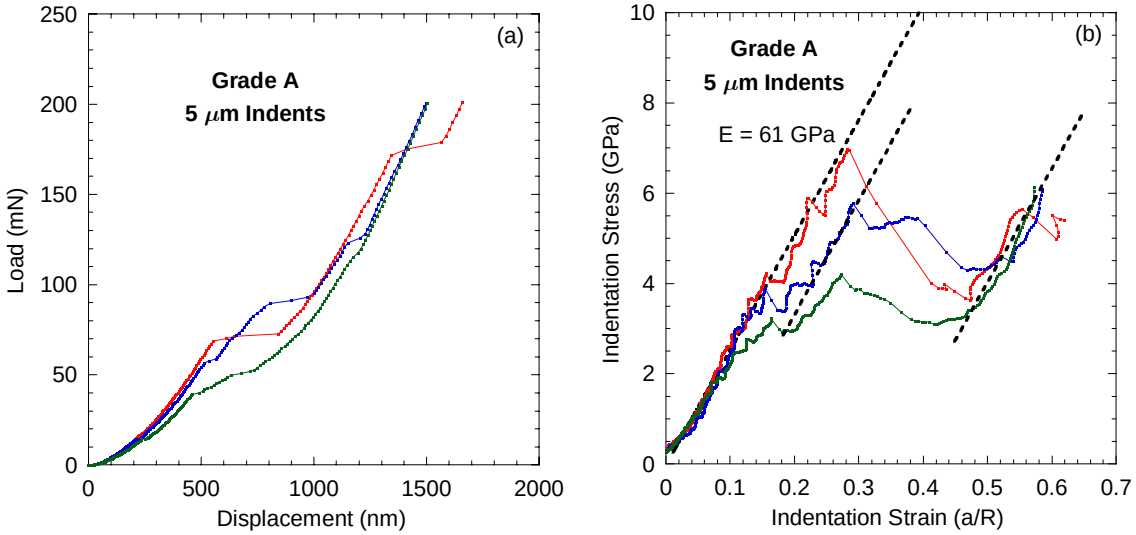

Fig. 8.7. The indentation – a) load-displacement; and b) stress-strain – response, at three different locations, when grade A was indented with a 5 μm indenter to a load of 200 mN. The dashed inclined lines represent linear elastic behavior. Note the elastic nature of deformation even after the large pop-ins.

It is crucial to note here that *only* when loaded to the maximum load possible - 500 mN - and only in some cases, massive pop-ins were observed. In the absence of such massive pop-ins, and despite the fact that the Hertzian stresses at the tip of the indenter were of the order of 8 GPa (Fig. 8.5c) or more, typically *no trace* of the indentations was found in the SEM. In other words, the indentation mark was only observed in the SEM after massive pop-ins.

8.4.2 Grade B

Like the grade A samples, indentations to 500 mN resulted in massive, sudden and irreversible penetrations of the order of 2 μm (Fig. 8.8a). When the results were converted to stress-strain curves, an elastic region, up to about 8 GPa (Fig. 8.8b), was

clearly observed, which was followed by a massive pop-in. Upon reloading, the second cycle showed small amounts of plastic deformation followed by the formation of fully reversible, reproducible loops.

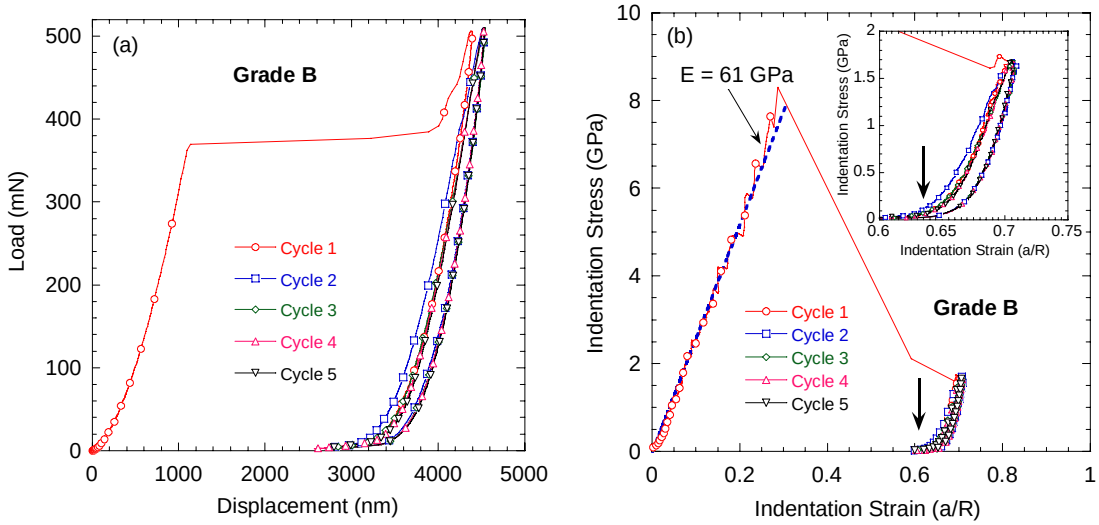

Fig. 8.8. a) Typical load-displacement response of grade B mica when a 13.5 μm indenter was cycled 5 times to 500 mN in the same location. b) Indentation stress-strain curves for the data shown in (a). Dashed inclined line represents a modulus of 61 GPa. Inset illustrates the reversible nature of deformation during cyclic loading after the pop-ins. The short vertical arrows highlight the lower modulus obtained during initial loading after pop-ins.

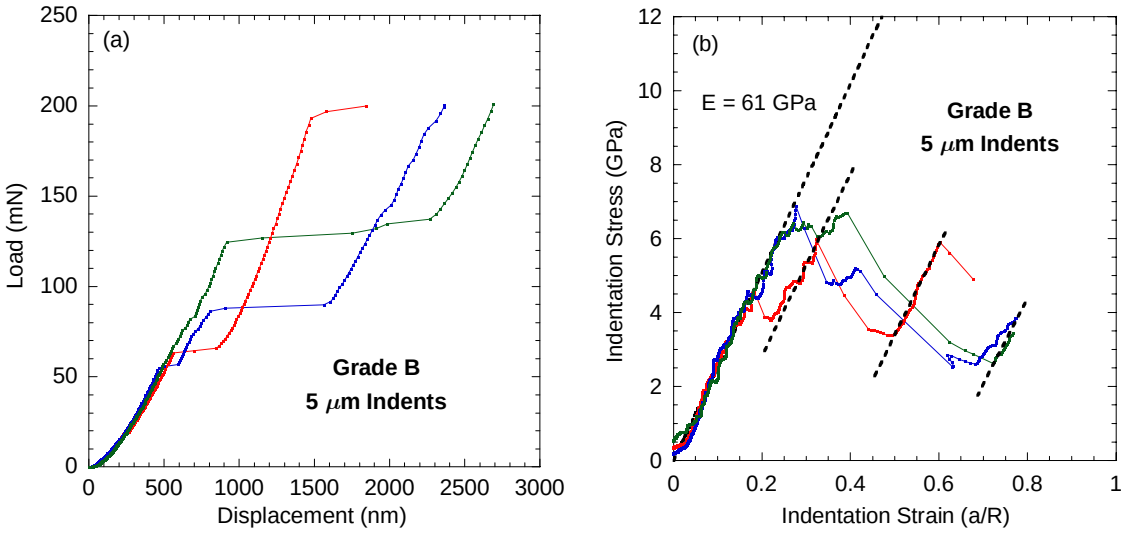

Fig. 8.9. The indentation – a) load-displacement; and b) stress-strain – response, at three different locations, when grade B was indented with a 5 μm indenter to a load of 200 mN. The dashed inclined lines represent linear elastic behavior. Note the elastic nature of deformation even after the large pop-ins.

Interestingly, W_d for the steady-state indentation loops were slightly higher for grade B than for grade A. As observed in grade A, the shape of the stress-stain curves during initial *reloading* in the latter cycles is << 61 GPa, which is, as discussed below, is most probably caused by delamination cracks.

When grade B samples were indented up to 100 mN, the behavior was completely elastic (Fig. 8.3a). The discrepancy with the earlier study[11] – where reversible loops were obtained at that load - is most probably due to the use of a different set of samples, with different defect concentrations.

8.4.3 Grade C

When grade C was loaded to 500 mN, typically one large pop-in followed several smaller pop-ins (denoted by horizontal arrows) during the first cycle (Fig. 8.10a). When the results were converted to stress/strain curves (Fig. 8.10b), like the other grades, the initial slope on loading corresponds to a modulus of 61 GPa. In contrast to the other grades, however, a yield point is observed between ~ 1 and 2 GPa, followed by a region of strain hardening, which is then followed by a massive pop-in event.

When loaded to 100 mN, the cyclic load-displacement curves showed hysteresis loops, unlike other grades (Fig. 8.3a). Despite the absence of large pop-ins, and in contrast to grades A and B, here fully reversible loops were observed after the first cycle (see results labeled 100 mN and shifted by 0.1 towards the right on the strain axis in Fig. 8.10b). Note the elastic regime during reloading.

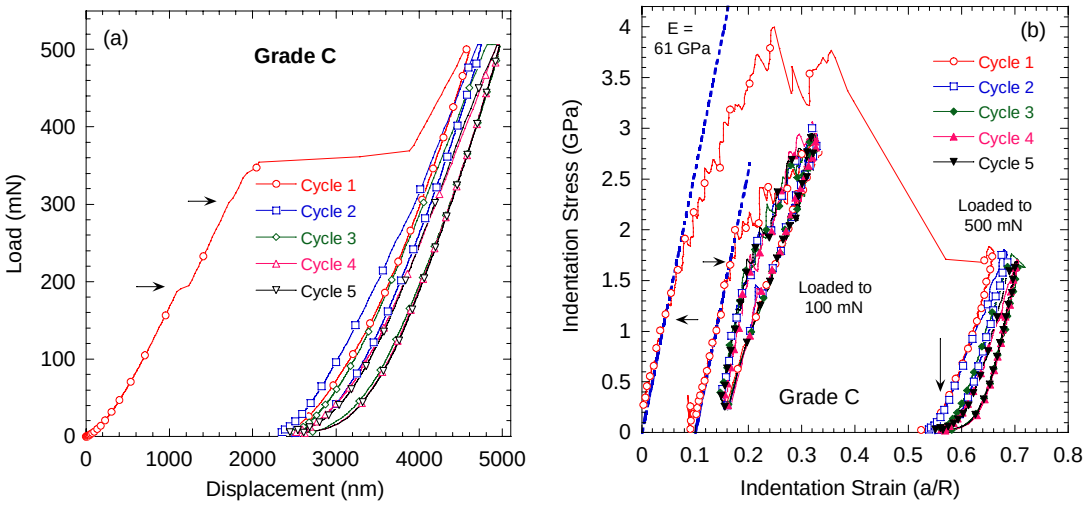

Fig. 8.10. a) Typical spherical nanoindentation load-displacement response for grade C mica, when a 13.5 μm indenter was loaded up to 500 mN. Note the smaller pop-in events (horizontal arrows) prior to the large pop-in and large hysteretic reversible loops during cyclic loading for 5 cycles. b) Indentation stress-strain curves for the data shown in a. Also plotted are the indentation stress-strain curves when grade C loaded up to 100 mN. The latter are shifted by 0.1 to the right for clarity. The dashed inclined lines represent a modulus of 61 GPa. Note, unlike grades A and B, the plastic deformation starts prior to the pop-in (short horizontal arrows). Also important is the fact that in the absence of a pop-in, the initial slope upon reloading is again 61 GPa. The short vertical arrow highlights the much lower slopes of the initial part of the repeat loading after the pop-in.

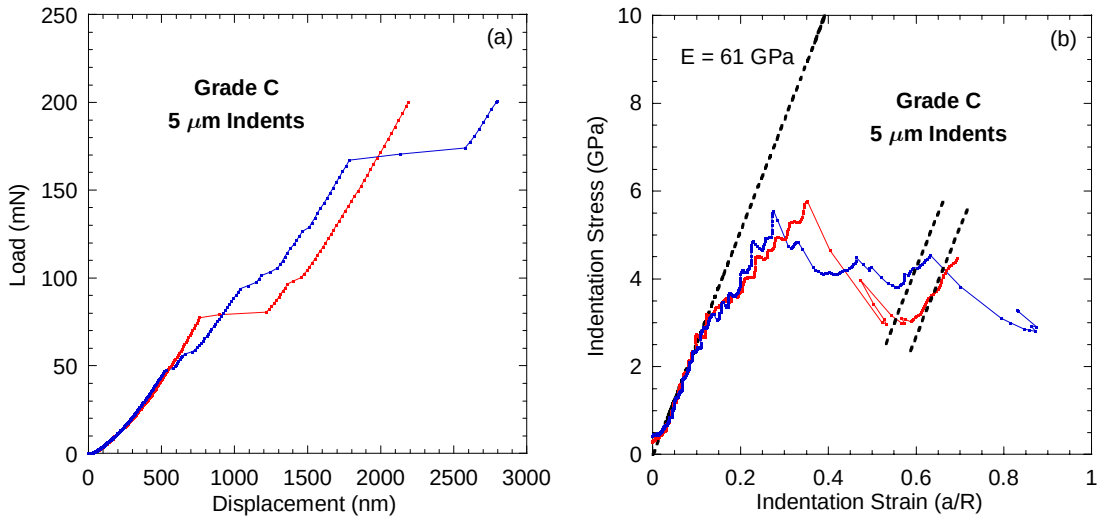

Fig. 8.11. The indentation – a) load-displacement; and b) stress-strain – response, at two different locations, when grade C was indented with a 5 μm indenter to a load of 200 mN. The dashed inclined lines represent linear elastic behavior. Note the elastic nature of deformation even after the large pop-ins.

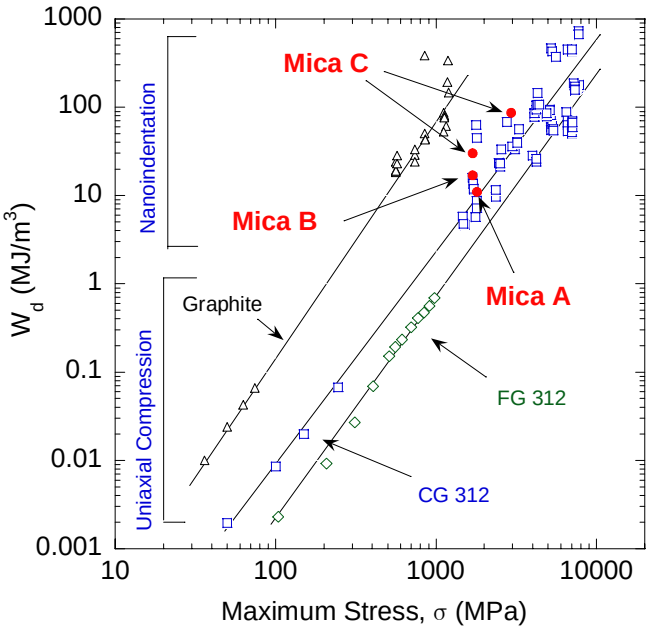

Fig. 8.12. Log-log functional dependence of dissipated energy, W_d, on stress for the 3 grades of mica tested here. Also included are the results for graphite and fine-grained (FG) and coarse-grained (CG) Ti_3SiC_2 obtained from both bulk deformation and spherical nanoindentation (*Barsoum et al.*, 2005b).

To better understand what is occurring during the pop-in events, different locations on all three grades were indented with the sharper 5 μm tip up to a load of 200 mN (Figs. 8.7, 8.9 and 8.11). The resulting stress-strain curves were unlike any others; it is clear in this case that after the massive pop-ins, the response remains linear elastic.

Figure 8.12 is a log-log plot of W_d versus applied stress for the various grades of mica tested here. Also included – in Fig. 8.12 - are the results for Ti_3SiC_2 and graphite for comparison with other KNE solids.[30]

Figure 8.13 shows the surface features and kink band formation surrounding the indents, after loading to 500 mN, in the different grades of mica – A, B and C. In this case, like in sapphire,[16] and for reasons that are not clear, but probably related to the large upheaval around the indenter, and in sharp contrast to graphite,[12] the anticipated 6-fold

symmetry to the indentation mark was not observed. However, the fact that the indents are more or less round (Figs. 8.13a, c and e) is consistent with a 6-fold symmetry.

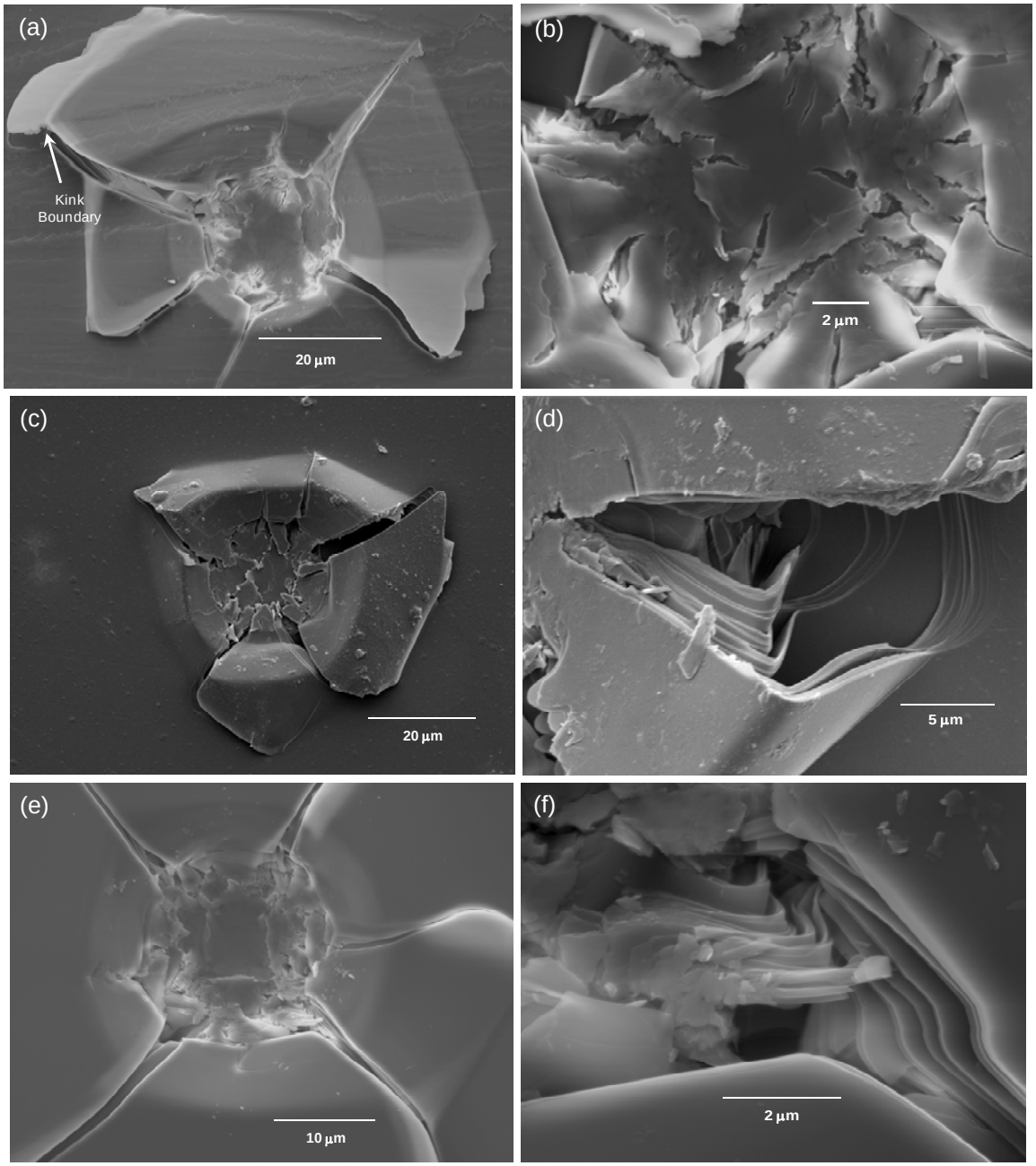

Fig. 8.13. Scanning electron microscope micrographs of indented regions when the 13.5 μm indenter was loaded up to 500 mN into: a) Grade A mica; Note pile-up and kink boundaries around the indented region. b) Magnified picture of the deformation inside the indented region showing extensive delaminations and cracking, that occur during the pop-in event in Grade A. c) Grade B mica; Note again pile-up and extensive cracking around and inside the indent, respectively. d) Magnified image of a kink boundary, formed around the indented region in Grade B. e) Grade C mica; and f) Formation of kink boundaries and extensive rotation of basal planes under the indented region in Grade C.

8.5 Discussion

8.5.1 Indentation stress-strain behavior

The hallmark or defining characteristic of KNE solids is the formation of fully reversible, reproducible stress-strain curves.[11,12,16,17,23,31] Based on that criterion alone, there is little doubt that mica is a KNE solid.[11] The results of this work further confirm this conclusion, as well as, shed more light on the subject. The most important finding of this work, however, and the one that has the most bearing on geology, is the role of defects on the response. The highest quality mica - grade A - is clearly the most immune to kinking; in some cases; even at stresses up to ~ 8 GPa, the response was sometimes linear elastic (e.g. open squares in Figs. 8.5a and c). Similarly, the response of grade B resulted in either fully reversible hysteretic loops, after small pop-ins in the first cycle,[11] or large pop-ins - of the order of 2 μm - at stresses, again, of the order of 8 GPa (Fig. 8.8b).

In contradistinction, the "yield point" of grade C (Fig. 8.10b) is roughly four times lower than the pop-in stresses for A and B (Figs. 8.5c and 8.8b). This is consistent with the fact that grade C, with its high initial defect concentration, either does not need to nucleate dislocations during the first cycle because they are presumably already present, and/or the defects lower the barrier to their nucleation.

Grade C, with the most defects, was not only the one where kinking occurred most readily at the lowest stresses (Fig. 8.10b), but also where the most stochastic response was observed (Fig. 8.3c) - most probably reflecting the distribution of flaws in that material. Two different regions clearly registered quite different pop-in stresses. At this

time the nature of the defects responsible for catalyzing the formation of KBs have not been identified, but as discussed below, delaminations and/or stacking faults are two distinct possibilities. Further TEM in-situ studies are needed to shed light on the mechanisms operating here.

The grade C 100 mN indent results (Fig. 8.10b) - wherein no large pop-ins are registered - are the most readily explainable in the context of our KB-based model. At a yield point of ~ 2 GPa, dislocations, most probably in the form of mobile dislocation walls (MDWs), start moving away from each other, and merge to form permanent KBs, which in turn leads to strain-hardening, observed beyond the yield point in Fig. 8.10b. On reloading, IKBs form, but only in between the kink boundaries formed during the first cycle. A similar response was observed when Ti_3SiC_2 was deformed at higher temperatures, cooled and retested at room temperature.[127] The fact that the slope of the initial part of the stress strain curves during *repeat* cycles agrees with the elastic modulus (~ 61 GPa) is noteworthy and is important evidence that delaminations do *not* play a role in this case (see below).

The results for the 500 mN indents (Figs. 8.5c, 8.8b and 8.10b) can also be explained by our model, by postulating that the pop-ins are caused by delaminations as a result of the tensile stresses generated according to Eq. 8.1. Here, during the pop-in, the response changes from one that is initially elastic, to one that is hysteretic, in which the second and third cycles are slightly open but all subsequent cycles to the same stress level are fully reversible (Figs. 8.5c, 8.8b and 8.10b). As discussed above this sequence of events has been linked to the presence of three interrelated microscopic events. Like in

ZnO,[17] sapphire,[16] and graphite[12] where it has been shown that, during the pop-ins, the elastic energy stored is converted to multitudes of dislocations in the form of MDWs, that, in turn, form KBs. The latter, presumably, leading to the formation of a multiplicity of smaller domains under the indenter. The hysteretic repeatable loops during the repeat cycles are evidence, albeit indirect, that IKBs that form within the smaller domains still play an important role. Direct evidence, however, for the breakdown of what was initially a single crystal is obvious from the SEM micrographs shown in Fig. 8.13. We note in passing that in $LiNbO_3$,[18] during the pop-ins, at least part of the strain energy is converted to twins.

Similar to graphite[12] - but in sharp contrast to non-layered KNE solids, such as ZnO,[17] sapphire,[16] and $LiNbO_3$[18] - here delaminations play an important role. This is best evidenced by the shape of the stress-strain curves upon reloading – concave upwards denoted by short vertical arrows in Figs. 8.5d, 8.8b and 8.10b - during the *initial* parts of the repeat loadings.

Contrast this response to that of the region loaded only to 100 mN in Fig. 8.10b, where presumably no delaminations occurred. Consistent with this view is the paradoxical result that a *higher* stress is actually sustained when the indenter is loaded to 100 mN, rather than to 500 mN during the repeat cycles. This somewhat paradoxical situation is a direct result of the massive pop-ins sustained at 500 mN, and the relatively large craters – thus lower stresses - formed (Fig. 8.13).

Other evidence that delaminations play a role can be seen in Fig. 8.6b, where the small undulations, introduced during loading, appear to heal upon unloading. It is well

established in the ceramics literature that microcracks can heal completely in conditions of high vacuum after the applied stress is removed as the broken bonds can reattach as long as there is no source of contamination or impurities, such as oxygen.[128] Most germane to this work, is the healing observed during cleavage tests on mica under very high vacuum conditions ($< 10^{-8}$ Pa), where cracks were made to advance and retreat, with little loss of energy through successive cycles.[128] Based on this information it is not unreasonable to conclude that the small undulations, or pop-ins, are associated with delaminations underneath the indenter that, because they are not exposed to the atmosphere, heal upon removal of the load. The excellent reproducibility of the stress-strain curves (Fig. 8.6b), where many of the fine features are faithfully reproduced from cycle to cycle is consistent with such an interpretation. Note that, at lower stresses, the undulations disappear, only to reappear at higher stresses.

Figures 8.7, 8.9 and 8.11 also clearly demonstrate the formation of delaminations during the pop-in events, when indented with a 5 μm indenter tip. Here multiple pop-in events occur successively, interspersed by regions of pure *elastic* response. Note that in all cases, the pileup of material around the indentation simply *cannot* occur without the rupturing of the basal planes, as well as the creation of the radial cracks observed (Fig. 8.13). Consistent with this interpretation is the fact that these multiple pop-in events were much more common with the "sharper" - i.e. 5 μm radius - of the two indenters. Note that the origin of the tensile stresses acting parallel to the basal planes that cause their rupture, must be elastic and generated from the local curvature of the basal planes as they are pushed into the bulk.

Delaminations are inherent to the IKB to KB transformation; without them, all the lamellae would be expected to fracture, which is clearly not the case here (Fig. 8.13). Note that basal plane dislocation arrays[121] are also inherent to the overall process; without them, the various lamellae could not shear relative to each other, the precursor for all that follows.[28,37]

8.5.2 Energy dissipation per cycle

Because of the high stresses possible under the indenter, W_d is not insignificant - it is of the order of ≈ 10 to 90 MJ/m^3 (Fig. 8.12). As noted above, from Fig. 8.12 it is evident that grade C dissipates the most energy as compared to the other grades – even more so in the *absence* of a pop-in, where W_d was ≈ 90 MJ/m^3. As a check on these values, we note that when the area enclosed by the load/displacement curves is divided by a^3 – assuming the latter is of the order of the volume affected by the indenter – a value of ≈ 67 MJ/m^3 is obtained indirectly confirming the slightly higher values of 90 MJ/m^3.

To verify our model, the following calculations were carried out. First, the threshold stress for IKB formation/motion was estimated to be 1.4±0.1 GPa from the yield point of the repeat cycles (viz. from Fig. 8.10b). Using this value in Eq. 1.2, the domain size 2α was estimated to be ~ 16 nm. Although the number is relatively small considering the size of the indent, it is reasonable considering the fact that, presumably, the initial defect concentration, or the number of IKB nucleation sites, is quite high.

According to our model, the high value of W_d can partially be attributable to the high value – 80 MPa - of the CRSS of the basal planes. The latter, or more accurately, $\frac{\Omega}{b}$ was

estimated based on Eq. 1.9 assuming $N_k\alpha^3 = 1$, and the 100 mN results on grade C (Fig. 8.10b). The assumption that $N_k\alpha^3 = 1$, is a reasonable one based on the number of IKBs per domain, a result that we have verified in previous work.[18] A CRSS of 80 MPa however, is higher than what one would obtain for mica tested in uniaxial compression tests for example. The reason for this high value is not understood, but is likely due to the normal component of the applied stress. And while it is generally accepted that normal stresses do not greatly affect CRSS's, it is not unreasonable to assume that the extremely high values developed here, and the geometry of the indenter relative the motion of the IKB dislocations under it, influences the CRSS. Solid solution effects cannot be neglected either at this time.

Recent *ab initio* and molecular dynamics calculations[44] have shown that dislocations in perfect metal crystals nucleate when:

$$\tau_{max} \approx \sigma/2 = G/n\,, \tag{8.2}$$

where τ_{max} and σ are the applied shear and normal contact stresses under the indenter, respectively. For polycrystalline metals n is $\approx$ 30.[45,46] In this work the appropriate modulus is not G, but c_{44}, which for mica is 15 GPa.[123] In other words, based on this work, and the fact that in some cases IKBs did *not* nucleate even at a $\sigma \approx 8$ GPa implies that for grade A, n is closer to 4 than 30. A conclusion consistent with recent results obtained in sapphire[16] and ZnO[17] single crystals, where n was $\approx$ 7.5 and 8, respectively.

In general, it is not easy to experimentally determine n. The fact that this value is close to the theoretical strength of a crystal and can be readily measured here is one of

several advantages of using spherical indenters and converting the results to stress-strain curves. This becomes more relevant as we have shown that, for ZnO single crystals,[17] the energy dissipated during the pop-in is roughly equal to the elastic strain energy stored before the pop-in. In other words, most of the elastic strain energy was used to nucleate dislocations. This comment notwithstanding, more work is ongoing and needed to understand the dislocation nucleation process during the massive pop-in events commonly observed when spherical, rather than sharp, nanoindenters are used.

The fact that dislocations in mica are confined to the basal planes[120,122] allows the dislocation loops to extend over relatively large distances, i.e. large values of 2β, which could partially explain the large values of W_d (Eq. 1.9). Note the glide of dislocations on different slip systems cannot explain this phenomenon; were the dislocations allowed to entangle the process would not be reversible.[118,120,122]

Typical SEM micrographs of post-indentation craters formed after the massive penetrations of the indenter (at 500 mN load) in different grades of mica are shown in Fig. 8.13. Examination of Fig. 8.13 reveals the segmentation of single crystal into multiple domains – a key component in our model - with some large cracks emanating from its center. The deformation induced segmentation of grains, is similar to that reported by Bell and Wilson in biotites,[118] and is almost identical to the microdomains observed in indented graphite single crystals after massive pop-ins.[12] Clear evidence for the formation of kink boundaries in the pileups around the indented region can be seen in all three grades. The massive rotation of some of the lattice planes (Fig. 8.13e) is unambiguous and striking in its severity. Similar rotations have been observed in recent

work on Cu single crystals subjected to spherical nanoindenters.[129] Similar features were also observed in Ti_3SiC_2, and other ternary machinable carbide and nitride phases at all length scales.[28,29,32,36,37,130]

8.5.3 Implications to geology

A relationship between NI and geology may seem farfetched. But as we pointed out in our previous paper on the subject,[11] since the deformation under an indenter is constrained it is possible to reach much higher stresses - and thus better mimic geologic conditions - than would normally be possible. Furthermore, the fact that the relationship between σ and W_d (Fig. 8.12) is apparently valid for over six orders of magnitude, demonstrates the predictive capability of our model to higher stresses with reasonable certainty.

The relevance of the results presented herein to geology cannot be overemphasized. The most profound implication has to do with the energy stored in a formation and its relationship to, i) its deformation history and, ii) the quality of the mica, or any other layered silicate, that it is comprised of. Clearly the areas under the stress-strain curves shown herein are quite different. It is fair to argue that such variations would be reflected in the response of any such formation to stresses. Needless to add, these facts complicate our understanding and analysis of the deformation of rocks containing these phases. This is probably one of the reasons for the huge variability in responses of various types of micas that have been observed.[119]

Second the confirmation that IKBs are the origin of the hysteretic mesoscopic units (HMU) in NME solids should lead to a much deeper understanding of the nature of

deformation in geological formations. This is especially true since micaceous materials form a major portion of the Earth's surface and a better understanding of their deformation behavior can potentially have a major influence on designing structures for minimal damage due to earthquakes.[117]

Third, with the knowledge of KNE deformation in micaceous solids and layered minerals, the elastic and damping properties, measured by ultrasound, can be analyzed in terms of residual stress and deformation history. Along the same lines, a solid under stress, with a high density of KB's, will have innumerable dislocation loops that in turn will respond to a perturbation, such as ultrasound, quite differently than the same rock with a different density of KB's. For example, the damping of Ti_3SiC_2, at room temperature and without stress, as measured by ultrasound is not exceptional.[131] However, a small deformation at high temperatures increases the damping by an order of magnitude.[132,133]

Given our understanding of dislocations, the cross-fertilization that will ensue, together with the large amount of work already existing on geological materials, some of which may have to be reinterpreted, should yield to quantum jumps in our understanding of their deformation behavior, damping and ultrasound characteristics.

8.6 Summary and Conclusions

The results of this work demonstrate the power of spherical NI, in furthering our understanding of the deformation mechanisms of geologically relevant solids. The advantage of probing small amounts of materials at geologically relevant stresses, should lead to rapid advancement in our understanding of deformation in geological formations.

This is especially true when the load displacement curves are converted to NI stress-strain curves. Such curves clearly demonstrate the effect of initial defect concentrations in mica single crystals on their mechanical response. The higher the defect concentration, the lower the stresses necessary for nucleation and/or growth of IKBs. As important the response of the mica is markedly different before and after the pop-ins, implying that the thermo-mechanical history is also an important consideration when trying to understand the deformation of such micas.

The high stresses generated under the indenter allow us to explore the response of such solids under geologically relevant conditions, simply rapidly and reproducibly. Clearly more work is needed, especially in relating the response of mica under a nanoindenter, to the response of a geologic formation made of the same material. It is our sincere hope that this work will inspire others to explore this important question, especially given the relative simplicity of the technique and the wealth of information obtainable.

CHAPTER 9: SUMMARY, CONCLUSIONS AND FUTURE WORK

9.1 Summary

9.1.1 Summary of Elastic Moduli

This section summarizes the elastic moduli values, for the hexagonal crystals studied herein, measured by spherical nanoindentation (E_{sph}), Berkovich nanoindentation (E_{Br}) and theoretical values calculated ($1/S_{33}$ or $1/S_{11}$, for C and A orientations, respectively) from reported elastic constants.

Table 9.1. Summary of elastic moduli values determined from spherical nanoindentation, Berkovich nanoindentation and theoretical elastic constants

Material	Orientation	E_{sph} (GPa)			E_{Br} (GPa)	$1/S_{33}$ or $1/S_{11}$ (GPa)
		1 μm	5 μm	13.5 μm		
ZnO	C	131±4	128±2	130±4	135±3	149 [57]
	A	121±3	126±3	128±6	144±4	128 [57]
$LiNbO_3$	C	184±4	184±6	186±2	200±2	199 [82]
	A	180±3	-	190±3	234±5	173 [82]
GaN	C	297±15	-	212±9	261±3	328 [57]
	A	284±6	-	196±5	255±3	226 [57]
Sapphire	C	381±7	-	361±6	412±8	458 [113]
	A	378±7	-	-	-	429 [113]

It is evident from Table 9.1 that the theoretical moduli values are reasonably close to the values calculated from spherical and Berkovich nanoindentation. This comment

notwithstanding, it should be noted here that the stress-states under a nanoindenter is more complex than a simple uniaxial experiment – hence, the moduli values computed from indentation experiment should not exactly match with the theoretically determined numbers. Also, with the exception of 1 μm indents in GaN, E_{sph} is lower than E_{Br}. Further studies are underway to better understand the relationship between E_{sph}, E_{Br} and the theoretical values.

9.1.2 Summary of Hardness

This section summarizes the hardness values obtained by Berkovich nanoindentation, H_{Br}, and Vickers microhardness indentation, H_V, on ZnO, $LiNbO_3$, GaN and sapphire single crystals. The values for fused silica are also shown in Table 9.2, for comparison. As shown in previous chapters (Chs. 3, 5, 6 and 7), it is difficult to define a particular hardness value for spherical nanoindentation, because often it exhibits strain hardening.

Table 9.2. Hardness values as measured by Berkovich nanoindentation and Vickers microindentation

Material	**Orientation**	**H_{Br} (GPa)**	**H_V (GPa)**
ZnO	C	4.8±0.1	3.3±0.1
	A	2.7±0.1	1.7±0.1
$LiNbO_3$	C	9.3±0.1	4.5±0.2
	A	12.6±0.2	5.7±0.2
GaN	C	15.2±0.1	10.9±0.1
	A	13.2±0.2	9.9±0.3
Sapphire	C	25±1	22.5‡
	A	-	
Fused Silica	-	9.3±0.2	5.6±0.6

‡ According to manufacturer

To examine if there is any correlation between H_{Br}, H_v, and the strain hardening rates observed for spherical nanoindentation, the latter is plotted against the difference of H_{Br}

and H_V (Fig. 9.1). Also plotted in this figure are the values for single crystals of TiO_2 (001), MgO (111), Si, and polycrystalline Fe and Al. Although the value for sapphire is shown in the figure, it is acknowledged that the hardening rate is probably incorrect because the deformation was already beyond the spherical limit of the 1 μm indenter (see Ch. 7).

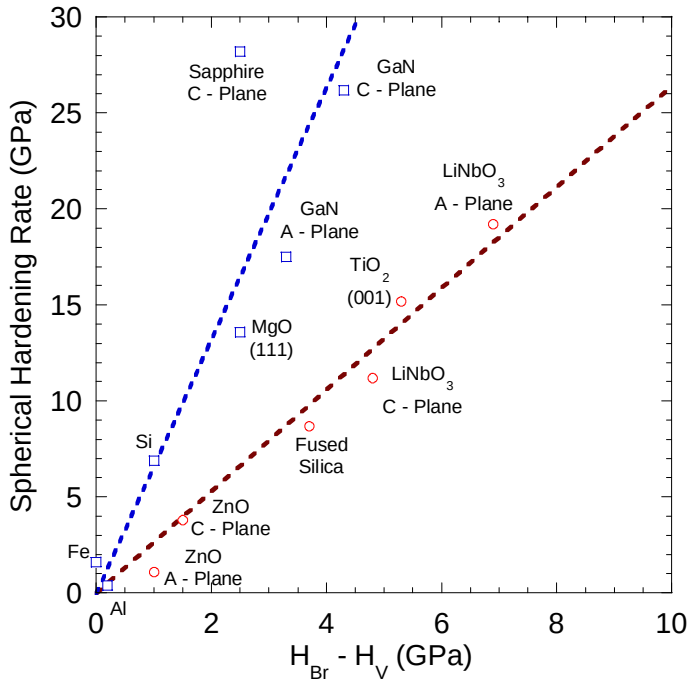

Fig. 9.1 Relationship between hardening rate in spherical nanoindentation and the difference between Berkovich and Vickers hardness.

It should be acknowledged here that, for the first time, Fig. 9.1 shows some kind of relationship between spherical nanoindentation, Berkovich nanoindentation and Vickers microindentation, although the exact nature of the relationship is not clear. More systematic work is in progress to understand this relationship.

9.1.3 Summary of Hysteretic Behavior under Spherical Nanoindentation

It has been discussed in earlier chapters that the C-orientation of the hexagonal crystals, studied herein, show fully-reversible hysteretic behavior during cyclic loading under spherical nanoindenter.[16-18,48,134] This section summarizes the experimentally determined parameters related to reversible hysteretic behavior in the C-orientation of the hexagonal crystals. Table 9.3 lists the crystals with their corresponding c/a ratio, C_{44}, and W_d, as determined from the spherical nanoindentation stress-strain curves discussed in previous chapters.

Table 9.3. List of c/a ratio, C_{44}, energy dissipated per unit volume per cycle, and maximum stress, during cyclic spherical nanoindentation in the C-orientation of the hexagonal single crystals (except, Ti_2AlC and Ti_2SC – which were polycrystalline)

Material	**c/a**	**C_{44} (GPa)**	**W_d (MJ/m^3)**	**Maximum Stress, σ_{max} (GPa)**
ZnO 13.5 μm	1.6	45	18	3.1
$LiNbO_3$ 13.5 μm	2.69	59.5	204	5.4
$LiNbO_3$ 5 μm			157	5.4
$LiNbO_3$ 1 μm			233	9.2
GaN 1 μm	1.63	241	20	25.3
Sapphire 1 μm	2.73	148	500	40
Mica (C-grade) 13.5 μm	1.4	15	90	3
Ti_2AlC 13.5 μm	4.47	119	31	2.8
Ti_2SC 13.5 μm	3.49	125	99	8

After calculating the above mentioned parameters, we try to find a possible relationship between the crystal structure (c/a ratio), the shear modulus (G, or C_{44}), and the hysteretic behavior under spherical nanoindentation. In light of Eq. 1.9, we can define a parameter, $\frac{W_d C_{44}^2}{\sigma_{max}^2}$, which takes into account only theoretical and experimentally determined values. Figure 9.2 results when this parameter is plotted against the c/a ratio, and the slope is most probably proportional to the domain size, α (Eq. 1.9), for the reversible hysteretic behavior.

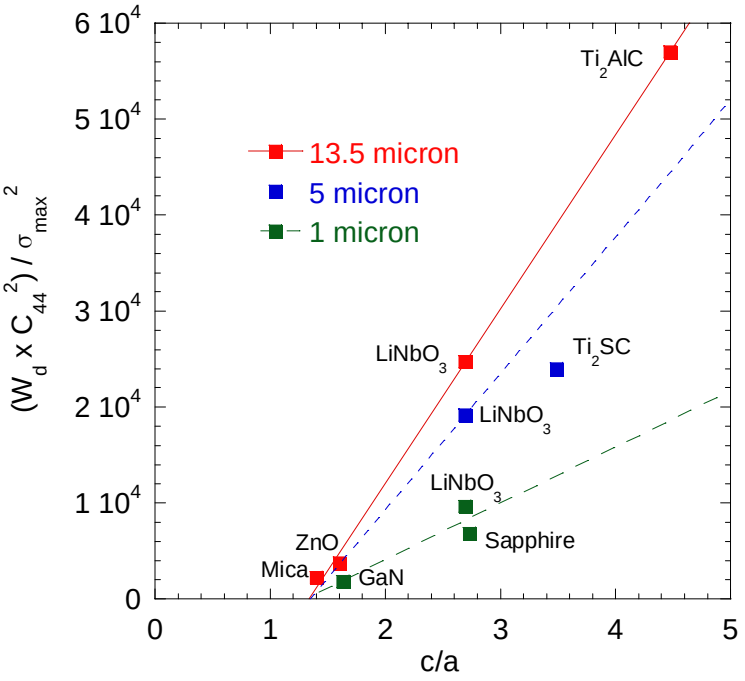

Fig. 9.2 Relationship of energy dissipation, per unit volume per cycle during cyclic spherical nanoindentation, with the c/a ratio of hexagonal crystals. Note that the magnitude of the slope depends on the tip size, which eventually determines the domain size for dislocation based fully-reversible behavior.

First, the slopes for different indenter sizes in Fig. 9.2 clearly show that the domain size is governed by the size of the indenter for a wide range of c/a ratio. Second, it is also

evident that the fully reversible deformation behavior is mostly dominant in hexagonal crystals, because all the lines intercept the x-axis at ~ 1.4.

Figure 9.2 is very important for better understanding of the reversible hysteretic behavior in single crystals under spherical nanoindentation, more specifically for hexagonal crystal structures. To check the validity of this plot, we added the result of 13.5 μm indents on polycrystalline Ti_2SC. The reason it does not fall on the same line as other 13.5 m indents is its small grain size of 2 – 4 μm. This is consistent with our work on KNE solids, where we showed that the domain size in polycrystalline materials is limited by the grain size.[30,31] Hence, Fig. 9.2 is very important in terms of predicting the reversible hysteresis in hexagonal solids if the domain size is known, and vice versa. It is also important in moving forward from single crystal results to polycrystalline materials, as demonstrated by the data on Ti_2SC.

9.2 Conclusions

1. Spherical nanoindentation is a powerful and important tool for studying micro/nano-scale elastic-plastic deformation behavior in materials; more so for brittle ceramics, where bulk uniaxial compression/tension experiments are not possible.

2. A detailed procedure is outlined, during this work, to convert spherical nanoindentation data into representative indentation stress-strain curves.[24] Besides providing more quantitative information about yield point, hardening rate and nonlinearity, the indentation stress-strain curves were used to compare between different orientations of materials and different indenter sizes – the information, which is not intuitive from a load-displacement curve.

3. Although more research is needed, there is almost a linear relationship between the spherical nanoindentation strain hardening rates and the hardness values measured from Vickers microhardness and Berkovich nanoindentation.

4. Stress-strain curves from cyclic spherical nanoindentation are very informative regarding dislocation based reversible hysteretic behavior in solids.

5. The micro-scale model is successful in defining different parameters in dislocation-based kink bands and the relationships between them. The experimental data from cyclic stress-strain curves, from both bulk and spherical nanoindentation experiments, match extremely well with the model, and hence the deformation behavior due to incipient kink bands (IKBs).[18,30]

6. The micro-mechanisms of deformation in hexagonal single crystals and KNE parameters, computed from the micro-scale model, matches with the microstructural features that formed under the indenter.[18]

7. The combination of the spherical nanoindentation results from the single crystals of hexagonal ceramics confirms the fully reversible, hysteretic behavior for high c/a (> ~ 1.4) materials – which, for the most part, is due to the dislocation-based IKBs. The combined picture (Fig. 9.2) also enhances the possibility to transfer the knowledge from deformation in single crystals to polycrystalline materials.

8. Calculation of representative indentation stress and strain enabled us, for the first time, to control these parameters, in real time, during indentation experiments. The

power of this novel technique is successfully demonstrated by the constant-stress creep in ZnO single crystals, studied herein (Ch. 4).

9.3 Future Work

As discussed in the previous chapters, we want to point out some interesting and important research directions, which will give us better understanding of the deformation under spherical nanoindenter in general, and kinking nonlinear elastic behavior in particular.

1. Validation of the definition of indentation strain by theoretical modeling and finite element simulations. This will be important for obtaining better representative indentation stress-strain curves for different materials.

2. Spherical nanoindentation experiments at elevated/lower temperatures. It will be important for studying the activation energy of dislocation nucleation and propagation in materials.

3. Controlled stress or strain indentation experiments to study creep, fatigue, and slow critical crack growth in materials, specially for brittle solids. These new experimental methods will also have the advantage of comparing the results with bulk experiments and determining the scaling factors in the deformation behavior.

4. Systematic cyclic spherical nanoindentation study of reversible hysteretic behavior in polycrystalline materials, with small grain sizes, in light of Fig. 9.2. It will be very informative for fabricating micro-devices with controlled damping properties.

5. It is also important to extend the proposed microscale model to incorporate effects of grain orientation and grain size distribution.

6. Systematic in-situ TEM experiments to visualize the dislocation structures forming during indentation and, if possible, the IKBs.

7. Systematic in-situ measurements of other functional properties (e.g. electrical, magnetic, optical) during indentation to study how different dislocation structures affect the functional behavior of the materials.

LIST OF REFERENCES

1. Doerner, M. F. & Nix, W. D. A method for interpreting the data from depth-sensing indentation instruments. *J. Mater. Res.* **1**, 601-609 (1986).

2. Oliver, W. C. & Pharr, G. M. Measurement of hardness and elastic modulus by instrumented indentation: Advances in understanding and refinements to methodology. *J. Mater. Res.* **19**, 3-20 (2004).

3. Field, J. S. & Swain, M. V. Determining The Mechanical-Properties Of Small Volumes Of Material From Submicrometer Spherical Indentations. *Journal Of Materials Research* **10**, 101-112 (1995).

4. Fischer-Cripps, A. C. A review of analysis methods for sub-micron indentation testing. *Vacuum* **58**, 569-585 (2000).

5. Fischer-Cripps, A. C. Critical review of analysis and interpretation of nanoindentation test data. *Surface and Coating Tech.* **200**, 4153-4165 (2006).

6. Field, J. S. & Swain, M. V. A Simple Predictive Model For Spherical Indentation. *Journal Of Materials Research* **8**, 297-306 (1993).

7. *High Pressure Surface Science and Engineering* (eds. Gogotsi, Y. & Domnich, V.) (Institute of Physics, Bristol, UK, 2003).

8. Galanov, B. A., Domnich, V. & Gogotsi, Y. Elastic-plastic contact mechanics of indentations accounting for phase transformations. *Exp. Mech.* **43**, 303-308 (2003).

9. Juliano, T., Gogotsi, Y. & Domnich, V. Effect of indentation unloading conditions on phase transformation induced events in silicon. *J. Mater. Res.* **18**, 1192-1201 (2003).

10. Iwashita, N., Swain, M. V., Field, J. S., Ohta, N. & Bitoh, S. Elasto-plastic deformation of glass-like carbons heat-treated at different temperatures. *Carbon* **39**, 1525-1532 (2001).

11. Barsoum, M. W., Murugaiah, A., Kalidindi, S. R. & Zhen, T. Kinking Nonlinear Elastic Solids, Nanoindentations and Geology. *Phys. Rev. Lett.* **92**, 255508-1 (2004).

12. Barsoum, M. W., Murugaiah, A., Kalidindi, S. R. & Gogotsi, Y. Kink Bands, Nonlinear Elasticity and Nanoindentations in Graphite. *Carbon* **42**, 1435-1445 (2004).

13. Murugaiah, A. in *Department of Materials Science and Engineering* (Drexel University Philadelphia, 2004).

14. Tabor, D. *Hardness of Metals* (Clarendon, Oxford, U.K., 1951).

15. Brinell, J. A. in *II. Cong. Int. Methodes d'Essai* (Paris, 1900).

16. Basu, S., Barsoum, M. W. & Kalidindi, S. R. Sapphire: A Kinking Nonlinear Elastic Solid. *J. Appl. Phys.* **99**, 063501 (2006).

17. Basu, S. & Barsoum, M. W. Deformation Micromechanisms of ZnO Single Crystals as Determined From Spherical Nanoindentation Stress-Strain Curves. *J. Mater. Res.* **22**, 2470-2477 (2007).

18. Basu, S., Zhou, A. & Barsoum, M. W. Reversible dislocation motion under contact loading in $LiNbO_3$ single crystal. *J. Mater. Res.* **23**, 1334-1338 (2008).

19. Iwashita, N., Field, J. S. & Swain, M. V. Indentation Hysteresis of Glassy Carbon Materials. *Phil. Mag. A* **82**, 1873-1881 (2002).

20. Herbert, E. G., Pharr, G. M., Oliver, W. C., Lucas, B. N. & Hay, J. L. On the Measurement of stress-strain curves by spherical indentation. *Thin Solid Films* **398-399**, 331-335 (2001).

21. Kucheyev, S. O., Bradby, J. E., Williams, J. S., Jagadish, C. & Swain, M. V. Mechanical deformation of single-crystal ZnO. *App. Phys. Lett* **80**, 956-958 (2002).

22. Bradby, J. E., Williams, J. S. & Swain, M. V. Pop-in events induced by spherical indentation in compound semiconductors. *J. Mater. Res.* **19**, 380-386 (2004).

23. Murugaiah, A., Barsoum, M. W., Kalidindi, S. R. & Zhen, T. Spherical Nanoindentations in Ti_3SiC_2. *J. Mater. Res.* **19**, 1139-1148 (2004).

24. Basu, S., Moseson, A. & Barsoum, M. W. On the determination of spherical nanoindentation stress strain curves. *J. Mater. Res.* **21**, 2628-2637 (2006).

25. Johnson, K. M., Manuszak, J. D. & Johnson, A. M. How kink bands work and how to work with kink bands. *Dept. of Earth and Atm. Sc., Purdue University* (2002).

26. Orowan, E. A Type of Plastic Deformation New In Metals. *Nature* **149**, 463-464 (1942).

27. Frank, F. C. & Stroh, A. N. On the Theory of Kinking. *Proc. Phys. Soc.* **65**, 811-821 (1952).

28. Barsoum, M. W., Farber, L., El-Raghy, T. & Levin, I. Dislocations, Kink Bands and Room Temperature Plasticity of Ti_3SiC_2. *Met. Mater. Trans.* **30A**, 1727-1738 (1999).

29. Farber, L., Levin, I. & Barsoum, M. W. HRTEM Study of a Low-Angle Boundary in Plastically Deformed Ti3SiC2. *Phil. Mag. Letters,* **79**, 163 (1999).

30. Barsoum, M. W., Zhen, T., Zhou, A., Basu, S. & Kalidindi, S. R. Microscale Modeling of Kinking Nonlinear Elastic Solids. *Phys. Rev. B.* **71**, 134101 (2005).

31. Barsoum, M. W., Zhen, T., Kalidindi, S. R., Radovic, M. & Murugahiah, A. Fully Reversible, Dislocation-Based Compressive Deformation of Ti_3SiC_2 to 1 GPa. *Nature Materials* **2**, 107-111 (2003).

32. Barsoum, M. W. The MN+1AXN Phases: a New Class of Solids; Thermodynamically Stable Nanolaminates. *Prog. Solid State Chem* **28**, 201-281 (2000).

33. Barsoum, M. W. & El-Raghy, T. Synthesis and Characterization of a Remarkable Ceramic: Ti_3SiC_2. *J. Amer. Cer. Soc.* **79**, 1953-56 (1996).

34. Barsoum, M. W. & El-Raghy, T. The MAX phases: unique new carbide and nitride materials. *American Scientist* **89**, 336-345 (2000).

35. Barsoum, M. W., Ali, M. & El-Raghy, T. Processing and characterization of Ti_2AlC, Ti_2AlCN and $Ti_2AlC_{0.5}N_{0.5}$. *Met Mater Trans* **31A**, 1857-65 (2000).

36. Barsoum, M. W., Brodkin, D. & El-Raghy, T. Layered Machinable Ceramics For High Temperature Applications. *Scrip. Met. et. Mater.* **36**, 535-541 (1997).

37. Barsoum, M. W. & El-Raghy, T. Room Temperature Ductile Carbides. *Metallurgical and Materials Trans.* **30A**, 363-369 (1999).

38. Jeitschko, W. & Nowotny, H. Die Kristallstructur von Ti_3SiC_2 - Ein Neuer Komplxcarbid-Typ. *Monatsh. fur Chem.,* **98** 329-37 (1967).

39. Pampuch, P., Lis, J., Stobierski, L. & Tymkiewicz, M. Solid Combustion Synthesis of Ti_3SiC_2. *J. Eur. Ceram. Soc.* **5**, 283 (1989).

40. El-Raghy, T., Barsoum, M. W., Zavaliangos, a. & Kalidindi, S. R. Processing and mechanical properties of Ti_3SiC_2: II, effect of grain size and deformation temperature. *J. Amer. Cer. Soc.* **82** 2855-2860 (1999).

41. El-Raghy, T., Zavaliangos, A., Barsoum, M. W. & Kalidindi, S. R. Damage Mechanisms Around Hardness Indentations in Ti_3SiC_2. *J. Amer. Cer. Soc.* **80**, 513-516 (1997).

42. Zhou, A. G., Barsoum, M. W., Basu, S., Kalidindi, S. R. & El-Raghy, T. Incipient and Regular Kink Bands in Dense and Porous Ti_2AlC. *Acta Mater.* **54**, 1631 (2006).

43. Zhou, A., Basu, S. & Barsoum, M. W. Kinking Nonlinear Elasticity, Damping, Micro- and Macroyielding of Hexagonal Close-Packed Metals. *Acta Mater.* **56**, 60-67 (2008).

44. Roundy, D., Krenn, C. R., Cohen, M. L. & J. W. Morris, J. Ideal shear strengths of fcc aluminum and copper. *Phys. Rev. Lett.* **82**, 2713-2716 (1999).

45. Cottrell, A. H. *Dislocations and plastic flow in crystals* (Oxford University Press, 1953).

46. Hull, D. *Introduction to dislocations* (Pergamon Press Ltd., Oxford, 1965).

47. Hess, J. B. & Barrett, C. S. Structure and Nature of Kink Bands in Zinc. *Trans. AIME* **185**, 599-606 (1949).

48. Basu, S., Barsoum, M. W., Williams, A. D. & Moustakas, T. D. Spherical nanoindentation and deformation mechanisms in free-standing GaN films. *J. App. Phys.* **101**, 083522 (2007).

49. Zhou, A. in *Materials Sc. and Engg.* (Drexel University, Philadelphia, 2008).

50. Kelly, B. T. *Physics of Graphite* (Applied Science Publishers, London, 1981).

51. Li, X. & Bhusan, B. A review of nanoindentation continuous stiffness measurement technique and its applications. *Materials Characterization* **48**, 11-36 (2002).

52. Field, J. S. & Swain, M. V. The indentation characterization of the mechanical properties of various carbon materials: glassy carbon, coke and pyrolytic graphite. *Carbon* **34**, 1357 (1996).

53. Bradby, J. E. et al. Contact-induced defect propagation in ZnO. *App. Phys. Lett* **80**, 4537-4539 (2002).

54. Moseson, A., Basu, S. & Barsoum, M. W. Determination of the effective zero point of contact for spherical nanoindentation. *J. Mater. Res.* **23**, 204-209 (2008).

55. Sneddon, I. N. The relaxation between load and penetration in the axisymmetric boussinesq problem for a punch of arbitrary profile. *Int. J. Engineering Science,* **3**, 47 (1965).

56. Lucas, B. N. & Oliver, W. C. Indentation power-law creep of high-purity indium. *Metallurgical And Materials Transactions A-Physical Metallurgy And Materials Science* **30**, 601-610 (1999).

57. Ozgur, U. et al. A comprehensive review of ZnO materials and devices. *J. App. Phys.* **98**, 041301 (2005).

58. Ahearn, J. S., Mills, J. J. & Westwood, A. R. C. Effect of electrolyte pH and bias voltage on the hardness of the (0001) ZnO surface. *J. Appl. Phys.* **49**, 96-102 (1978).

59. Prasad, S. V. & Zabinski, J. S. Tribological behavior of nanocrystalline zinc oxide films. *Wear* **203-204**, 498-506 (1997).

60. Coleman, V. A. et al. Mechanical properties of ZnO epitaxial layers grown on a- and c-axis sapphire. *App. Phys. Lett.* **86**, 203105 (2005).

61. Coleman, V. A., Bradby, J. E., Jagadish, C. & Phillips, M. R. in *Mater. Res. Soc. Symp. Proc.* 0957-K07-17 (Materials Research Society, 2007).

62. Coleman, V. A., Bradby, J. E., Jagadish, C. & Phillips, M. R. Observation of enhanced defect emission and excitonic quenching from spherically indented ZnO. *App. Phys. Lett.* **89**, 082102 (2006).

63. Kooi, B. J., Poppen, R. J., Carvalho, N. J. M., DeHosson, J. T. M. & Barsoum, M. W. Ti3SiC2: A damage tolerant ceramic studied with nanoindentations and transmission electron microscopy. *Acta Materialia* **51**, 2859-2872 (2003).

64. Molina-Aldareguia, J. M., Emmerlich, J., Palmquist, J., Jansson, U. & Hultman, L. Kink formation around indents in laminated Ti_3SiC_2 thin-films studied in the nano scale. *Scripta Mater.* **49**, 155-160 (2003).

65. Mulhearne, T. O. & Tabor, D. *J. Inst. Metals* **89**, 7 (1960).

66. Asif, S. A. S. & Pethica, J. B. Nanoindentation creep of single-crystal tungsten and gallium arsenide. *Phil. Mag. A* **76**, 1105-1118 (1997).

67. Mayo, M. J. & Nix, W. D. A micro-indentation study of superplasticity in Pb, Sn, and Sn-38 wt%Pb. *Acta Metall.* **36**, 2183-2192 (1988).

68. Barsoum, M. W. *Fundamentals of Ceramics* (Institute of Physics, Bristol, 2003).

69. Clarke, D. R. Varistor ceramics. *J. Am. Ceram. Soc.* **82**, 485-502 (1999).

70. Gittus, J. H. Theoretical equation for steady-state dislocation creep in a material having a threshold stress. *Proc. R. Soc. Lond. A* **342**, 279-287 (1975).

71. Sherby, O. D. & Wadsworth, J. Superplasticity - Recent advances and future directions. *Prog. Mater. Sci.* **33**, 169-221 (1989).

72. Cannon, W. R. & Langdon, T. G. Review Creep of Ceramics Part 2 - An examination of flow mechanisms. *J. Mater. Sci.* **23**, 1-20 (1988).

73. Weis, R. S. & Gaylord, T. K. Lithium Niobate: Summary of Physical Properties and Crystal Structure. *Appl. Phys. A* **37**, 191-203 (1985).

74. Vere, A. W. Mechanical twinning and crack nucleation in lithium niobate. *J. Mater. Sci.* **3**, 617-621 (1968).

75. Subhadra, K. G., Rao, K. K. & Sirdeshmukh, D. B. Systematic hardness studies on lithium niobate crystals. *Bull. Mater. Sci.* **23**, 147-150 (2000).

76. Park, B. M., Kitamura, K., Furukawa, Y. & Ji, Y. Relation between mechanical twinning and cracking in stoichiometric lithium niobate single crystals. *J. Am. Ceram. Soc.* **80**, 2689-92 (1997).

77. Park, B. M., Kitamura, K. & Furukawa, Y. Relations between ferroelectric polarization and mechanical twinning in stoichiometric lithium niobate single crystal. *J. Kor. Phys. Soc.* **32**, S789 - S792 (1998).

78. Schaefer, D. M., Patil, A., Andres, R. P. & Reifenberger, R. Elastic properties of individual nanometer-size supported gold clusters. *Phys. Rev. B* **51**, 5322 (1995).

79. Gerberich, W. W. et al. Reverse plasticity in single crystal silicon nanospheres. *Int. J. Plast.* **21**, 2391-2405 (2005).

80. Valentini, P., Gerberich, W. W. & Dumitrica, T. Phase-transition plasticity response in uniaxially compressed silicon nanospheres. *Phys. Rev. Lett.* **99**, 175701-1 (2007).

81. Johnson, K. L. *Contact Mechanics* (Cambridge, Cambridge University Press, 1985).

82. Ledbetter, H., Ogi, H. & Nakamura, N. Elastic, anelastic, piezoelectric coefficients of monocrystal lithium niobate. *Mechanics of Materials* **36**, 941-947 (2004).

83. Zhou, A., Basu, S. & Barsoum, M. W. Kinking Nonlinear Elasticity, Damping, Micro- and Macroyielding of Hexagonal Close-Packed Metals. *Acta Mater.* **56**, 60-67 (2007).

84. Pojprapai, S., Jones, J. L., Hoffman, M. & Vogel, S. C. Domain switching under cyclic mechanical loading in lead zirconate titanate. *J. Am. Ceram. Soc.* **89**, 3567-3569 (2006).

85. Kounga-Njiwa, A. B. et al. Ferroelasticity and R-curve behavior in $BiFeO_3$-$PbTiO_3$. *J. Am. Ceram. Soc.* **89**, 1761-1763 (2006).

86. Pearton, S. J., Zolper, J. C., Shul, R. J. & Ren, F. GaN: Processing, defects and devices. *J. App. Phys.* **86**, 1-78 (1999).

87. Pearton, S. J. et al. GaN electronics for high power, high temperature applications. *Materials Science and Engineering B* **82**, 227-231 (2001).

88. Oxley, C. H. Gallium Nitride: The promise of high RF power and low microwave noise performance in S and I band. *Solid-state Electronics* **48**, 1197-1203 (2004).

89. Liu, L. & Edgar, J. H. Substrates for gallium nitride epitaxy. *Materials Science and Engineering R* **37**, 61-127 (2002).

90. Kim, H. M., Oh, J. E. & Kang, T. W. Preparation of large area free-standing GaN substrates by HVPE using mechanical polishing liftoff method. *Materials Letters* **47**, 276-280 (2001).

91. Motoki, K. et al. Preparation of large GaN substrates. *Materials Science and Engineering B* **93**, 123-130 (2002).

92. Vaudo, R. P. et al. in *IWN 2000, IPAP conference series C1* 15 (Nagoya, Japan, 2000).

93. Oshima, Y. et al. Preparation of freestanding GaN wafers by hydride vapor phase epitaxy with void-assisted separation. *Japanese journal of applied physics part 2 - letters* **42**, L1-L3 (2003).

94. Yu, G. et al. Mechanical properties of the GaN thin Þlms deposited on sapphire substrate. *J. Crystal Growth* **189/190**, 701-705 (1998).

95. Kucheyev, S. O., Bradby, J. E., Williams, J. S., Jagadish, C. & Swain, M. V. Nanoindentation of epitaxial GaN films. *Appl. Phys. Lett.* **77**, 3373-3375 (2000).

96. Navamathavan, R. et al. 'Pop-in' phenomenon during nanoindentation in epitaxial GaN thin films on c-plane sapphire substrates. *Materials Chemistry and Physics* **99**, 410-413 (2006).

97. Caceres, D. et al. Nanoindentaion on AlGaN thin films. *J. App. Phys.* **86**, 6773-6778 (1999).

98. Nowak, R. et al. Elastic and plastic properties of GaN determined by nano-indentation of bulk crystal. *App. Phys. Lett.* **75**, 2070 (1999).

99. Bradby, J. E. et al. Indentation induced damage in GaN epilayers. *App. Phys. Lett.* **80**, 383-385 (2002).

100. Eddy, C. R., Moustakas, T. D. & Scanlon, J. Growth of gallium nitride thin films by electron-cyclotron resonance microwave plasma-assisted molecular-beam epitaxy. *J. App. Phys.* **73**, 448-455 (1993).

101. Williams, A. D. & Moustakas, T. D. Formation of Large-Area Freestanding Gallium Nitride Substrates by Natural Stress-Induced Separation of GaN and Sapphire. *J. Crystal Growth* **300**, 37-41 (2007).

102. Vlassak, J. J. & Nix, W. D. Measuring the elastic properties of anisotropic materials by means of indentation experiments. *J. Mech. Phys. Solids* **42**, 1223-1245 (1994).

103. Drory, M. D., AgerIII, J. W., Suski, T., Grzegory, I. & Porowski, S. Hardness and fracture toughness of bulk single crystal gallium nitride. *App. Phys. Lett.* **69**, 4044-4046 (1996).

104. Nowak, R., Li, C. L. & Swain, M. V. Comparison of implantation with Ni^{2+} and Au^{2+} ions on the indentation response of sapphire. *Materials Science and Engineering* **A253**, 167-177 (1998).

105. Hermann, M. et al. Nearly stress-free substrates for GaN homoepitaxy. *J. Crystal Growth* **293**, 462-468 (2006).

106. Saito, T., Hirayama, T., Yamamoto, T. & Ikuhara, Y. Lattice Strain and Dislocations in Polished Surfaces on Sapphire. *J. Amer. Cer. Soc.* **88**, 2277 (2005).

107. May, C. A. & Ashbee, K. H. G. Deformation kinking in the corundum structure. *Micron* **1**, 62-69 (1969).

108. Bridgman, P. W. *Large Plastic Flow and Fracture* (McGraw Hill, N.Y., 1952).

109. Tymiak, N. I., Daugela, A., Wyrobek, T. J. & Warren, O. L. Acoustic emission monitoring of the earliest stages of contact-induced plasticity in sapphire. *Acta Mater.* **52**, 553-563 (2004).

110. Nowak, R. et al. Peculiar surface deformation of sapphire: Numerical simulation of nanoindentation. *App. Phys. Lett* **83**, 5214-5216 (2003).

111. Nowak, R. & Sakai, M. The Anisotropy of Surface Deformationof Sapphire: Continous Indentation of Triangular Indenter. *Acta Mater.* **47**, 2879-2891 (1994).

112. Nowak, R., Sekino, T., Maruno, S. & Niihara, K. Deformation of Sapphire Induced by a Spherical Indentation on the (10-10) Plane. *Appl. Phys. Lett.* **68**, 1063-1065 (1996).

113. Wachtman, J. B. J., Tefft, W. E., Lam, D. C. J. & Stenchfield, R. P. Elastic Constants of Synthetic Single Crystal Corundum at Room Temperature. *J. Res. Natl. Bur. Std.* **64A**, 213 (1960).

114. Sun, Z.-M., Murugaiah, A., Zhen, T., Zhou, A. & Barsoum, M. W. Microstructure and Mechanical Properties of Porous Ti_3SiC_2. *Acta Mater.* **53**, 4359-4366 (2005).

115. Mitchell, T. E., Perlata, P. & Hirth, J. P. Deformation by a Kink Mechanism in High Temperature Materials. *Acta Mater.* **47**, 3687-3694 (1999).

116. Guyer, R. A., McCall, K. R. & Boitnott, G. N. Hysteresis, Discrete Memory and Nonlinear Wave Propagation in Rock: a New Paradigm. *Phys. Rev. Lett.* **74**, 3491 (1995).

117. Guyer, R. A. & Johnson, P. A. Nonlinear Mesoscopic Elasticity: Evidence for a New Class of Materials. *Physics Today* **52**, 30-36 (1999).

118. Bell, I. A. & Wilson, C. J. Deformation of Biotite and Muscovite: TEM microstructure and Deformation Model *Tectonophysics* **78**, 201-228 (1981).

119. Shea, W. T. & Kronenberg, A. K. Strength and anisotropy of foliated rocks with varied mica contents. *Journal of Structural Geology* **15**, 1097-1121 (1993).

120. Kronenberg, A., Kirby, S. & Pinkston, J. Basal slip and mechanical anisotropy in biotite. *J. Geophys. Res.* **95**, 19,257 (1990).

121. Christoffersen, R. & Kronenberg, A. K. Dislocation interactions in experimentally deformed biotite. *J Struc Geolg* **15**, 1077 (1993).

122. Meike, A. In situ deformation of micas: A high-voltage electron-microscope study. *Am. Mineral* **74**, 780 (1989).

123. McNeil, L. E. & Grimsditch, M. Elastic Moduli of Muscovite Mica. *J. Phys. Condens. Matter,* **5**, 1681-1690 (1993).

124. Holcomb, D. J. *J. Geophys. Res.,* **86** 6235 (1981).

125. Mares, V. A. & Kronenberg, A. K. Experimental deformation of muscovite. *J. Struc. Geol.* **15**, 1061-1075 (1993).

126. Stroh, A. N. The Cleavage of Metal Single Crystals. *Philos. Mag.,* **3** 597 (1958).

127. Zhen, T., Barsoum, M. W. & Kalidindi, S. R. Effects of Temperature, Strain Rate and Grain Size on the Mechanical Compressive Properties of Ti_3SiC_2 *Acta Mater.* **53**, 4163-4171 (2005).

128. Lawn, B. R. & Wilshaw, T. R. *Fracture of Brittle Solids* (Cambridge University Press, Cambridge, UK, 1975).

129. Zaafarani, N., Raabe, D., Roters, F. & Zaefferer, S. On the origin of deformation-induced rotation patterns below nanoindents. *Acta Mater.* **56**, 31-42 (2008).

130. Gilbert, C. J. et al. Fatigue-crack Growth and Fracture Properties of Coarse and Fine-grained Ti_3SiC_2. *Scripa Materialia* **238**, 761-767 (2000).

131. Barsoum, M. W., Radovic, M., Zhen, T. & Finkel, P. Dynamic Elastic Hysteretic Solids and Dislocations. *Phys. Rev. Lett.* **94**, 085501 (2005).

132. Fraczkiewicz, M., Zhou, A. G. & Barsoum, M. W. Mechanical Damping in Porous Ti_3SiC_2. *Acta Mater.* **54**, 5261-5270 (2006).

133. Radovic, M. et al. On the elastic properties and mechanical damping of Ti_3SiC_2, Ti_3GeC_2, $Ti_3Si_{0.5}Al_{0.5}C_2$ and Ti_2AlC in the 300 - 1573 K temperature range. *Acta Mater.* **54**, 2757 - 2767 (2006).

134. Basu, S., Zhou, A. & Barsoum, M. W. On Spherical Nanoindentations, Kinking Nonlinear Elasticity of Mica Single Crystals and Their Geological Implications. *J. Struc. Geol.* **Submitted for publication** (2008).

VITA

SANDIP BASU

EDUCATION:

Ph.D., Materials Science and Engineering, Drexel University, Philadelphia, PA, 2008
M.S., Ceramic Engineering, Institute of Technology, Banaras Hindu University, Varanasi, India, 2002
B.S., Ceramic Technology, College of Ceramic Technology, University of Calcutta, Calcutta, India, 2000

PUBLICATIONS:

1. Kinking nonlinear elasticity in metals, A. Zhou, S. Basu and M. W. Barsoum, Acta Mater. 56, 60 – 67 (2008).
2. Indirect observation of reversible dislocation motion in $LiNbO_3$ single crystal, S. Basu, A. Zhou and M. W. Barsoum, J. Mater. Res. 23, 1134-1138 (2008).
3. Determination of effective zero-point of contact for spherical nanoindentation, A. Moseson, S. Basu and M. W. Barsoum, J. Mater. Res. 23[1], 204-209 (2008).
4. Deformation micromechanisms of ZnO single crystals as determined from spherical nanoindentation stress-strain curves, S. Basu and M. W. Barsoum, J. Mater. Res. 22, 2470 - 2477 (2007).
5. Spherical nanoindentation and deformation mechanisms in free-standing GaN films, S. Basu, A. D. Williams, T. D. Moustakas and M. W. Barsoum, J. App. Phys. 101, 083522 (2007).
6. On the determination of spherical nanoindentation stress-strain curves, S. Basu, A. Moseson, and M. W. Barsoum, J. Mater. Res. 21, 2628-2637 (2006).
7. Sapphire – A kinking nonlinear elastic solid, S. Basu, M. W. Barsoum, and S. R. Kalidindi, J. App. Phys. 99, 063501 (2006).
8. Incipient and regular kink bands in fully dense and 10vol% porous Ti_2AlC, A. G. Zhou, M. W. Barsoum, S. Basu, S. R. Kalidindi, and T. El-Raghy, Acta Mater. 54, 1631-1639 (2006).
9. Microscale modeling of kinking nonlinear elastic solids, M. W. Barsoum, T. Zhen, A. Zhou, S. Basu, and S. R. Kalidindi, Physical Review B 71, 134101 (2005).
10. Room temperature constant-stress creep of a brittle solid studied by spherical nanoindentation, S. Basu, M. Radovic and M. W. Barsoum, J. App. Phys., Accepted (2008).

AFFILIATIONS:

American Ceramic Society (ACerS), Materials Research Society (MRS), American Society of Materials (ASM) and The Minerals, Metals and Materials Society (TMS).